Surface Electrical Resistivity Tomography: Infiltration Test Monitoring in Vegetated and Bare Soils

Auteur : De Lanève, Clément
Promoteur(s) : Nguyen, Frédéric; Caterina, David
Faculté : Faculté des Sciences appliquées
Diplôme : Master en ingénieur civil des mines et géologue, à finalité spécialisée en géologie de l'ingénieur et de l'environnement
Année académique : 2024-2025
URI/URL : http://hdl.handle.net/2268.2/23347

Université De Liège – Faculté des Sciences Appliquées

Surface Electrical Resistivity Tomography: Infiltration Test Monitoring in Vegetated and Bare Soils

Author: DE LANÈVE Clément

Master thesis presented to obtain the degree of:

Master of Science in Geological and Mining Engineering

professional focus in environmental and geological engineering

Supervisor: NGUYEN Frédéric

Co-Supervisor: CATERINA David

Academic year: 2024 – 2025

Acknowledgments

Many people deserve my gratitude for their participation and help in the achievement of this Master Thesis.

Firstly, I would like to thank my master thesis supervisor, Frédéric Nguyen, for his constructive guidance and dedicated supervision during this past year. I am also grateful to him for giving me the opportunity to present part of my work at the EGU General Assembly 2025, which was a valuable and enriching experience (cf. Nguyen et al., 2025).

I would also like to thank the Applied Geophysics Team at the University of Liège for warmly welcoming me, and in particular David Caterina for his support during and after the field works, as well as for his valuable remarks and advice. I would like to personally thank Abdeljalil Boutarfa, Gilles Swerts, and Aurore Degrée for organizing the Miscanthus Infiltration Test Experiment. I am grateful for the opportunity to participate in their work and contribute to the tests as part of my thesis. Although the internship was not directly related to this master thesis, I would like to take this opportunity to sincerely thank my internship supervisor, Mohamed Chtouki, for warmly hosting me at UM6P and for introducing me to the field of agrogeophysics during those six enriching weeks.

On a more personal note, I would like to thank my friends from the University for sharing both the tough and the good moments throughout this academic journey. Also, a special thanks to my classmates from the Geological Engineering master's program for these past months of working together, sharing our struggles, hardworking moments and laughs in our little office.

Lastly, I would like to thank my family, especially my parents, for giving me the opportunity to pursue this academic journey, for their unwavering support and encouragement, and for always believing in me throughout my studies.

Summary

Infiltration is one of the main focuses in hydrogeophysics studies, the assessment of infiltration can take various form such as studying infiltrations patterns, preferential flows, infiltration rate, … The applications of studying such processes can also be diverse, such as studying aquifer recharges, pollutant leaching or simply infiltration assessment for flood management. The last application cited is particularly important in agricultural sector. Indeed, agricultural crops are more and more subject important precipitations resulting in uncontrolled water runoff from fields and in water erosion creating mud flows. To reduce the consequences of these natural hazards, solutions have been developed such as buffer strips. The aim is to assess if such buffer strips can help mitigate the risks but also not induce a too large loss of profit for the farmers. In this context, perennial crops of Miscanthus X Giganteus cultivated for energy purposes have already been proved to reduce water erosion and are used also as a natural barrier for mud flows on border of fields, in addition of these properties, in this work, this plant is studied to assess its infiltration potential.

In order to demonstrate the better infiltration in soils with presence of miscanthus, a runoff infiltration experiment has been conducted in Gembloux (BE) monitored by Electrical Resistivity Tomography (ERT) surface profiles. The runoff setup was equally distributed in a miscanthus parcel and the bare soil of a field, uncultivated at the moment. The experiment was repeated 3 times and timelapse measurements were performed to study the dynamics of the infiltration. The processing of these data revealed few challenges mainly related to artifacts of resistivity increase and the influence of a water sheet flow during the infiltration step on the data acquisition. Firstly, to assess this influence, a synthetic model is construct and revealed that the top resistivity of the profile calculated by the inversion is misinterpreted (lower calculated resistivity than real resistivities). From this model, it is determined that despite misinterpreting the real resistivities, relative change is still qualitatively interpretable. For the other main problem (about artifacts), advanced processing consisting in applying full timelapse processing with spatial and temporal constraints revealed to be successful to reduce artifacts but also reduced the accuracy of the inversion result by over smoothing, nonetheless, change of resistivity is still proved to be accurate qualitatively.

At the end, timelapse study with before and after analysis revealed an overall greater resistivity decrease in the miscanthus plot, nevertheless due to limitation to convert this decrease in water content variation, the better infiltration potential cannot be rigorously proved but clues in the timelapse study are encouraging to suppose a better infiltration in the vegetated soil. An overall infiltration pattern has been distinguished, linking it with the initial conditions revealed limitations of the infiltration at a change of soil horizon at this time scale, v at an estimated depth of 40-50 cm. Finally, perspectives of infiltration monitoring by ERT were investigated through the assessment of an infiltration stick that has for purpose to be installed in small boreholes and increase resolution at higher depths when coupled with classic surface setups. The analysis between the stick and a classic setup revealed a good efficiency of the studied instrument.

Résumé

L'infiltration est l'un des principaux centres d'intérêt dans les études hydrogéophysiques, la mesure de l'infiltration peut prendre différentes formes, comme l'étude des patterns d'infiltrations, des écoulements préférentiels, du taux d'infiltration, etc. Les applications sont également variées, comme par exemple : l'étude de la recharge des aquifères, le lessivage de polluants ou simplement l'évaluation de l'infiltration pour la gestion des inondations. Cette dernière application est particulièrement importante dans le secteur agricole. En effet, les cultures agricoles sont de plus en plus soumises à d'importantes précipitations, entraînant des ruissellements incontrôlés depuis les champs et de l'érosion générant parfois des coulées de boues.

Pour réduire les conséquences de ces aléas naturels, des solutions ont été développées, telles que les bandes tampons. L'objectif est d'évaluer si de telles bandes tampons peuvent aider à atténuer les risques tout en n'induisant pas une trop grande perte financière pour les agriculteurs. Dans ce contexte, les cultures pérennes de Miscanthus X Giganteus, cultivées à des fins énergétiques, ont déjà démontré leur capacité à réduire l'érosion et sont également utilisées comme barrière naturelle contre les coulées de boue en bordure des champs. En plus de ces propriétés, ce travail étudie le potentiel d'infiltration de cette plante, afin de démontrer une meilleure infiltration dans les sols présentant du miscanthus, une expérience d'infiltration par ruissellement a été réalisée à Gembloux (BE), monitoré par des profils de tomographie électrique (ERT). Le dispositif de ruissellement a été réparti de manière égale entre une parcelle de miscanthus et le sol d'un champ non cultivé à ce moment-là. L'expérience a été répétée trois fois, et des mesures en time-lapse ont été effectuées pour étudier la dynamique de l'infiltration. Le traitement de ces données a révélé quelques défis, principalement liés aux artéfacts d'augmentation de résistivité et à l'influence d'un film d'eau en surface pendant l'infiltration sur l'acquisition des données. Tout d'abord, pour évaluer cette influence, un modèle synthétique a été construit et a révélé que la résistivité superficielle du profil calculée par l'inversion est mal interprétée (résistivité calculée plus faible que les résistivités réelles). À partir de ce modèle, il a été déterminé que, malgré une mauvaise estimation des résistivités réelles, les changements relatifs restent qualitativement interprétables. Pour l'autre problème principal (lié aux artéfacts), un traitement avancé consistant à appliquer un traitement "full inversion" en time-lapse avec contraintes spatiales et temporelles s'est avéré efficace pour réduire les artéfacts, mais a également réduit la précision du résultat de l'inversion par un lissage excessif, néanmoins, les changements de résistivités se sont révélés représentatif du phénomène qualitativement.

Au final, l'étude en time-lapse combiné à l'analyse avant/après a révélé une diminution globale plus importante de la résistivité dans la parcelle de miscanthus. Néanmoins, en raison des limitations pour convertir cette diminution en variation de teneur en eau, le meilleur potentiel d'infiltration ne peut être rigoureusement prouvé, mais les indices issus de l'étude time-lapse sont encourageants pour supposer une meilleure infiltration dans le sol végétalisé. Un pattern d'infiltration global a été déterminé, et la comparaison avec les conditions initiales a révélé une limitation de l'infiltration à un changement d'horizon pédologique, à cette échelle temporelle et à une profondeur estimée de 40-50 cm. Enfin, les perspectives pour le suivi de l'infiltration par ERT ont été explorées à travers l'évaluation d'un bâton d'infiltration conçu pour être installé dans de petits forages et qui peut permettre d'augmenter la résolution en profondeur lorsqu'il est couplé à des dispositifs classiques de surface. L'analyse entre le bâton et un dispositif classique a révélé une bonne efficacité de l'instrument étudié.

Table of Content

List of Figures

List of Tables

Introduction

Geophysical methods such as Electrical Resistivity Tomography (ERT) have become increasingly popular for investigating infiltration dynamics due to their ability to provide non-invasive, spatially and temporally resolved subsurface information. Timelapse ERT has proven effective in identifying preferential flow paths and monitoring infiltration fronts in a range of environments (Blazevic et al., 2020; Lu et al., 2022; Zhao et al., 2020). However, the reliability of timelapse ERT data interpretation can be affected by inversion artifacts, prompting the development of tailored inversion strategies (Clément et al., 2009; 2010) and studies on the influence of acquisition protocols (Austin et al., 2017; Haaken et al., 2016). Additionally, integrating petrophysical relationships has been shown to improve the interpretation of resistivity changes in terms of water content when high-resolution results are achieved (Dietrich et al., 2014; Hübner et al., 2017).

The main experiment conducted in this work aims to image the infiltration in a miscanthus parcel. ERT is not a conventional method, so it needs its own study for every case. This monitoring of an infiltration test differs from the ones existing because of the spatial differentiation of the infiltration that will be assessed and its direct objective to determine an infiltration potential of a vegetated soil in runoff conditions. Indeed, many experiments tend to often study infiltration on its own while this study has for additional objective to assess the hydraulic properties of a modified agricultural soil by a perennial plantation, in this case: Miscanthus X Giganteus. In short, here the infiltration heterogeneity will be directly compared under surface flow conditions and varying soil conditions (bare and vegetated soil). The particularity of this experiment also resides in the scale, indeed, the scale of this experiment is small spatially (6 m extension) and temporally short (5 h) but with numerous measurements made, allowing a high temporal resolution compared to existing experiments. Also, the experiment was repeated 3 times, whereas other studies often operate single-run experiments. This work also proposes an advanced inversion processing to try to avoid artifact generation and interpret the results as best as possible, given all the limitations imposed by the experiment conditions. In addition, it also displays various way to present the results to capture at best everything that could be extracted from it and do not stop at the interpretation of the resistivity profile images.

The manuscript is divided in 4 main sections. Firstly, in the Chapter 1, the state of the art will be reviewed with summaries of a selection of articles that focus on the ERT monitoring of infiltration test or water content evolution with time in natural conditions. From this state of the art, it is retrieved that numerous experiments exist with their own procedure and processing and each with a specific focus on infiltration, it can be in artificial medium like landfill, in natural conditions to study pollutant migration but also aquifer recharges or simply study infiltration pattern and preferential flows in a determined lithology. This literature review will mainly help to identify the different challenges that this type of study implies, especially to well interpret inversion results with the main problem that occur in most of the studies: artifacts appearance. Then, before

detailing the experiments conducted, a brief overview of the theory about ERT, inversion and petrophysics is realised in the Chapter 2.

Chapter 3 is the core of this work, presenting the description and the results of the conducted experiment of an infiltration test within a miscanthus parcel and bare soil. This chapter is itself divided in different parts including a description of the problematic with description of the vegetation of interest, the description of the experiment, the data quality assessment and the data processing with results and discussions that go with it. In this section, it will be described how an infiltration front have been estimated thanks to the inversion result images and the difference of resistivity evolution that occurs between bare soil and vegetated soil through different types of representations of the results, suggesting a potential better infiltration in the miscanthus parcel. It will also describe the difficulty of estimating water content from the resistivity and why the conversion turned out unsuccessful, limiting the assessment of a quantitative infiltration comparison between the soil types and relativizing the fact that the better infiltration into the vegetated plot can be rigorously demonstrated. Finally in the Chapter 4, a second experiment has been conducted to test an infiltration stick with integrated ring electrodes which is designed to be used in small boreholes. This section is already part of the perspectives for the future infiltration tests monitoring and tends to assess the efficiency of the instrument to later used it with classic surface ERT setups. In this section it will describe how the infiltration stick revealed to be an efficient instrument with comparing it to a classic setup. To finish this work, perspectives are mentioned and demonstrate the large possibilities of improvements of the miscanthus infiltration test experiment but also for the timelapse ERT in general because it exists in the literature numerous ways of proceeding the tests and the processing, offering space for new ideas to improve the results and specifically artifacts removal.

1.State of the Art

1.1. *Standard Infiltration Tests*

Generally, classic in-situ infiltration tests do not rely on geophysical measurements. The main infiltration tests used are borehole infiltration test, simple or double ring infiltrometer, drip infiltrometer, permeameter or other pilot tests like the ones mentioned in Philips & Kitch (2011) and Fan et al. (2020). These tests rely on water volume or water head punctual measurements in different setups and are mostly very local measurements. They often rely on theories that have strong hypothesis in terms of soil model, often considering the soil as homogeneous or simple model such as a layered soil model. These considerations imply an incapacity of reflecting the complexity of the soil and its non-uniformity, the efficacity is also impaired by the topography and flow stability, for example, the steady state is often difficult to maintain stable for a constant-head infiltration test (Fan et al., 2020). Different soil properties or lab measurement can also be used to evaluate the hydraulic conductivity of the soil of interest. (Philips & Kitch, 2011)

The input of geophysics and more specifically ERT is the establishment of other soil properties or parameters of the infiltration than what can already be extract with classic tests. These parameters or properties are for example the wetting front, the evolution of the moisture content or even the determination of preferential flows. Preferential flow is a parameter that cannot be easily deduce by classic infiltration tests because they determine an overall infiltration rate and not an infiltration pattern like ERT can deliver. In addition, several ranges of spatial scale are possible with this method while it was almost always punctual with classic tests, i.e., ERT can capture the spatial heterogeneity of the infiltration. Other advantages are the possibility of functioning by transient state and link the subsurface structure with the infiltration and additionally linking it with hydrogeological digital model (Fan et al., 2009). Disadvantages could be that specific infiltration setups have to be designed to investigate the region of interest like it has been realised in the experiments conducted that will be describe further in this document. Also, these setups are often more complicated to install than the classic ones.

1.2. *ERT Timelapse Monitoring: Literature Review*

The focus of the state of the art is timelapse experiments monitored by ERT that have been conducted by numerous researchers with various experimental setups, this analysis gives a good hint of the good practice that has been already realised but also information on eventual problems that could occur while processing these types of dataset as well with some interesting results that can be compared to the experiments conducted and detailed in this work. Focus has also been made on experiments that principally studied the infiltration processes in the vadose zone. Study like Hermans et al. (2012a) can study sea water intrusion in coastal environment but does not consider the vadose zone because the problem is due to aquifers interferences and is also study at a one frame images.

To begin with, to illustrate that timelapse ERT is not always about infiltration test but can present the same protocol of processing the data, a first study of interest is about heat injection. Indeed, Hermans et al. (2012b) studied the effect of heat injection in a shallow geothermal borehole with ERT data. This study is being realised by injecting heated water in a borehole, the conduction could in a way be interesting to also study water displacement. This acquisition was realised on a large profile scale (45.75 m) to be able to measure at the depth of interest. Sensitivity analysis was firstly performed to determine if the comparison between timelapse and background measurements were similar and then comparable. Inversion processing was performed with fixed starting and reference model corresponding to the background for the timelapse data. With this result and the confirmation by a forward model, the authors concluded that this technique was a reliable tool to distinguish the plume of heat induced by the injection of heated water. The result was analysed qualitatively with profile of percentage of change of resistivity compared to background but also quantitively by application of laboratory and petrophysical relations between the temperature and the resistivity calibrated by a thermo-hydrogeological model. (Hermans et al., 2012b)

The study mentioned in the previous paragraph gives a good idea of how timelapse data can be processed and interpreted. Nevertheless, this study does not focus on the water infiltration and is interested in the heat plume evolution, but it demonstrates the importance of sensitivity analysis and forward modelling to confirm that results are coherent. The next studies that are mentioned are all related to the imaging of the water infiltration, especially in the vadose zone.

Blazevic et al. (2020) performed their experiment with their own system of water infiltration, and they infiltrate about 250 L to 400 L per infiltration step that was performed once a day. They define a rectangular surface of 2.2 x 2.4 m separated by wooden planks and install 14 m long orthogonal profiles that go through the area of infiltration with a 20 cm spacing between electrodes. They also installed seismic profiles parallels to the ERT profiles. Different sensors were also installed at different depths to monitor the water content, temperature, and matric water potential. Concerning their results, the first try of processing an image with a starting and reference model homogeneous of 50 Ω.m, gave an image result with high increase in resistivity surrounding the supposed infiltration pattern. A different approach of the inversion processing using a two-steps inversion of the timelapse frame with choosing as start and reference model the lower resistivity model between background result and first inversion of the considered frame is used to force the result to a decrease in resistivities and avoiding the increase in resistivity anomalies. This method does decrease the artifacts but do not completely erase them. Despite these artifacts and with the seismic investigation as well, the authors conclude that with their results, they have been able to identify preferential flow paths and the overall direction of the flow with the determination of isochrones of percentage of resistivity decrease or velocity change for the seismic profiles. (Blazevic et al., 2020)

Like mentioned in the previous paragraph, preferential flows are often the factor of interest when realising infiltration tests monitored by ERT. Several studies have monitored infiltration test to study preferential flows. Lu et al. (2022) used a double ring infiltrometer coupled with ERT

profiles and cross-hole resistivity measurements to infiltrate deionized water in the vadose zone. On the contrary of classic or salted water, the infiltration of deionized water results in an increase in the bulk resistivity in the inversion result and, in this case, decreasing resistivity artifacts were observed. Nevertheless, this study still identified preferential flows and matrix flow areas. On another scale, Du et al. (2024) constructed a multi-layer model at a scale of 1:3000 with simulated cracks in a sandstone layer to assess infiltration patterns in cracks for coal mine geological hazard. They added to their model an array of electrodes to acquire the ERT data while injecting water on top of the model. They demonstrate that at the start of the infiltration the preferential flows were important in the cracks and clearly visible, while continuing the infiltration, those preferential paths became less pronounced to become almost invisible avec 3 hours of injection, because of the increase in the matrix flow. Their conclusion was that cracks should be identified at an early stage of the infiltration test when water flow only in the preferential pathways. (Du et al., 2024)

Another environment that has preferential flows characteristics is loess. Zhao et al. (2020)'s experiment induced an infiltration by a simple ring infiltrometer, the objective was to characterise the preferential flows present in a loess plateau that includes an agricultural field. This experiment denotes by its use of different profiles with different electrode spacings, large spacings were used to characterise at lower resolution plot-scale information and then small spacings were used to characterise with a high-resolution localised information. The spacing of 0.2 m was sufficient to analyse the infiltration processes and to capture anomalies that induced these different infiltration patterns. Preferential flows have been effectively detected with the use of ERT monitoring, these observations have been confirmed by excavation. Timelapse measurements also revealed that infiltration was first dominated with preferential flows but then transferred into matrix flow with time passing to progressively reach deeper depths. (Zhao et al., 2020)

This study helped the authors understanding the mechanics of water infiltration in loess plateau and revealed that intact loess was limiting water infiltration when no preferential flow patterns where present, the direct effect of intact loess was a diminution of the infiltration capacity of these areas under high water fluxes circumstances. On a ERT data processing point of view, they encountered problems with high temperature changes of the surface during the data acquisition. Increase in temperature during the beginning of the test revealed a change in the measured resistivities having a real impact on the background and further measurements interpretations. This effect could induce an inaccuracy if quantitative observations are needed (Zhao et al., 2020). Nevertheless, if temperature is measured with accuracy and for every ERT measurements, data correction based on the temperature can be operated.

Fernández de Vera et al. (2017) used an infiltration pond with a saline tracer to assess the infiltration in the vadose zone on a former industrial site. The ERT setup includes surface electrodes and cross-hole ERT. A vadose zone monitoring system (VMS) is also used in this experiment. The 1.5 x 1 m infiltration pond with 50 cm depth was crossed by two almost perpendicular ERT lines of 48 and 32 electrodes, respectively 20 and 40 m long and a constant spacing between electrodes for each line. Four 15 m-deep boreholes were also equipped with 24 electrodes each. The

background resistivity results showed the distinction between the main lithologies and the boreholes artificial materials. The top part has been distinguished as backfill, and silt and sand deposit beneath it were also distinguished. Time lapse results are analysed by resistivity change compared to background with a define threshold of percentage decrease in resistivity, rendering white cells when the decrease is less important and for increase in resistivity (probably artifacts, or drying soil). This method highlighted the tracer location. (Fernández de Vera et al., 2017)

The 5-days timelapse results revealed the formation of a plume induced by the saline tracer, with a distinguishing orientation, the maximum of resistivity decrease was located near the surface suggesting that most of the tracer was retained in the backfill. Rain events increase the vertical flow and induce deeper infiltration of the tracer that is visible on the inversion result. VMS data also suggested that the tracer was maintain in the backfill during this period. More measurements were then realised up to 105 days after the tracer injection and revealed an increasing depth of infiltration of the tracer with time also highlighting preferential flows. The evolution of the tracer infiltration was mainly dependant of the rain events. The deeper depth of the tracer was measured at 4 m. This study concluded that the matrix flow mechanisms was dominant and such factor have a major influence on the transport of pollutants being highly dependent of the precipitations, while dry seasons are occurring, pollutants can take month to reach the level beneath the backfill. The VMS results correlated with the ERT measurements and revealed a non-uniformity of the tracer infiltration and allowed to characterize the distribution of the plume by the resistivity measurements. Some issues related to the ERT data, and their processing were encountered especially on the profile with a high spacing between the electrodes having important level of noise and generating artifacts in the inversion solutions. (Fernández de Vera et al., 2017)

Haaken et al. (2016) operated a similar experiment in a similar context, with monitoring infiltration in the context of SAT (Soil Aquifer Treatment) with ERT but also GPR (Ground-Penetrating Radar). A pond was equipped with hydrological sensors and the geophysical instruments such as the ERT profiles. For the timelapse measurements, the electrodes were buried at 75 cm below ground surface. A total of 288 electrodes composed three different profiles. The pond alternate with drying and flooding sequences for a total of 15 days of experiment. Acquisitions were operated every hour during all the experiment for a total of 363 surveys. Inverse modelling was performed using a difference inversion approach that means the objective function is no longer only dependant of $\mathbf{m}$ (the model solution) but $\mathbf{m}-\mathbf{m_0}$ where $\mathbf{m_0}$ is the background model. On the inversion results, the water infiltration is clearly visible covering the total extension of the profile after a few hours in the shallow part of the profile (2 m), the infiltration in the bottom layer that is coarser occurs after 18h after the start of injection. In addition to the inversion result images, the evolution of conductivity of single cells has been studied showing the increase in conductivity during infiltration steps but also a focus on the drying curves, i.e., the decrease in conductivity during the drying steps. These curves are studied and link to the hydraulic properties of the considered layer, showing a difference in the transient response depending on the considered lithologies. The decrease in conductivity was fitting an exponential function with specific parameters dependant of the lithologies. (Haaken et al., 2016)

The analysis of this approach allows the authors to process an aquifer zonation on behalf of the electrical conductivity evolution with time during drying steps. They concluded that ERT was a powerful tool to monitor SAT systems and helped determinate the optimum infiltration cycle to apply. (Haaken et al., 2016)

Austin et al. (2017) also conducted an infiltration test of their own but by using a rainfall simulator that can reproduce at best a rain event thanks to under pressure pipes located at a determined height so that drops hit the soil at a realistic velocity for rain. Their simulator is coupled with electrodes arrays to obtain time-lapse data for the different infiltration events that they simulate. Like other studies, artifacts showing an incoherent increase in resistivities were present, while they have been able to diminish these artifacts with inversion parametrisation, they investigate further this phenomenon by running a simple forward model of their experiment. This model is simple and corresponds to the real soil composition on site, it is a two layered model (0 to 0.5 m deep layer and 0.5 to 2 m layer) with the top layer that has a decreasing resistivity with time. The objective of this forward model was to modify the resistivity of the bottom layer to observe if any variations occurred on the interpretation but most importantly also modify the acquisition protocol to observe if the protocols induced an effect on the artifacts' intensity. They did prove that the intensity of this artifacts is highly dependent on the acquisition protocols, for example, the dipole-dipole array produces artifacts of high resistivity values while Wenner-alpha array reduces drastically these artifacts but do not represent the infiltration zone accurately because it fails to delineate the infiltration front. (Austin et al., 2017)

Other studies have tried to reduce or delete those artifacts to have a clean image of the infiltration front. Clément et al. (2009) try to erase the high resistivity artifacts by advanced inversion processing. To assess their implementation, they constructed a synthetic model consisting of a multi-layer model with a top layer that have a decreasing resistivity that represents the infiltration. The objective was to represent a few decimetres deep infiltration. To study the intensity of the artifacts, they chose to use the ratio between the calculated image and the background, meaning that a ratio greater than 1 is an increase in resistivity and smaller, a decrease. The standard inversion resulted in high ratio beneath the infiltration going up to 6 depending on the layers. Then, their advanced inversion scheme was used consisting of using a decoupling line at the level of the infiltration front, for objective to delineate the two subregions. This addition to the inversion process created a result with artifacts but with a way lesser amplitude than before, the maximum ratio reached was 1.3, proving that this methodology reduces the artifacts. Along with the test of their inversion process, they also simulate different electrodes spacing and logically determined that the smaller the spacing, the better the resolution of the infiltration front, too large electrodes spacings (2 m for example) are not capable of representing the infiltration front of only a few decimetres (40 cm in this case). (Clément et al., 2009)

The decoupling line inversion process was then applied on a real case study that has in addition to the ERT timelapse data, an a priori knowledge of the infiltration front at 6 locations on the profile thanks to a Neutron Probe. Standard Inversion already revealed that the infiltration front was well

represented with taking a ratio threshold at 0.8 and corroborated with the neutron probe interpretation, decrease in resistivity was still present beneath this level, overestimating the infiltration of water, which is why the 0.8 value was chosen. And as it was expected the increase in resistivity at greater depth do not correlate with the neutron probe data, confirming these effects are artifacts. (Clément et al., 2009)

Once standard inversion is realised, they tested their advanced inversion processing with a decoupling line at a constant depth showing only decrease in resistivity in the upper decoupling zone and less important increase in the deeper zone with even some artifacts having a smaller area. From this point, they concluded that their advanced inversion process did help reducing the artifacts but did not find it entirely satisfactory, therefore, they tried to refine their decoupling line with a priori information such as the neutron probe data (partial information of the front) or the standard inversion and they suggested also using a TDR (Time Domain reflectometry) sensor (exact knowledge or almost exact knowledge of the front). Partial information of the infiltration front results in a better image but still with few artifacts and with the decoupling line almost the same as the infiltration front, almost no artifacts were observed in the upper decoupling zone and are limited in the deeper zone. (Clément et al., 2009)

As a conclusion, the technique of decoupling line can be particularly useful with knowledge of the infiltration front to reduce high resistivity artifacts, nevertheless, this is often the point of interest of this type of measurement. Clément et al. (2009) also suggested an eventual approach with using Invariant zone to reduce artifacts like it has already been made in other cases. To conclude they suggest using a spacing as small as possible between electrodes to reduce from the beginning the possibility of artifacts appearances. (Clément et al., 2009)

Artifacts appearances often occur when measuring infiltration and with standard processing. On some context, these artifacts can be misinterpreted as real phenomena, it is often occurring in waste landfills when studying the circulation of leachate and may misinterpret the increase in resistivities as biogas migration in the landfill. Therefore, Clément et al. (2010) investigates array configuration and inversion processing to try to reduce or even eliminate at best the artifacts to better interpret the real phenomena occurring.

To assess the effects of array configurations and inversion parameters, they create 2D and 3D models to then generate synthetic data from these models. These models are blocks models with isotropic and homogeneous property. This summary will focus on the 2D model that they created because no 3D inversion was investigated in the context of this master thesis. The resistivity attribution and the geometry of the model is based on a real case study of a waste landfill, the general geometry is composed of two layers: one shallow layer of 1.5 m meter height with a 100 Ω.m resistivity and a 15 m high layer of 15 Ω.m representing the landfill. When these layers are infiltrated by leachate, they respectively decrease of 70 or 60% of resistivity. This infiltration is represented by a 2 m wide trench in the top layer and an 8 m wide and 2.5 m high bulb beneath it. They differentiate two types of processing, the standard processing, and the advanced processing so that comparison between both results can be done. The standard processing is a classic timelapse

inversion scheme of Gauss-Newton minimization with isotropic smoothness and a fixed regularization factor of 30 (λ), the timelapse frame is calculated using the background as reference model to reduce change between the images. (Clément et al., 2010)

As it was hypothesized by the authors artifacts can be generated in function of the acquisition protocol. The two symmetrical arrays: Wenner-Schlumberger and Dipole-Dipole created many artifacts while Pole-Dipole array had limited artifacts and an overall satisfactory result with standard inversion. To characterise the different artifacts generated with the symmetrical arrays, the following distinction is made:

- AI_s: Increase in resistivities in the shallow part along the trench
- AI_d: Increase in resistivities at deeper levels
- AD: Decrease in resistivities
- RV: Real Variation of resistivities, corresponding to the simulated infiltration of leachate

For standard inversions, the RV region is well represented, nevertheless a lot of AI_s are observed near the trench for the Wenner-Schlumberger array, AI_d for both arrays that could cause misinterpretation of drying zone or biogas circulation. AD are observed beneath the infiltration bulb for the Wenner-Schlumberger array as well, this artifact could lead to an overestimation of the infiltration front. For the Dipole-Dipole array, AD are observed at shallower depth and the RV is a bit overestimated. This analysis reflects the significant effect of the acquisition protocol on the results but also that artifacts are always generated and can lead to misinterpretation if not spotted and recognize as artifacts. (Clément et al., 2010)

Advanced processing is applied on the synthetic data to try to delete the artifacts. This processing consists of two different regularizations: the application of invariant resistivity regions and another constraint tending to minimize the variation from background (minimum length constraint). The invariant regions concerned the bottom of the model where it is known that no flux can flow, in reality this corresponds to the bottom of the landfill, sides are also fixed as invariant regions, on real data, this information can be retrieved by other methods like a neutron-probe or electromagnetic measurements. (Clément et al., 2010)

For the results of their advanced processing, fixing values in some regions revealed a good quantitative representation of the infiltration pattern while the minimum length constraint underestimated the resistivity decrease. AI_d were absent around the bulb of infiltration, except for Dipole-Dipole array with fix regions. But the minimum length constraint had also some possible misinterpretation with an overestimation of depth of infiltration (AD). Combination of both array configurations data did not improve the solution and even created more artifacts. Advanced processing resulted in a better representation of the infiltration, with advancements in artifacts removal, dependence of the acquisition protocol has also been proved with better result with Pole-Dipole configuration, further model with representation of biogas migration (zone of increase in resistivities) has also been generated to assess if the advanced processing can distinguish real increase in resistivity from artifact generation. This article relates on the high number of parameters

that can generate artifacts and how to deal with them using different regularizations with advanced processing. It also discuss the difficulty to model a situation without eliminating real phenomena by over constraining the inversion model. (Clément et al., 2010)

The vadose zone is also often studied to study the recharge processes of aquifers, especially in the karst vadose zone. In the study of Watlet et al. (2018), they operated a long term ERT monitoring of a karst vadose zone. Their first challenge was to define a background because the infiltration will be induced by the precipitations, they then decided to operate a background measurement during the dryest season of the year, in order to then enhance the water content increase for the future measurements. What differs from the other infiltration monitoring study is the representation of the change of resistivity, it is represented as a log resistivity change where ρ_i is the resistivity of the time considered and ρ_o the resistivity of the background:

$$\Delta\rho = \left(\frac{\log(\rho_i)}{\log(\rho_o)} - 1\right) * 100 \quad (1)$$

In their processing, in addition to the reference model constraint, they also added a temporal constraint. The inversion results allow to determine 8 distinct regions of the profile with different infiltration dynamics. Generally, the top layer present the highest variability of resistivity change with time while more deeper regions present a more diffuse infiltration with lower seasonal variation, but what was interesting is the large fracture present in the profile that was on static images more conductive and on timelapse frames presented a high variability dependant of the rainfall event. (Watlet et al., 2018)

Another case study of water infiltration in unsaturated soil has been conducted in the Cevennes (France) by Brunet et al. (2010). The plot of 400 m² was old terraces with vineyards that are now uncultivated and located on a slope of about 15%. This monitoring did not imply an artificial induced water injections because they made 10 different measurements during a period of 22 months (February 2006 to December 2007) and was done to study the evolution of water content in the experimental plot. A 48 electrodes array with 50 cm spacing was installed perpendicular to the slope. With these measurements, they also used a TDR sensor at 3 distinct locations to retrieve the water content vertical profiles. Soil samples were also taken to quantify the different empiric factors of Archie's law used for calibration of the resistivity/water content relationship. These factors were retrieved by electrical resistivity measurement of the soil samples in laboratory with a knowledge of the exact water content. Pore water resistivity evolution with contact with soils were also studied in laboratory for different initial water composition. Finally, from these soil samples, the porosity of the soil was retrieved. All these measurements allowed the authors to perform a water deficit estimation of the 2D profiles for the 1.2 m top part of soil considering a highly non-porous bedrock. For accuracy of the pore water resistivity estimation, measurements were only made more than 100h after the last rainfall so that mineral composition equilibrium was established between the soil and the water and laboratory results can be used for this estimation.

They concluded that the mean water deficit ranged from 270 mm to 365 mm respectively in the wettest and driest conditions. (Brunet et al., 2010)

To confirm their results, they compared them with the different TDR measurements and despite being spaced by about 5 m they revealed similar temporal patterns but differences in volumetric water content can reach up to 5% with TDR estimation being smaller than the ERT's in dry soils but higher in wet soils. Authors explained that these variations, especially for dry soils, can be caused because Archie's calibration could not develop low water content. Another source of error could be the calibration of the TDR sensor. At the end, new measurements with another type of probe revealed underestimation and overestimation in dry/wet soils for the TDR probe. After further processing on the TDR and ERT measurements only in the top 70 cm soils using an overall same porosity, revealed a good link between the two methods with a maximum difference of water deficit estimation of 15%. On the overall results, ERT shows a trend to smooth more the seasonal variations of water deficit in the soils but has been revealed to have a good potential to assess the variation of the water deficit/water content in the plot. (Brunet et al., 2010)

To conclude, authors listed uncertainties that could impact their water content/deficit estimation:

- Temperature, despite applying a temperature correction on the data, small bias in the temperature has a direct effect on the estimation, a 10% bias in temperature lead to a 4% bias on the corrected resistivity.
- Pore water resistivity, a 10% positive bias led to a 5.9% bias in water content.
- Porosity, a 10% positive bias led to a 2.35% bias in water content.

Authors insisted on well assessing the different properties of the Archie's law, nevertheless, bias in the parameters also generated a smaller error in the water content estimation, like it can be deducted from the examples listed above. The last uncertainty is the inversion algorithm that have a decreasing accuracy with depth, sensitivity of the generated solution must be well studied to discard any errors resulting for the inversion results and the deeper resistivity result must be well analysed before making any interpretations. (Brunet et al., 2010)

This study revealed the good practices to quantify the water content of a given plot. Especially with all the parameters retrieved to apply Archie's law on an ERT profile. They succeeded to interpret resistivities as water content or water deficit in the unsaturated soil and linking it with the dry and wet seasons and the TDR measurements.

Another example of timelapse ERT where they applied Archie's law to monitor the water content evolution is Dietrich et al. (2014), this study has been realised in a soil with a petrocalcic horizon. Like the previous study, they used laboratory results to calibrate the different parameters and confirmed it by a 1D simulation with Hydrus and TDR results. The infiltration process was induced by irrigation on two specific zone along the 11.2 m profile with 20 cm spacing electrodes for a total of 27 days of experiment, studying the infiltration process and the drainage, drying process once the infiltration step was finished for a total of 19 timelapse measurements.

The inversion results revealed a difference in the composing material of the soil thanks to the distinction between zones with different resistivities. Soil water content change imaging allowed to distinguish preferential flows that were present especially in the less cemented zone and to spot low-permeability bodies where lateral fluxes were more important, these zones were spotted as $CaCO_3$ rich soils. Also, it was proven that drainage processes had a slower dynamic compared to the infiltration process showing a high-water retention in fine-grained soil. The results were confirmed by numerical solution of the problem and the TDR sensor data. Authors concluded that 2D ERT was a reliable tool to monitor the water content changes in the vadose zone and distinguish the heterogeneity presence. (Dietrich et al., 2014)

Sometimes, ERT is just used as an additional tool, in the article from Loukil et al. (2021), they investigate an olive mill waste water storage and performed geochemical and ERT measurements. In this case, the ERT results helped to confirm the geochemical analysis and to understand the subsurface structure and preferential zones of infiltration. They did not use advanced processing for inversion and simply interpreted static images. (Loukil et al., 2021)

To finish this non-exhaustive list of all timelapse monitoring tests that exist in the literature, the article from Hübner et al. (2017) is reviewed because of its close similarities with the experiment performed in the context of this master thesis. They operated an infiltration test with two controlled high intensity irrigation tests in a horizontal multi-layer subsurface context with contrasting hydrological properties between. To monitor this infiltration, they used a 3D ERT configuration and operated numerous measurements for 5 days. The setup was composed of two different parts in the upper and the lower part of the slope. The upper part include a 2.8 x 5.6 m area with 196 electrodes spaced by 0.2 m. In the lower part a 0.2 m grid was also used but with only 98 electrodes. This high number of electrodes allows a high resolution but the small spacing between them requires a high precision in the determination of their position to avoid any mistake by mislocating the electrodes in the inversion model. (Hübner et al., 2017)

Their results were that the top highly conductive organic layer presenting a lot of macropores, and a high hydraulic conductivity was reflected in the ERT results by preferential flows patterns. The second layer at 50 cm depth had a significant lower hydraulic conductivity but flow was still entering this layer but mostly with matrix flow, slowing the vertical components of the flow. Once the coarser material reached, the basalt layer, capillary effect was observed, holding the water in the upper layer and enhancing the lateral flow in the direction of the slope. Only when high water content is reached, the capillary barrier breaks, and water infiltrate the basalt. To conclude this interpretation, they used the inversion results processed by background as reference model, a precise estimation of the error and anisotropic penalties to enhance the vertical variation. In addition, they used a fine mesh and were helped by tension-meter based hydrometric measurements. (Hübner et al., 2017)

1.3. *Conclusion of the State of the Art*

From all the articles reviewed in the previous sub-section, no unified operating procedure has been determined. This means that each researcher defines their own methodology to perform and analyse infiltration monitoring using ERT data, often without referring to a standardized framework.

While some will rely on existing infiltration setups like a double ring infiltrometer (Lu et al., 2022), infiltration ponds (Fernández de Vera et al., 2017; Haaken et al., 2016) or own design setup such as the rain simulator from Austin et al. (2017) or a showerhead with wooden planks separation (Blazevic et al., 2020), others will simply use natural conditions to study the evolution of the soil water content (Watlet et al., 2018; Brunet al., 2010; Dietrich et al, 2014).

The space extension of these various timelapse experiments can drastically vary from only a few meters in extent to larger extent reaching few decametres large profiles. This will mainly be determined by the phenomenon of interest, while aquifer recharge studies will be composed of very large profiles with large spacing and then lower resolution, others will study water interaction very close to the surface and then will increase drastically the resolution by using a very small spacing between electrodes (for example 0.2 m spacing for Zhao et al. (2020) and Hübner et al. (2017)). Also, some studies will focus on only 2D profiles while others study the evolution of infiltration with 3D arrays. Additionally, some studies, particularly when studying deeper interactions, will use borehole electrodes to better represent the medium at greater depths (ex: Fernández de Vera et al. (2017)) or sometimes burying the electrodes to assure their positioning during all the experiment (Haaken et al., 2016).

For the inversion processing, the main challenge was the presence of numerous artifacts of increase resistivities that by their definition were not representative of any physical reality. There are no established protocols to process the timelapse data without appearance of artifacts, therefore, each researcher has designed their own processing based on previous studies, inversion theory and personal experiences. The more common approach is using a reference model regularization on the timelapse frames by using as reference the background processed with classic constraints for static images (Blazevic et al., 2020; Watlet et al., 2018, Hübner et al., 2017). Often, this kind of processing generated increased resistivity artifacts that some tried to get rid of by different regularization. While some simply added a temporal constraint (Watlet et al., 2018), others used processing that require a priori knowledge of the medium by other instrument (neutron probe, TDR…) or simply lithology knowledge. Clément et al. (2009) used this a priori knowledge to determine a decoupling line that best fit the infiltration front and observed encouraging results in the reduction of the artifacts. Clément et al., (2010) used knowledge of bedrock and side of a landfill to impose invariant regions in the inversion model and also observed a decrease in the artifact's generation. Few authors used forward modelling, i.e., generating data with a synthetic model to firstly assess the influence of array configuration on the artifact's generation (Austin et

al., 2017; Clément et al., 2010) but also to confirm their advanced processing and to determine how the physical interpretation of the timelapse frames could be impacted.

Finally, the representation of the infiltration pattern is done using change of resistivity images where the decrease in resistivity usually relates the infiltration of water. Often, a threshold of resistivity decrease is determined to mask the artifacts of increase in resistivity and the low decrease zone not relating water infiltration. Some authors will use ratio of resistivities, others percentage of change and some their own way to represent the change like Watlet et al. (2018) using a log resistivity change. Also, with good determination of Archie's law parameters and calibration, some authors like Brunet et al. (2010) and Dietrich et al. (2014) successfully represented the water content of their respective profile with transforming the real resistivity calculated in water deficit or volumetric water content.

2. Materials and Methods

2.1. *Electrical Resistivity Tomography Theory*

Electrical Resistivity Tomography is based on a simple electric principle. Electric current is injected into the ground with a given intensity I (A) with one or a pair of electrodes. Another pair of electrodes then measures a potential V (V). The objective is to retrieve the resistivity of the studied space. For a simple cylinder, the resistivity (ρ) (Ω.m) is defined as follows by Pouillet's Law:

$$\rho = \frac{RA}{L} \tag{2}$$

Where R is the resistance (Ω), L the length (m) of the cylinder and A the cross-sectional surface (m^2). It is also worth noting that other geophysical techniques, such as Electromagnetic Induction (EMI), investigate the same property but typically in terms of conductivity rather than resistivity (Everett, 2013).

The law that governs this method is Ohm's law. It can be written as follows:

$$\boldsymbol{J} = \sigma \boldsymbol{E} \Leftrightarrow \boldsymbol{E} = \frac{\boldsymbol{J}}{\sigma} = \rho \boldsymbol{J} \tag{3}$$

Where J is the current density field (A/m^2), E the electric field (V/m) and σ the conductivity (S/m). This expression corresponds directly to its equivalent in a circuit: V = I.R where I is the intensity of the current (A).

Let us consider a homogeneous half space isotropic with the injecting electrodes situated at the top of this space representing the Earth's surface. At a distance r (m) from the injection point, the current density J can be expressed as the current density on the surface of the half sphere of radius r (m):

$$J = \frac{I}{2\pi r^2} \tag{4}$$

then the potential V can be recovered by integrating this result on the surface and by using the relation

$$I = -\frac{dV(r)}{dr} \tag{5}$$

$$J = -\sigma \frac{dV(r)}{dr} \Leftrightarrow \frac{dV(r)}{dr} = -\frac{I}{2\pi\sigma r^2} \tag{6}$$

By integrating this solution, and considering that $V(\infty) = 0$, it is found that:

$$V(r) = \frac{I}{2\pi\sigma r} = \frac{I\rho}{2\pi r} \tag{7}$$

With this formula it is then possible to express the voltage measured by the two measuring electrodes (M and N). Furthermore, from this voltage, the resistivity can be retrieved. This calculated resistivity is called the apparent resistivity ρ_a (Ω.m) and is only valid under the hypothesis that the half space is homogeneous and isotropic, conditions that are almost never encountered in reality. Nevertheless, it is often used to provide a first overview of the measured data. (Everett, 2013)

$$V_{MN} = V_M - V_N = \frac{I\rho}{2\pi}\left(\frac{1}{r_M} - \frac{1}{r_N}\right) \tag{8}$$

$$\Leftrightarrow \rho_a = \frac{2\pi V_{MN}}{I}\left(\frac{1}{r_M} - \frac{1}{r_n}\right)^{-1} = \kappa\frac{V_{MN}}{I} \tag{9}$$

Where κ is the geometric factor (m) and r_m and r_N the respective distance (m) between the injecting electrode and the measuring electrodes. This formula is valid for 3 electrodes setups, the more common setups are composed of 4 electrodes array changing the geometric factor by the following formula (Everett, 2013):

$$\kappa = \frac{2\pi}{\frac{1}{AM} - \frac{1}{AN} - \frac{1}{BM} - \frac{1}{BN}} \tag{10}$$

Different kind of array configurations exist, they differ by their overall sensitivity, targets of interest, depth of investigation, lateral or vertical sensitivity and signal-to-noise ratio (Loke et al., 2013). Some of these array configurations and their sensitivities can be found in Figure 2-1, The C1 and C2 points (often referred as A and B) are the electrodes where the current is injected, and P1 and P2 are the measuring electrodes, also often referred as M and N. The most commonly used configuration is the Dipole-Dipole array because it has an overall high lateral sensitivity while other arrays, such as the Gradient array, have more vertical sensitivity. (Dahlin & Zhou, 2004)

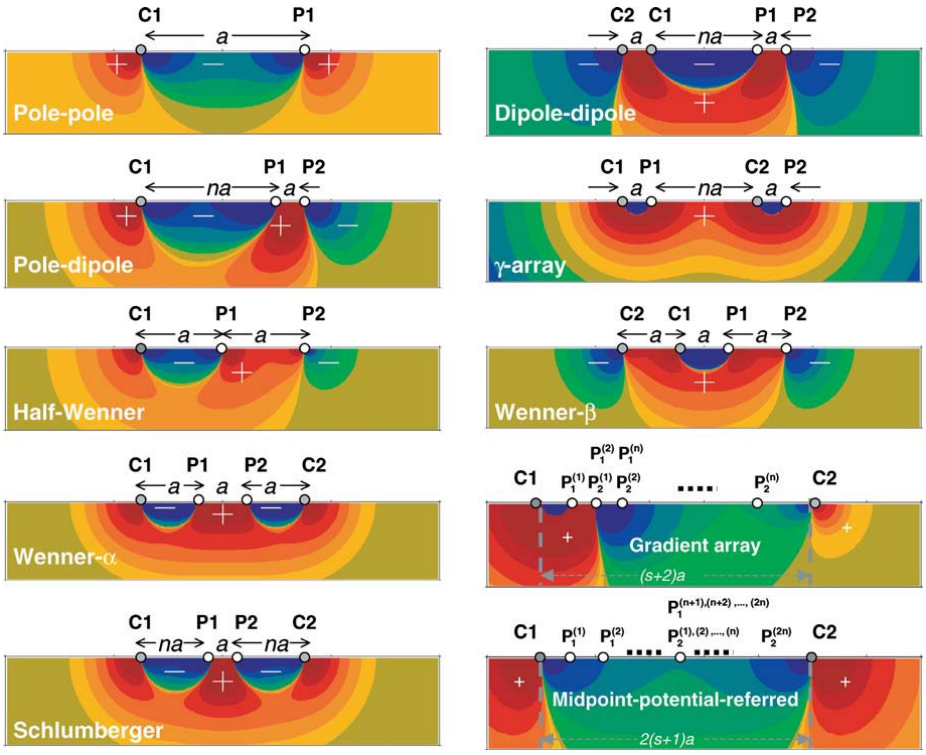

Figure 2-1: Schematics of electrode array configurations and their sensitivity patterns for one given configuration of each type of array (Dahlin & Zhou, 2004)

2.2. *Inversion Theory*

The main goal of inversion processing is to be able to resolve the forward problem:

$$\boldsymbol{d} = \boldsymbol{g}(\boldsymbol{m}) \tag{11}$$

With g the forward non-linear operator and g^{-1} does not exist, so that $g^{-1}(\boldsymbol{d}) = \boldsymbol{m}$ cannot be directly resolved. The vector $\boldsymbol{m}$ contains the parameters that define the model, in this case the resistivities. This is the model vector, while $\boldsymbol{d}$ is a vector containing all the know data, i.e., the measured resistances. The inverse problem can then be restated as finding **m** by using the forward mapping, which reproduces at best the given data **d** to a specified level of uncertainty. The two vectors, **m** and **d,** can also be represented by applying a logarithmic transform to the model result and the data to resolve the problem. Since the inverse problem implies finding a solution of a problem with M unknowns and N inputs of data, where M greater than N, the inverse problem solution is non-unique, and the numerical problem is ill-posed. To counter these issues, additional constraints must be imposed on the inversion (Binley & Kemna, 2005). To do that, the problem will be resolved by optimizing (minimizing) an objective function that has the following form:

$$\Psi(\boldsymbol{m}) = \Psi_d(\boldsymbol{m}) + \lambda * \Psi_m(\boldsymbol{m}) \tag{12}$$

Where λ is the regularisation parameter. The first function that needs to be minimize is relative the data misfit, in a L_2 normalization (this is the only normalization used in the case of this master thesis) its expression is the following formula:

$$\Psi_d(\boldsymbol{m}) = \|\boldsymbol{W_d}[\boldsymbol{d} - \boldsymbol{g}(\boldsymbol{m})]\|_2^2 \quad (13)$$

In an L_1 normalization, the formula not squared, but in practice, IRLS (Iterative Reweighted Least Squares) algorithm is used to approximate the L_1 norm because of the singularity produced by the absolute value. The $\boldsymbol{W_d}$ matrix is a data weighting matrix associated with the individual data errors (a diagonal matrix comprising the inverse of each individual error). Usually, the error for single inversion is determined using reciprocal data and can be expressed as the logarithm of the difference between measured resistances for normal and reciprocal data, but this can be adapted depending on the context (see Section 2.3). (Lesparre et al., 2017)

The second term of the objective function is a stabilizing model objective function whose purpose is to regularize the problem by choosing the regularization operator *L* best suited for this purpose.

$$\Psi_m(\boldsymbol{m}) = \|\boldsymbol{W_m}L(\boldsymbol{m})\|_2^2 \quad (14)$$

Where $\mathbf{W_m}$ is a matrix defining the imposed constraint, usually composed of 1 and -1, and permits to define smoothing between adjacent cells or not.

In many cases, and in the case of the processing realised for this master thesis, the regularisation is based on a given reference model $\boldsymbol{m_{ref}}$ such as the previous formula is express as follows:

$$\Psi_m(\boldsymbol{m}) = \left\|\boldsymbol{W_m}\left(\boldsymbol{m} - \boldsymbol{m_{ref}}\right)\right\|_2^2 \quad (15)$$

The solution is then found by minimizing the objective function, by using an iterative process, usually by a Gauss-Newton approach that with the previous expressions, can be expressed as follow for a given step *k*:

$$\left(\boldsymbol{J_k^T W_d^T W_d J_k} + \lambda\, \boldsymbol{W_m^T W_m}\right)\Delta\boldsymbol{m_k} = \boldsymbol{J_k^T W_d^T W_d}[\boldsymbol{d} - \boldsymbol{g}(\boldsymbol{m_k})] - \lambda\, \boldsymbol{W_m^T W_m}\left(\boldsymbol{m_k} - \boldsymbol{m_{ref}}\right) \quad (16)$$

The model update is then simply calculated by updating the current model: $\boldsymbol{m_{k+1}} = \boldsymbol{m_k} + \Delta\boldsymbol{m_k}$. The matrix $\boldsymbol{J}$ is the Jacobian matrix comprising the partial derivatives based on the data vector.

To calculate the wanted solution, it is then possible to calculate multiple steps of the iterative process until reaching a satisfactory solution. The stop criterion can be chosen as when misfit of data is as small as possible by a given value ($\Psi_d(\boldsymbol{m_k})$ < Criterion) or sometimes the model converges towards a solution that does not reach the target criterion, the iterative process can then be stopped if the change between two consecutive models becomes small or after a given number of iterations. To help the model converges faster it is often useful to start with a starting model ($\boldsymbol{m_0}$) known to be close or similar to the solution. For example, in the case of the timelapse processing, the starting model of the timelapse data is often chosen as the background solution

previously calculated. For single inversion, homogeneous starting model with median of apparent resistivities can be chosen for example. (Binley & Kemna, 2005)

Once a solution is reached, diverse ways of knowing the sensitivity of the final model exist. It can be found by calculating a resolution matrix, but is also often simply assessed by determining the cumulated sensitivity of the model thanks to the Jacobian matrix, by simply computing the following formula:

$$s_j = (\boldsymbol{J^T J})_{jj} \; or \; \left(\boldsymbol{J^T W_d^T W_d J}\right)_{jj} \text{ if weighting matrixes are present} \tag{17}$$

This is a quick and inexpensive way to estimate the resolution, where sensitivity is low, resolution is supposed to be low as well. Another way to assess the resolution of a given model is to calculate a depth of investigation index (DOI index). This approach is based on the calculated of two models using the same inversion process but with different reference models. Then, by applying the following formula, an index is found, revealing the regions that are more or less constrained, which can then be interpreted as high or low sensitivity areas.

$$DOI_j = \frac{m_j^{(1)} - m_j^{(2)}}{m_{ref_j}^{(1)} - m_{ref_j}^{(2)}} \tag{18}$$

Where $m_j^{(1)}, m_j^{(2)}$ are the models' solutions and $m_{ref_j}^{(1)}, m_{ref_j}^{(2)}$ are reference models of each calculated model. While this method is powerful to assess the sensitivity of a model, only the sensitivity matrix is used during processing of the field data in this master thesis, due to the large dataset and the fact that DOI calculation requires performing two additional inversions, while the sensitivity matrix is directly calculated from the Jacobian matrix which used for calculating the final model. (Binley & Kemna, 2005)

To define the quality of final result, the root mean square error (non-weighted) is calculated by comparing real data with calculated resistivities by the following formula:

$$RMS = \sqrt{\sum_{i=0}^{n} \frac{(d_i - m_i)^2}{n}} \tag{19}$$

Often, the relative root mean square error is used, and this will be the case in most of this work, it is simply defined as the root mean square error but weighted by the data value such as:

$$RRMS = \sqrt{\frac{\sum_{i=0}^{n} \frac{(d_i - m_i)^2}{n}}{\sum_{i=0}^{n} (d_i^2)}} \tag{20}$$

2.3. *Full Timelapse and Time-constrained Processing*

Kim et al. (2009) developed a new way to invert ERT data for timelapse measurements, the main objective is to improve the solution of monitoring temporal change without contaminating the image solution by inversion artifacts often present in classic processing.

To do that they based their work on developing the inversion algorithm specifically for DC resistivity data. Their approach, like the classic inversion scheme, uses a least-squares inversion algorithm. The subsurface model is assumed to change continuously in time, the medium is defined in a space and time domain. It means that the model not only depends on the 3 dimensions of space but also with time, making the model a 4-D space when adding the temporal "coordinate", this is why this algorithm is called 4-D inversion algorithm, in the case of this study 3D space data are not considered because only profiles are analysed separately but the principle behind stay the same, only one spatial dimension is omitted. When considering a 4-D model, it is therefore possible to perform a single, simultaneous inversion of all the monitored data.

If the same overall functioning explained in the previous section is reused, the model vector (**m**) become the space-time model vector **m** of all the considered timesteps, such as:

$$\boldsymbol{m} = \{\boldsymbol{m_1}, \boldsymbol{m_2}, \dots, \boldsymbol{m_n}\} \tag{21}$$

Where n is the number of timesteps collected, and m_i the corresponding model vector of the timestep i.

Kim et al. (2009) algorithm proceed steps in the inversion problem while using m reference model in the total of the n timesteps allowing them to determine a subsurface model U containing these reference models. The inversion is then performed on this reduced set of parameters by minimizing the error, using linear interpolation to estimate the model at non-reference timesteps based on the reference models. Additionally, the forward model response between these timesteps of reference are also interpolated but by a first-order Taylor expansion. These steps allow to reduce the size of the given matrixes for calculations. Additional space and time constraints are added to the objective function. For more information, please refer to Kim et al. (2009).

The full inversion proceed in the used python package (pyGimli) in this master thesis is simplified compared to Kim et al. (2009) and is explained in Günther & Martin (2016), where they used the same source code as what has been done on the experimental data of this work but with frequential data and not temporal data, this changes nothing to the inversion algorithm.

The space-time model vector stays the same as in the equation (21) and in the same way the data vector become a combination of all the data vectors of each timestep such as:

$$\boldsymbol{d} = \{\boldsymbol{d_1}, \boldsymbol{d_2}, \dots, \boldsymbol{d_n}\} \tag{22}$$

While the model and data vector become "vectors of vectors", the Jacobian matrix becomes a block-diagonal matrix with all the individual Jacobian matrix filling the diagonal.

$$\boldsymbol{J} = \begin{bmatrix} \boldsymbol{J_1} & \boldsymbol{0} & \cdots & \boldsymbol{0} \\ \boldsymbol{0} & \boldsymbol{J_2} & \cdots & \boldsymbol{0} \\ \vdots & \vdots & \ddots & \vdots \\ \boldsymbol{0} & \boldsymbol{0} & \cdots & \boldsymbol{J_n} \end{bmatrix} \tag{23}$$

The iterative and updating model process then follows the same equation as (16), a smoothness constraint is applied between adjacent cells, but here a temporal constraint is added to increase smoothness between the same cells of different timesteps. (Günther & Martin, 2016)

In addition to these changes, the weighting matrix from equation (13) can also be adapted to the timelapse problem to better account for error variation between frames. As the data weighting is operated with a new error definition taking the timelapse problem into account:

$$\epsilon_{TL} = |\Delta log\, R_N - \Delta\, log\, R_R| \tag{24}$$

Where ϵ_{TL} is the timelapse error, which can be estimated by an envelope fit or a least-squares fit of the error as a function of the mean resistance. $\Delta \log R_n \; and \; \Delta \log R_R$ are the log-resistance differences between normal and reciprocal measurements, comparing the background and the considered time step. This data weighting approach is used in data-difference inversion. (Lesparre et al., 2017)

While these smoothness constraints are not explicitly detailed by pyGimli documentation, a temporal smoothness can be added to the objective function in the same way it was explained with the equation (14) for the spatial regularization. So that the objective function becomes:

$$\Psi(\boldsymbol{m}) = \Psi_d(\boldsymbol{m}) + \lambda * \Psi_m(\boldsymbol{m}) + \beta * \Psi_t(\boldsymbol{m}) \tag{25}$$

The added function can take the following form and is dependent of a weighting matrix ($\mathbf{W_t}$), with a determined form.

$$\Psi_t(\boldsymbol{m}) = \|\boldsymbol{W_t m}\|_2^2 \tag{26}$$

With for example:

$$\boldsymbol{W_t} = \begin{bmatrix} 1 & -1 & 0 & \cdots & 0 \\ 0 & 1 & -1 & \ddots & \vdots \\ \vdots & 0 & 1 & \ddots & 0 \\ \vdots & \vdots & \ddots & \ddots & -1 \\ 0 & 0 & \cdots & 0 & 1 \end{bmatrix} \tag{27}$$

This matrix imposes smoothing between two consecutive steps but can be designed to constrain between multiple timesteps by filling the matrix with 1 or -1, or even numbers smaller than 1 to weight the different constraints between timesteps as a function of their time differences. And of course, the temporal constraint is governed by the imposed smoothing factor β.

2.4. *Petrophysics Theory: Archie's Law*

Once electrical resistivity models are retrieved from the results of the inversion, resistivities can be converted into saturation or water content using a petrophysical law, this is especially useful in the infiltration monitoring or simply moisture mapping of a given site. An empirical law was established to link the resistivity of a given bulk with resistivity of the water, the saturation, and the porosity. This law is called Archie's law after it was introduced by Archie (1942). Then over time, this law has been adapted as its applications have evolved and is often used in converting ERT profiles or 3D model from resistivity to water content. In the literature review, that was the case for Brunet et al. (2010) and Dietrich et al. (2014).

Brunet et al. (2010) expressed the relation to isolate the direct relation between the bulk resistivity (ρ in Ω.m), the water resistivity (ρ_w in Ω.m), the porosity of the material (Φ (-)) and the saturation (S (-)):

$$\rho = a\,\rho_w\,\Phi^{-m}\,S^{-n} \tag{28}$$

In this expression, 3 different empirical parameters are present where *m* is the coefficient of cementation, ranging from 1.2 to 4, *n* is the coefficient of saturation which is generally close to 2 when water is used and *a*, which is often considered equal to 1, especially for the unconsolidated materials (Frohlich & Park, 1989; Ward, 1990; Telford et al, 2009). The validity of Archie's law is for medium to coarse-grained soils and rocks, which is then not applicable in every situation (Brunet et al., 2010). Especially because of the assumption of Archie's law that the change of conductivity is mainly induced by the pore water conductivity and do not consider the effect of the surface conductivity present in clay materials. For the same saturation, a material with a clay fraction will have a lower resistivity. A model has been proposed to include this effect but need additional parameters of the soil (cation exchange capacity and empirical parameters), making the relation more complicated and increasing the number of unknowns (Waxman & Smits, 1968).

In the equation (28), the three different parameters *a*, *m* and *n* are empirical parameters, it means that for every experiment that converts resistivity into water content estimation, soil samples have to be taken, and resistivity measurements must be operated in laboratory while controlling the actual water content in order to determine these empirical parameters. Also, with these samples, the porosity must be determined, and the water conductivity/resistivity must be measured in order to leave only the saturation as an unknown that can be calculated by the previous formula.

The conversion from saturation to water content is simply made by multiplying the saturation found by the porosity.

2.5. *Materials*

The main instrument used in the experiments is the ABEM Terrameter LS2 (Guideline GEO) with stainless steel electrodes to acquire ERT data. In addition, a conductivity meter was used to retrieve the electrical conductivity of the infiltrated water. A water pump and a flow regulator were also used to control the infiltration rate.

All data processing was performed using Python 3 and especially the open-source library pyGimli for geophysical data processing (Rücker et al., 2017).

3. Miscanthus Infiltration Test Monitoring

3.1. *Miscanthus in Agriculture and for Water Erosion Management*

The growing need to produce greener energy, and especially the urge to transition from fossil fuel consumption to bio-based fuel or energy has raised numerous challenges in the agricultural sector specialised in crops for energy purposes. Plantations also need to follow ecological standards like low fertilization, plant protection and low energy input, and additionally a low erosion potential and a beneficial effect on the biodiversity. Other criteria privileged are the adaptation of the crop to a local demand, reducing the transportation economic and ecological costs, a minimal irrigation to save as much water as possible and also, from a social point of view, improving the public perception of the countryside. Crops that fulfil most of these conditions are perennial crops because of their high yielding, limited maintenance, and inputs. (Winkler et al., 2020)

Miscanthus X Giganteus is one of these perennial crops. Defined as a "rhizomatous perennial C4 grass", this plantation originated from East Asia and presents an extra underground structure with numerous rhizomes and roots, its height goes up to 3, even 4 m. This important height results in an important yield of the crops. While green harvesting is preferred for biogas production, most of miscanthus crops are brown harvested at the end of the autumn for combustion purposes, another application of miscanthus is also animal bedding. 20-year rotation crops are usually operated with an annual harvesting of the top part, but the base plant is left, tillage is then drastically reduced. (Kam et al., 2020; Winkler et al., 2020)

The tillage reduction along with the underground structure of miscanthus result in an improved soil structure. Also, these crops have a high carbon storage capacity, which increases the organic carbon present in the soil and directly increases the fertility and the soil stability by aggregation. Because of the low tillage necessary, these crops are more adapted to be cultivated in irregular shaped fields or less accessible fields. These types of crops have been a focus in the recent EU regulations because they provide important production for the green energy plan and have a good impact on other ecological properties previously cited such as (Winkler et al., 2020):

- Increasing carbon content in soil
- Improving the soil structure, improving erosion protection
- Conserving and developing the biodiversity

The properties of these crops allow them to be used also as buffer strips along waterbodies or field borders as is the case in this work. Buffer strips can help reduce soil erosion by improving soil structure and reducing water runoff by increasing infiltration through root systems and water deficit during critical times. (Anderson et al., 2009; Winkler et al., 2020).

While the properties of reducing erosion and increase infiltration in different buffer strips plantation has been proved. The reduction of water erosion induced by miscanthus has been studied in different studies such as the one describe further in this chapter (Mazur & Kowalczyk-Jùsko, 2021) along with proof of high yielding in winter flood zone area (Kam et al., 2020). Less is known about the water infiltration properties of Miscanthus, it is the main reason the following experiment described in this document was conducted.

But before detailing the conducted experiment, the water erosion reduction potential is reviewed with the analyse of the work of Mazur & Kowalczyk-Jùsko (2021), their experiment also assess partially the water infiltration potential.

Water erosion is a geomorphological force that reshapes environments by affecting soil stability and fertility. This effect can have direct influences on the landscape or agricultural land by directly affecting the arable land through soil displacement and reduced fertility (Firooz & Firooz, 2024). Water erosion can be classified in different categories base on their processes (Firooz & Firooz, 2024):

- Sheet erosion, the removal of surface soil layers by drop impact or surface runoff.
- Rill erosion, manifesting by the creation of small channels in soils resulting from water runoff.
- Gully erosion, is the extreme form of rill erosion, creating large channels making agricultural exploitation impossible.
- Streambank erosion, occurring on riverbanks.

The first two types of erosion are the ones that are mainly involved in agricultural context.

As part of the different studies, miscanthus has been studied to see if its implementation on the border of fields could help prevent water erosion or at least reduce it to an acceptable level as hypothesised, due to its underground structural properties. Mazur & Kowalczyk-Jùsko (2021) conducted a two-year experiment to demonstrate the effectiveness of Miscanthus in reducing water erosion and soil degradation, their experimental protocol was to select two distinct parcels, one with a new miscanthus plantation while the other one was empty with no planted vegetation to be used as a control zone. Both plots were located nearby in the same field with similar topography. The objective was to select plots with the most identical properties possible. To monitor their results, they assessed different parameters such as soil properties, biomass, rainfall data, water quality and finally the soil displacement as a measure of total soil volume displaced. For this last parameter they differentiate three types of erosion partially in accordance with the earlier classification for the two first types:

- Linear erosion (or rill erosion), the formation of small channels by the washing of shallow soil
- Surface erosion, washing of the top layers of soil by water flowing on top of the soil.
- Patches of deposited sediment, formed by deposition of eroded soil material.

Their results align with their hypothesis. Indeed, firstly, in terms of soil mass losses, they were 29% higher in the control plot than in the miscanthus plot with a significant difference of rill erosion that is up to 89.3% higher. Nevertheless, surface erosion and patches of eroded sediments are lower in the control plot by a factor of 17.4 and 21.4%, respectively. Secondly, the water quality analysis revealed a lower concentration of ammonia-based compounds in the miscanthus plot, marker of a lesser fertiliser runoff than in the control plot, these results about water quality also confirm an effect of miscanthus for reducing the surface water pollution. Finally, the average water runoff was calculated in the plots and compared to the real precipitations and revealed a lower water runoff from the miscanthus plot. The average water runoff is 17.4% of the total precipitations in the miscanthus plot while it increases up to 20.4% in the control plot. (Mazur & Kowalczyk-Jùsko, 2021).

With flow analysis, they distinguished a lower runoff from the miscanthus part, the objective of this chapter is to provide additional information about the infiltration potential of miscanthus through analysis of the timelapse ERT monitoring of a runoff infiltration test.

3.2. *Site Description*

The site investigated in the context of this experiment is the border of a beet field, with no crops at the moment of the experiment. On the South-East border, miscanthus has been planted and is now mature. The band of miscanthus is about 20 m wide and covers all of this border. This band of miscanthus has been planted following events of mudflow coming from the field and damaging the roads and buildings downhill. The objective with this miscanthus parcel is to reduce the mud flow primarily, but if the infiltration potential is better, this could also help prevent or at least reduce possible flooding events. The layout of the field and its location regarding the urban area is visible on the map of the Figure 3-1.

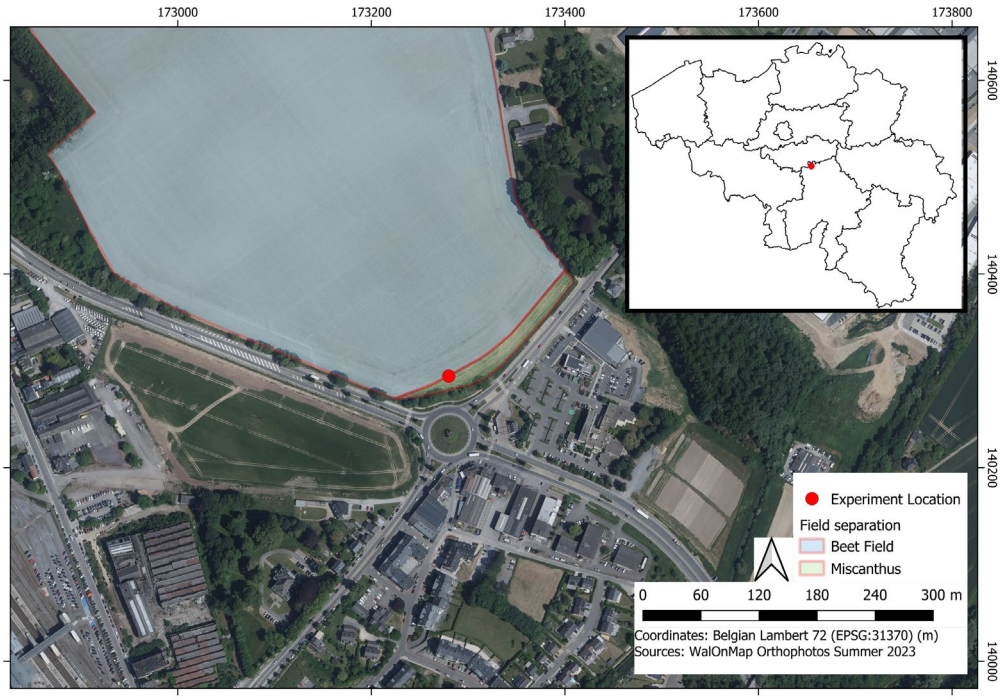

Figure 3-1: Map of the site location and its surroundings (Modified from SPW, 2024)

The soil characterisation is retrieved from the digital soil map of Wallonia. From this map, it is known that the soil is silty, in the Annexe 1, it can be seen in the diagram the classification of this soil type, which is referred to as letter A in the figure. The digital map also informs about the drainage condition, and it is considered as a soil with favourable drainage conditions and finally, the last piece of information provided is that the soil has a structural B horizon. (Bah et al., 2005; SPW, 2022)

3.3. *Experiment*

3.3.1. Experimental Setup

The following description of the experimental setup has been repeated three times at the same location side by side, one repetition per day. From now on, each experiment will be mentioned as 1, 2 or 3 depending on their order of realisation.

The setup for the infiltration is different from usual infiltration tests such as double ring infiltrometer because in this case, estimating a value of hydraulic conductivity is not the objective. Other tests have been conducted alongside this experiment to determine hydraulic conductivities but will be used to compare with the results of this experiment. The infiltration setup used is a runoff infiltration, thanks to the slight inclination of the field on its border, the water is injected on top of the small hill, a part will flow on top of the soil and a fraction of water will be infiltrated in the soil, water that has not been infiltrated is recuperate at the bottom and pumped back into the water tank to have a closed-loop system so that at the end of the experiment, an estimation of the

total infiltrated water is possible. The surface of this runoff infiltration is 6 m² in a form of a band measuring 1 m by 6 m where water is running off along the greater dimension, this band is separated thanks to plastic boards embedded in the soil.

The final objective being the differentiation of infiltration between bare soil and the parcel with miscanthus, the first three meters of the infiltration band is composed of bare soil (uncultivated soil between the miscanthus and the cultivated field) and the last three meters is within the miscanthus parcel with the tops of the plants that have been cut to let the roots and the base of it untouched, mainly for practical reasons. There is also mulch on the miscanthus half that has not been removed to keep the overall same conditions that without the setup. The height difference between top of the band and the bottom is 0.33, 0.31 and 0.31 m for the three different bands in order of realisation of each experiment, it means that bands have an overall mean slope of 5%.

The other important setup that must be detailed is the electrode setup for the ERT acquisition. It has been chosen to carry out three different profiles within the infiltration setup. The main one that will be called the longitudinal profile has the same direction as the water flow. This profile goes through both soil types and is the longest profile with a length equal to the band length: 6 m. It is composed of 16 electrodes with equal distances between each: 0.4 m. Two other profiles are also installed, but perpendicular to the main line, and each one cuts one of the two halves through the middle. These 2 lines have the same configuration, i.e., 16 electrodes with a 0.3 m spacing for a total length of 4.5 m, it has been chosen to reduce the spacing to increase the resolution and because these two profiles do not have to be as long as the first one since the region of interest is only 1 m wide.

The experimental setup is summarised in the next Figure (Figure 3-2)

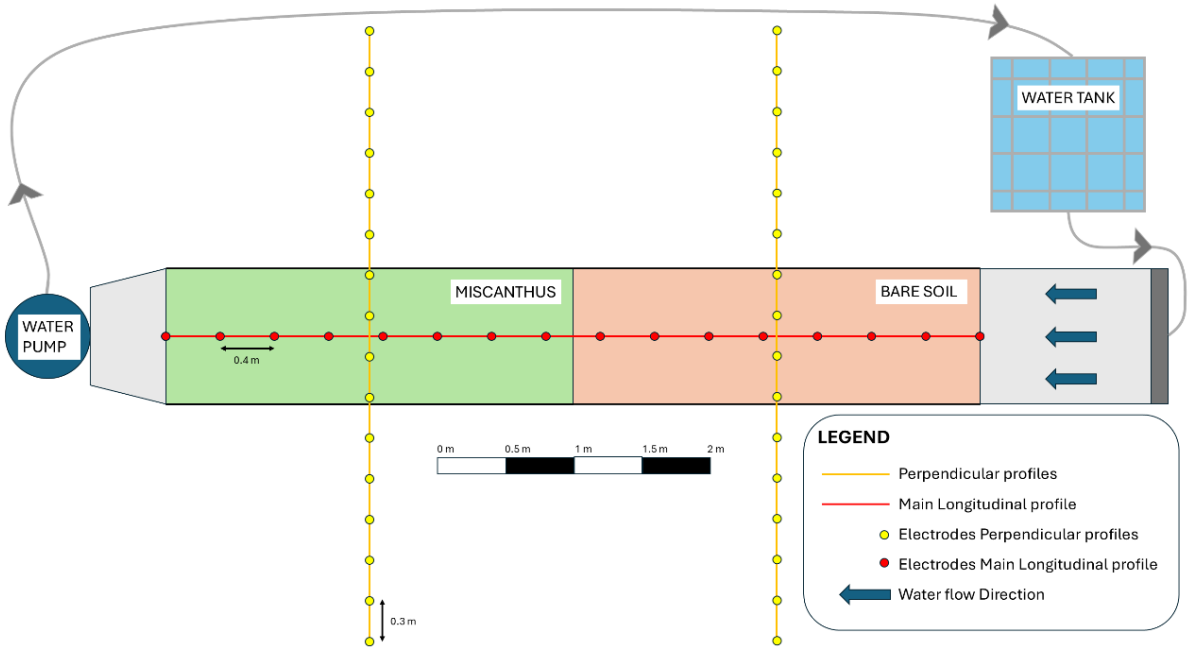

Figure 3-2: Schematic of the infiltration and ERT setups

3.3.2. Infiltration and ERT Parameters

The last subject to discuss when preparing the field trip is the acquisition protocol: how the data will be acquired and what the timesteps are. To maximize the number of timelapse frames during the infiltration, it was decided that only the longitudinal profile would acquire data during the infiltration process. Every acquisition is done on a single line by a Dipole-Dipole 6 protocol coupled with a Gradient 7 protocol with 48 and 49 measurements respectively for a total of 97 different measurements for one acquisition. Due to the small number of electrodes of the profiles (16) compared to usual electrode arrays, the two protocols are merged to increase the number of datapoints and then increase the robustness of the inversion problem.

The ABEM Terrameter LS2 was configured to automatically acquire the measurements. The script for the automation was designed to last 1h as when the machine is started, it acquired 9 normal acquisitions then 1 reciprocal measurement, again 9 normal acquisitions and a final reciprocal measurement, this script was then launched every hour during the duration of each experiment. Nevertheless, because precautions were taken to ensure automated measurements do not exceed one hour, it was possible to take 2 more manual measurements after the end of the script before it restarts for the next hour. Thus, 20 measurements were made on the longitudinal profile and 2 reciprocal measurements every hour.

The water flow determined is 1 L/s, this value can slightly change during the experiment but does not vary by more than 2%. Two interconnected water tanks of 1 m^3 each were used. Salt was added to the water to increase the conductivity and then the contrast.

3.3.3. Course of the Experiment

The experiment was conducted during the end of August 2024 (19, 21 and 23 August 2024). The weather was generally dry and hot during the experiment if the rain at the end of 23 August is excluded, this rain event did not impact the data acquisition because it only happened at the very end when the data acquisition was over. The dry weather preceding the experiment ensured an unsaturated soil to acquire background data and operate the infiltration test.

Before the start of each experiment, 2 different background measurements were made on all the profiles, then automated acquisition on the longitudinal profile was started. After 1 or 2 measurements the infiltration test began. On the first day, the infiltration lasted 2 hours, once finished the measurements continued for 2 hours. The two other days the same protocol was realised except for the infiltration that ran for 3 hours. At the end of the experiment, 2 after-experiment measurements were taken on all profiles.

Concerning the events that were observed during the experiments, for each repetition after approximately 3 minutes a water sheet flow established. This body of water was a few centimetres deep and had a significant impact on the data because of its low resistivity and needs to be considered when processing and interpreting the data. Measurements of this water sheet flow have been made during the experiments to try to quantify it. These measurements are represented

alongside the topography on the different graphs from the Figure 3-3. They also display the topography of the 3 experiments, and it can be observed that they all have similar geometry especially this small basin that is present in the middle of the profile due to a slight increase in height in the direction of flow (from right to left).

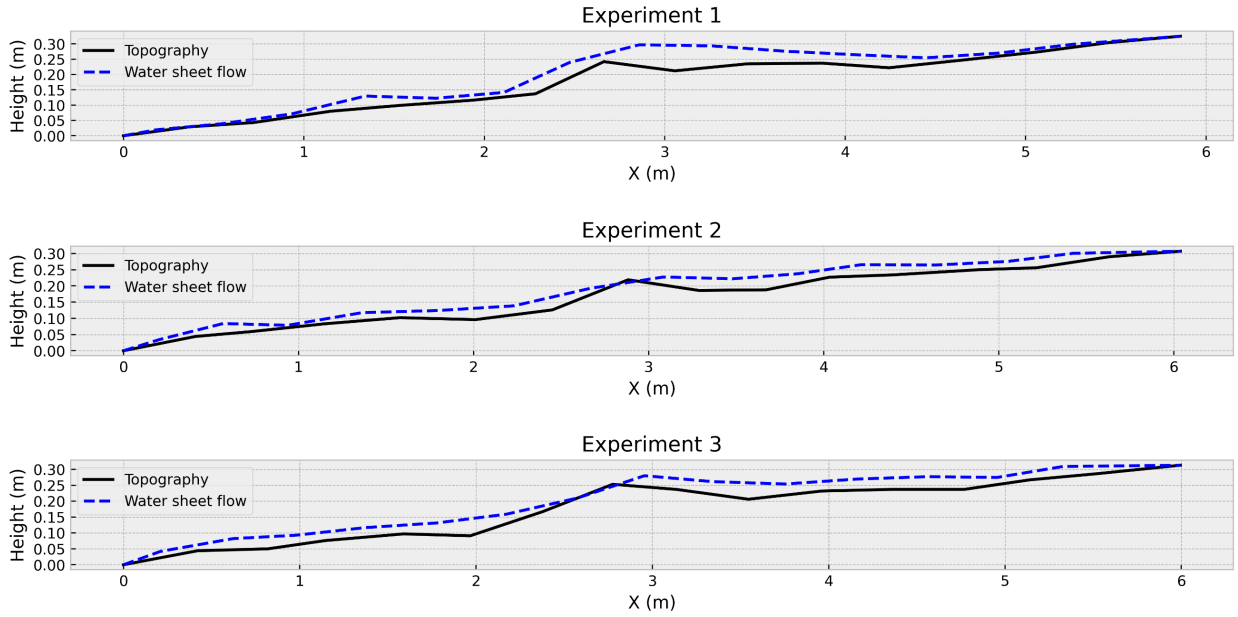

Figure 3-3: Representation of the water sheet flow during every experiment

Electrical conductivity values of the injected water were also measured at different time during the experiments and are summarised in the following Table 3-1. (Different measurements were made during the experiments, the mean of these values has been calculated)

Table 3-1: Electrical conductivity of the infiltrated water for every experiment

Experiment	Mean Electrical Conductivity (mS/cm)	Standard deviation (mS/cm)
1	11.195	0.098
2	13.412	0.124
3	11.868	0.010

To illustrate the disposition of the setup and the overall context, the images from the Figure 3-4 are provided. In these pictures, especially the left picture, the establishment of the water sheet flow is clearly visible with the electrodes directly in contact with the water. Also, on the right picture, the miscanthus and the setup can be observed.

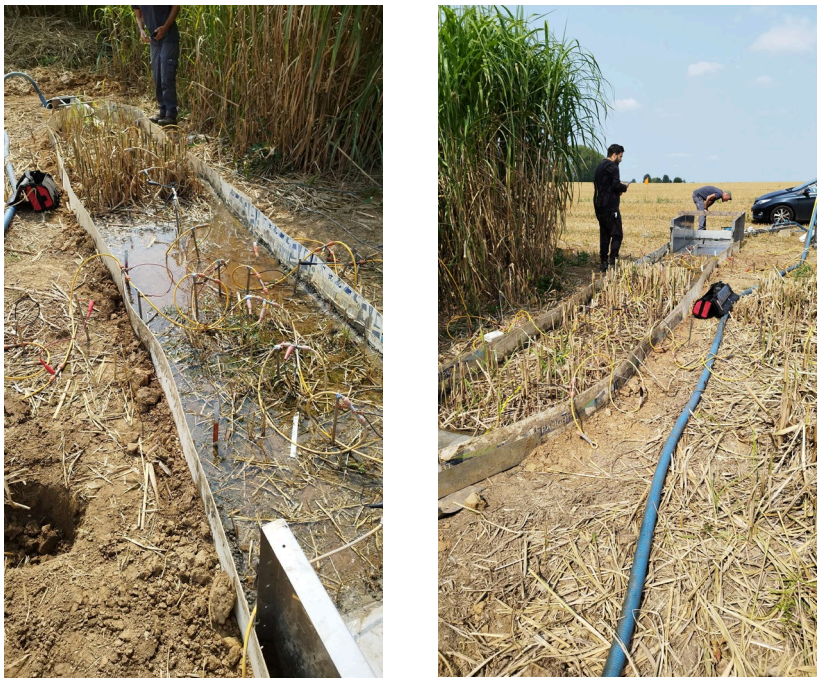

Figure 3-4: Pictures of the setup of the experiment 1

At the end of the infiltration the remaining volume of water in the tanks was measured approximately, for the first experiment the volume infiltrated was estimated at 850L while it was 900L for the two others. These values are not precise values, and the error range is probably large because only the marks on the tanks were used to measure these volumes and the exact starting volume was close to 1000L for each tank but was also not measured precisely. This principally gives an order of magnitude of the infiltrated volume, and what's interesting is that the infiltrated volume for the last experiments was not drastically higher despite the time of infiltration being 50% longer.

3.3.4. Challenges

The main challenge of the experiment is to represent as accurately as possible the infiltration by inverting the acquired data. As previously seen in the literature review, timelapse monitoring of infiltration test can present a few difficulties such as the artifact generation, the inversion scheme processing, or even external factors such as temperature change or in this case the establishment of the water sheet flow. This last factor will be a major challenge concerning the data processing, while this kind of issue is rarely occurring in the already existing infiltration test with ERT conducted. Contrary of classic ERT campaign, the timelapse acquisition will bring the additional challenge of well interpreting transient events by reproducing resistivity profiles and correlating these resistivities with physical phenomena.

3.3.5. Contribution to the State of the Art

As previously mentioned, infiltration monitoring is well studied in the literature, nevertheless, it is often only focused on studying the infiltration itself. Some studies will focus on identifying

the infiltration front and others on the preferential paths depending on the context of their experiment.

In this case, in addition to identifying the infiltration pattern it will also be interesting to make conclusion on the difference in infiltration rates between the parcels with or without miscanthus. This will differentiate this experiment from others, here the infiltration is analysed by comparison of different parts of the profile to be able to determine a relative difference of infiltration. It also differs in its infiltration setup, while some rely on existing infiltration equipment like double ring infiltrometer (Lu et al., 2022), rain simulator (Austin et al., 2017) or simply with a shower head (Blazevic et al., 2020), the setup used in this case was a custom-made runoff infiltration setup that can simulate runoff coming from the upper part of the field. This is a high flow setup simulating extreme conditions.

A further addition is the large number of timelapse measurements taken. While others have usually a large extension of ERT profile, their measurements were only made at specific time before and after the infiltration steps or with large time spacing. In this case, the measurements were made during the entire infiltration process with short steps (~3 minutes), allowing study throughout the entire experiment and of the kinetics of the phenomena.

3.4. *Simulated Experiment with a Numerical Model*

To better understand the expected result of an experiment, a simulated experiment with synthetic data is often conducted using a numerical model. Forward modelling consists of creating a model with known electrical properties and then simulating data from this model to perform an inversion of these data. Thanks to these steps, it is possible to determine if the generated inversion images best reflect reality or if artifacts occur during the inversion process. It also helps for the interpretation, in this case understanding if the decrease in resistivity really represents the infiltration front and at which extension. The main challenge that has been encountered is the effect of the established water sheet flow during the water infiltration phase and how it will affect the result of the inversion. The main question of this section is: Can real variations in resistivity be accurately generated by the inversion process?

3.4.1. Model Description

The objective is to adapt the real case problem to a synthetic and simple model. To do that, the complexity of the resistivity distribution of the soil is neglected and the background model is simply defined as a homogeneous space of a known resistivity of 16 m long (X dimension) and 5 m deep (Y dimension). Then a second model is generated representing the same homogeneous space but with a determined saturated portion of soil from X=0 to 6 m, and with an infiltration front 40 cm deep. For the dimension of the electrode array, it has been chosen to determine similar geometry as the real experiment, i.e., a 6 m long array with 16 electrodes of 40 cm spacing aligned with the saturated zone. On this model, the boundary conditions on an electrical point of view are non-flow boundary conditions (Neumann) on the left, right, and bottom borders, meaning that no

current leaves or enters the system on this border, and mixed boundary conditions on the top border to be able to represent the injection of current at the determined position meaning that current is injected at the electrode positions and no current leaves or enters the model along the rest of the boundary. After simulating ERT data from this model, the same model is adapted to represent the water sheet flow, also simplified compared to the real case, it is simply represented by a 3 cm thick low resistive layer on top of the previous model

The Figure 3-5 represents the synthetic model and the Table 3-1 the precise resistivity values applied to this model. The water sheet flow is not well represented on this graph due to its small thickness compared to the total size of the model:

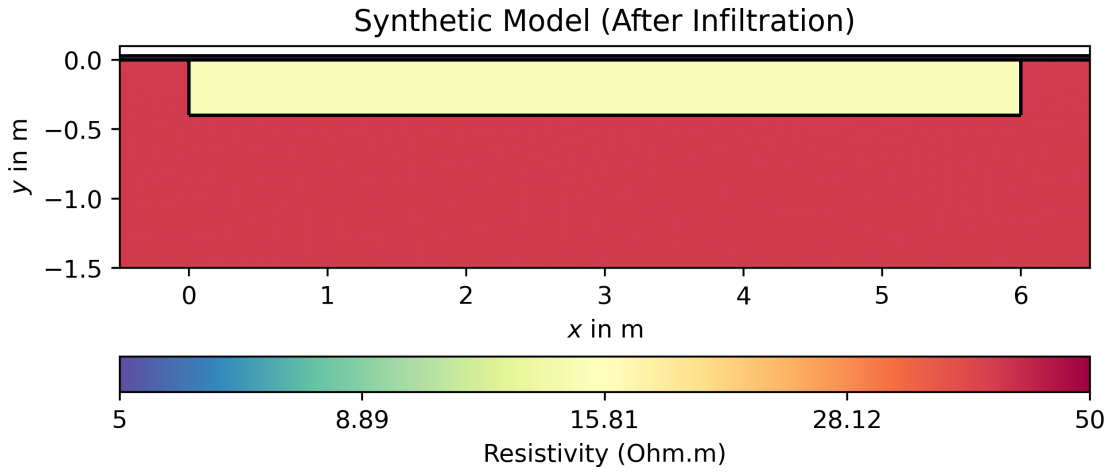

Figure 3-5: Synthetic model determined for the simulated experiment

Table 3-2: Summary of the chosen resistivities of the synthetic model

Zone	Imposed Resistivity (Background) (Ω.m)	Imposed Resistivity (After Infiltration) (Ω.m)
Water sheet flow	1	1
Infiltration front	40	15
Background	40	40

The data are simulated using a Dipole-Dipole coupled with a Gradient array (like the experimental data) and generated by the pyGimli library (Rücker et al, 2017). Electrode positions are located at Y = 0 m and every 40 cm from X = 0 m to 6 m. The electrodes are simulated as point electrodes.

3.4.2. Analysis of the Simulated Data

Once data are simulated the inversion process is basically the same as what is done with the real data (Time-Constrained processing). The precise inversion scheme will be described later because it results from different processing that will be explained. This section is mainly useful to observe the effect of the water sheet flow on a controlled model. Before inverting the data that includes the water sheet flow, the following result is without the effect of this low-resistive layer (Figure 3-6). As expected, this result accurately represent the reality of the imposed model. Nevertheless, the resolution is not perfect, it can be seen with the expected infiltration front (interpreted as the bottom of the decreased resistivity area) is deeper than 40 cm, but this is a result that is coherent when working with only 16 electrodes and a 40 cm spacing between them. There is probably a limitation to represent the real resistivity profile with precision due to the configuration. An isoline of 25% of decrease is also represented.

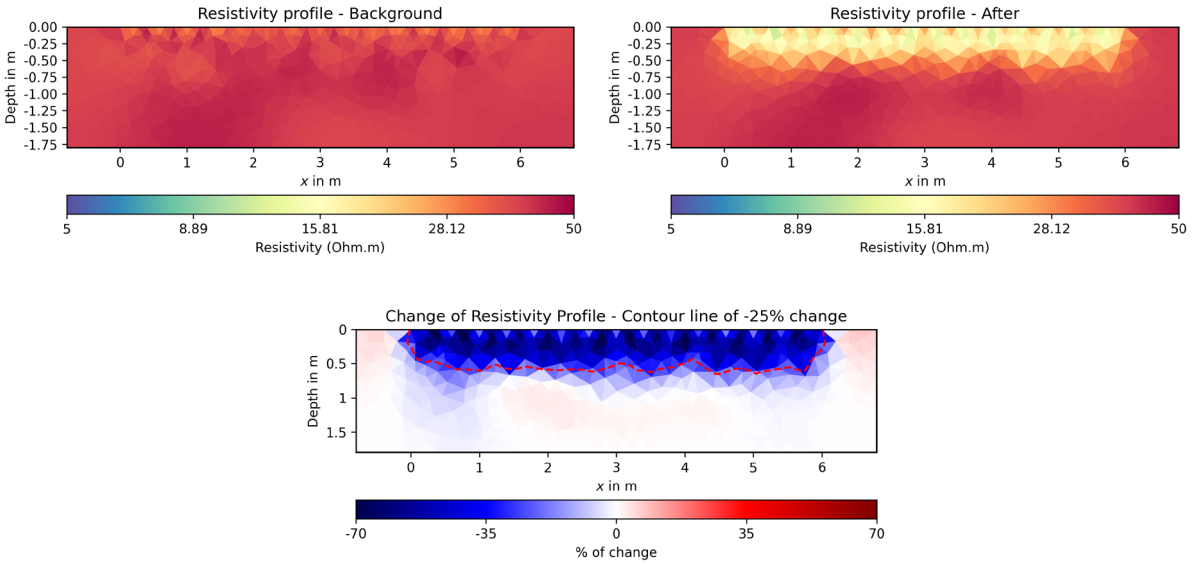

Figure 3-6: Background and After infiltration resistivity profiles and relative change between for the simulated experiment without a water sheet flow (Time-Constrained processing)

This result can be considered as a reference because of the known properties of the starting model and no influence of a low resistive layer on top. This is a similar result to what will be expected when processing the background and after infiltration measurement of the real data.

Once the standard result is obtained, the data are simulated with the presence of the 1 Ω.m layer that is 3 cm thick. In the Figure 3-7, as expected, the result differs from the previous standard model. Indeed, the background resistivity profile fails to represent the reality of the designed model. The effect of the water sheet flow appears as a top layer with falsely low resistivity values, reaching less than 10 Ω.m at the very top. The resistivity change profile reveals an overestimation of the infiltration front with decrease in resistivity reaching a greater depth. Also, due to the lower starting resistivities on the top part, the decrease in resistivity is less important than what was

observed in the standard model. Again, the same isoline as before is present, compared to the previous solution without the water sheet flow, the isoline is present at a greater depth and with a more irregular pattern.

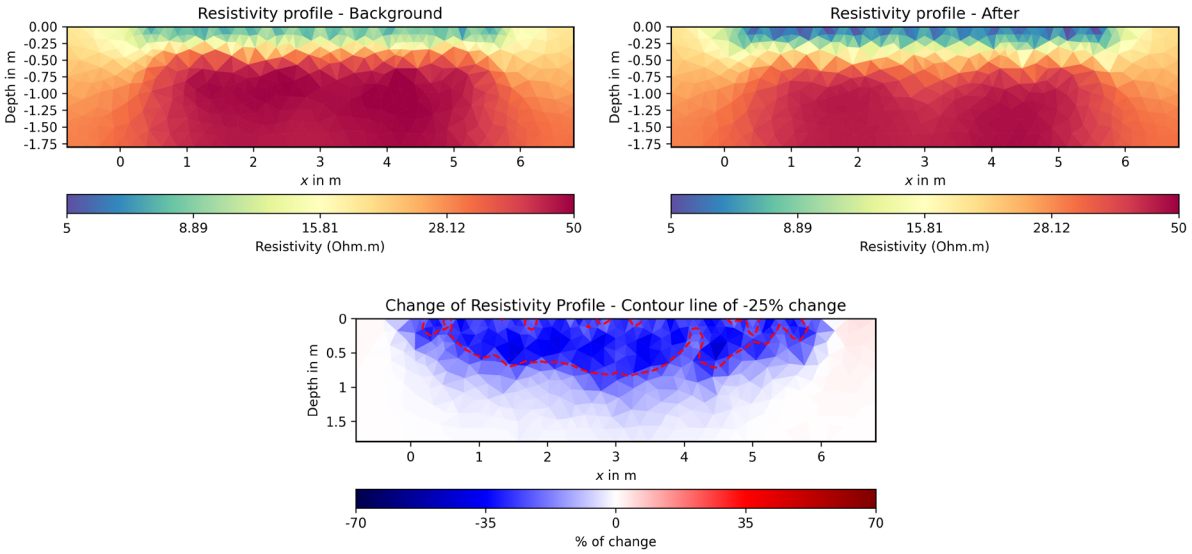

Figure 3-7:Background and After infiltration resistivity profiles and relative change between for the simulated experiment with the water sheet flow representation (Time-Constrained processing)

These results revealed that the inversion results of the measurements realised during the infiltration test, i.e., with the water sheet flow established, cannot be quantitatively interpreted because of the misrepresentation of the upper part of the profile due to the influence of a low resistive layer on top, in this case salted water. A solution that can be introduced to try to reduce this effect is the region regularization, i.e., introducing in the inversion model the calculation of the resistivity of a top layer with decorrelation between this region and the soil region, this model is define with the same geometry as the synthetic model. This model can also be completed by imposed range of resistivity values to the model so that only resistivities of this range can be calculated. To do that the water sheet flow region is constrained to be between 0.5 and 1.5 Ω.m and the rest of the profile can take values between 10 and 2000 Ω.m to not over constrain the model. With this processing of the data the background profile is improved with a reduced decrease in resistivity on top of the profile but is still biased by the influence of the low-resistivity layer (Figure 3-8).

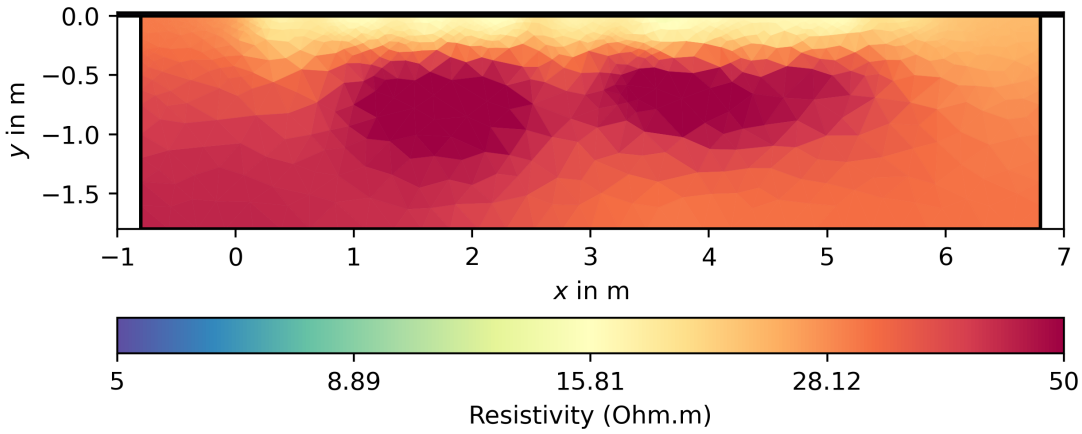

Figure 3-8: Background resistivity profile of the simulated with the water sheet flow and region-wise regularisation

Despite a slight improvement of the calculated model, it has only been possible to generate the background with this method due to issues applying the other types of regularization (time constraint, starting and reference model) with this processing making it difficult to use with timelapse processing.

A limitation of the constructed forward model is the simulation of the electrodes. Electrodes are simulated as points at the surface of the model (Y = 0 m), while real electrodes are linear and embedded in the ground, with part of it directly in contact with the soil, another part with the water and the rest with the air. Consequently, more current is expected to flow into the soil thanks to the embedded electrodes. Nevertheless, this forward model still gives an idea of the misinterpretation that can be expected in the processing of the real data.

3.5. *Data Quality*

To assess the data quality of the measurements, reciprocal data are usually used. Theoretically, if a measurement is made with electrodes AB where the current is injected and MN where the voltage is measured, when inverting the injection and measurement pairs, the resistance retrieved must be equal. From the reciprocal data it is then possible to estimate the error by comparing the normal measurement with the sampled reciprocal data, i.e., an additional measurement with only a limited number of datapoints but with the injection and measurement dipoles inverted. A small error of the data assures a good quality. The quality of the background and after measurements are assessed first.

There are many solutions to display the results of the reciprocal analysis of a dataset. The first graphs that are displayed are comparisons on a log-log graph of all the common datapoints between normal and reciprocal measurements. Perfect quality of these will display all the points on the identity line on the graph, the further the points are from the identity line, the more reciprocity is not guaranteed, meaning the final solution depends on the choice of the injection or measurement dipoles.

The first graphs of the Figure 3-9 represents the reciprocal analysis of the background and after measurements of the longitudinal profile, in every plot, a trend line of all the points is shown, the parameters **a** and **b** of the trend line equation are also calculated using the corresponding formula:

$$R_{reciproc} = a * R_{normal} + b$$

The quality is better when **a** is close to 1 and **b** to 0, i.e., when the trend line is approximating an identity line.

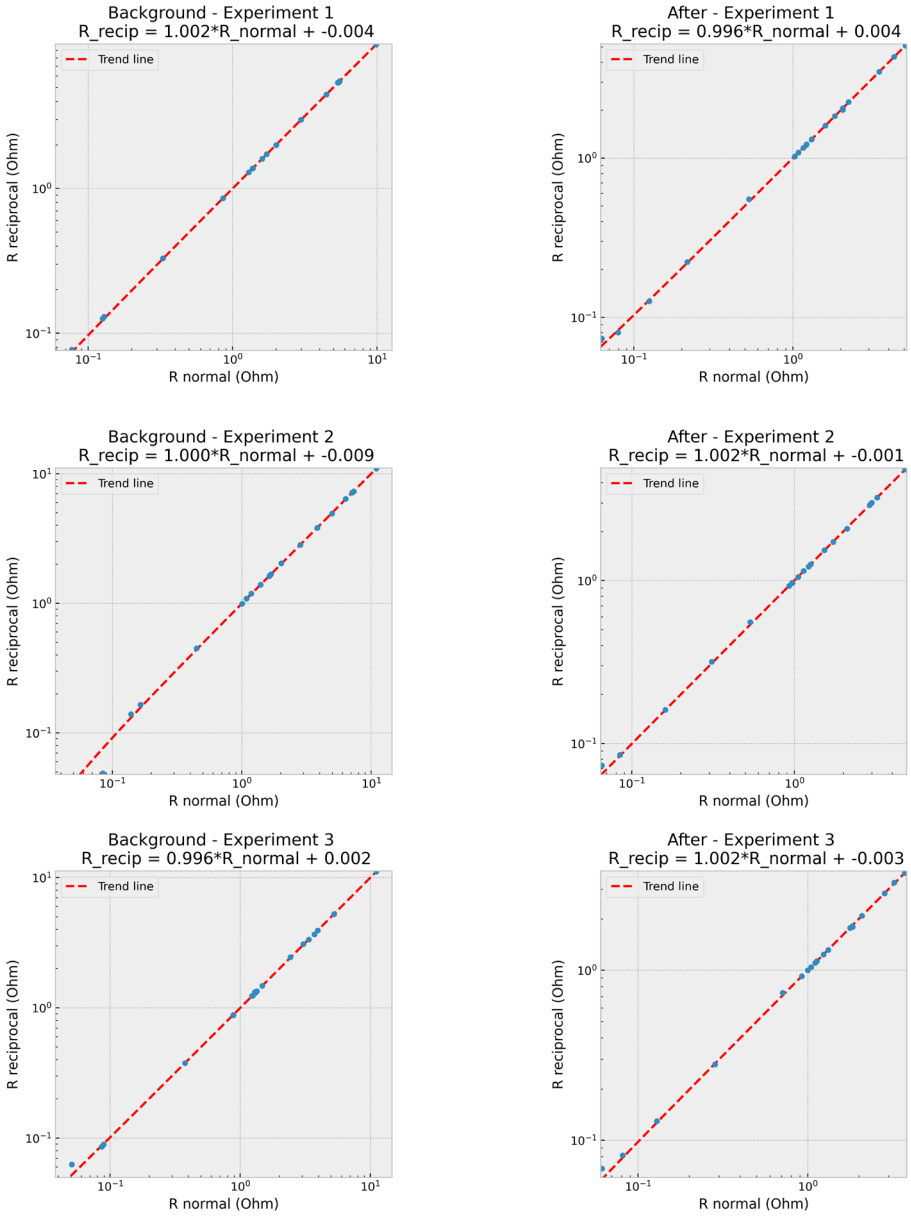

Figure 3-9: Resistance comparison of normal and reciprocal measurements for every experiment Background (Left) and After Infiltration (Right) measurements

Because reciprocal data were also taken during the timelapse automated acquisition, the reciprocal analysis was also performed on these measurements. Nevertheless, due to a short timestep between the normal acquisition and the reciprocal acquisition and considering that the environment is constantly changing because of the infiltration, small errors in the reciprocal analysis may be caused by this. The analysis is focused on the evolution of the **a** and **b** parameters of the trend line. As it can be seen on the Figure 3-10, both parameters diverge from the ideal values (respectively 1 and 0), but the difference in parameters is mainly observed for the data during the infiltration, effect probably caused by the aforementioned reason. In absolute, both parameters do not have extreme values and stay close to the wanted values, which implies overall good quality of the different data, in general when looking at the plots for every timesteps, points are very close to the identity line indication good data quality.

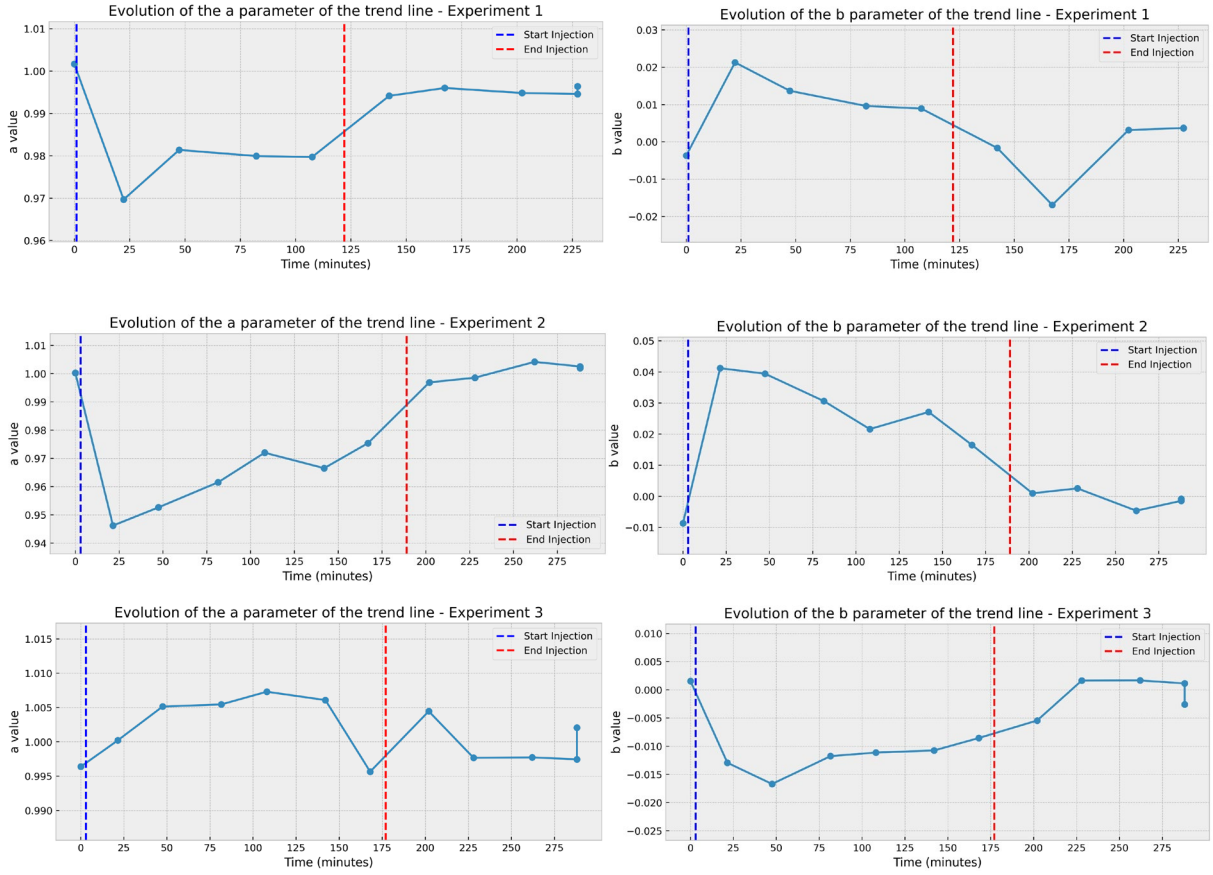

Figure 3-10: Evolution of the a (Left) and b (Right) parameters of the trend line of the resistance comparison of normal and reciprocal data for the timelapse measurements

Some points of low resistance are often distant from the identity line, and this variation can be seen on the next plots (Figure 3-11), they represent the relative variation of resistance between the normal and reciprocal data as a function of the mean resistance of the reciprocal and normal measurements. This concerned almost only one datapoint of low resistance and seems to be present in many profiles, these points are plotted as having a high relative error but have generally a similar

absolute error. Nevertheless, most datapoints have a repetition error smaller than 3% and rarely exceeding 5%. These error ranges can be acceptable even if a lesser error is often preferable, this can be partially explained by the parameter of acquisition that have been optimised to reduce the acquisition time to acquire more timelapse frames. Some of these parameters are the number of stacks per datapoint, which was set to two, the acquisition time, i.e., the time the current is injected, or also the maximum current intensity fixed at 50 mA to avoid overusing the battery and to enable measurements throughout the entire experiment.

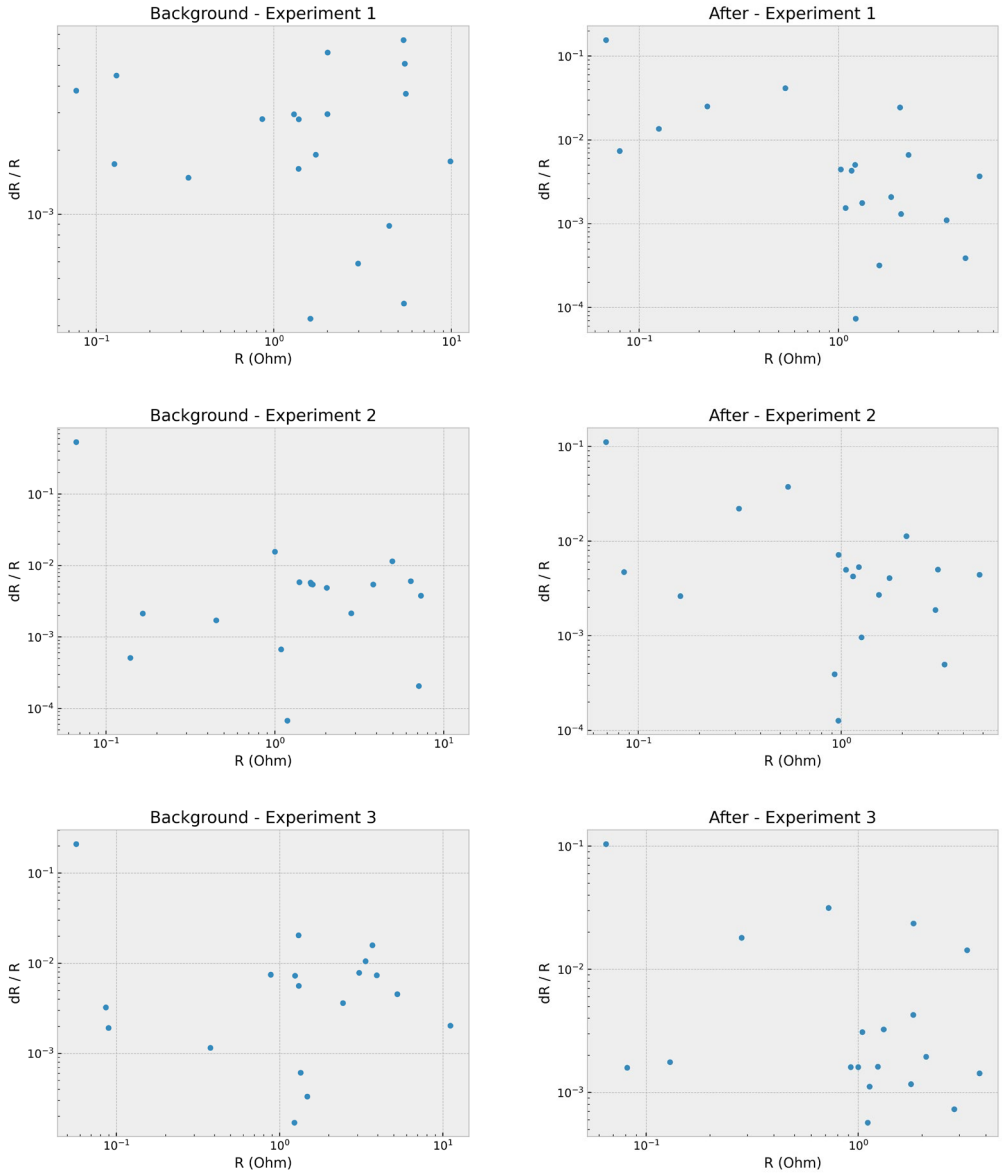

Figure 3-11: Reciprocal error in function of the resistance for Background (Left) and After-Infiltration (Right) measurements of each experiment

With these previous figures, an error model can be retrieved, but the limited number of datapoints for the reciprocal measurements do not allow an exact estimation of the error model, especially with the outliers of low resistivity discussed previously.

Another form of representing this error is by histograms (Figure 3-12), despite having a limited number of points it is also possible to see that the error is mostly less than 5% and for some acquisitions even less but there is often one datapoint having a really high error, this points is the same point related to an overall low resistivity that has been discussed in previous paragraphs and is not represented in the following histograms to better represent the overall distribution. It has been observed that this high error point never appears in the first experiment.

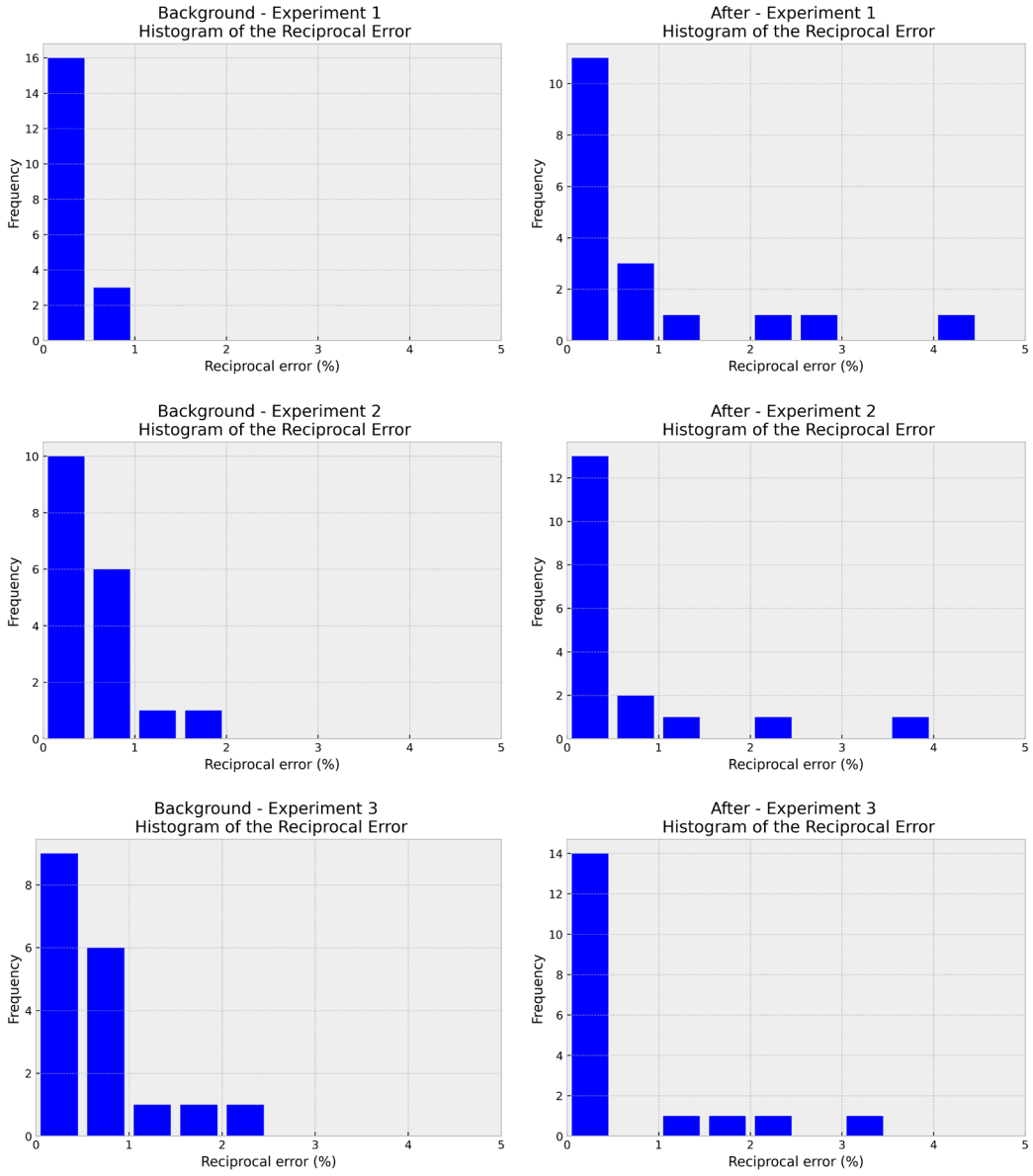

Figure 3-12: Histograms of reciprocal errors for Background (Left) and After-Infiltration (Right) measurements of each experiment

The reciprocal analysis is here focused on the longitudinal profile, but the perpendicular profiles data quality have also been processed. The conclusion are the same, sometimes one or two outliers can appear, but the data generally present a good quality like the longitudinal profile.

3.6. *Apparent Resistivity Study*

Before proceeding to the inversion of the acquired data, it is good to analyse the apparent resistivities and already try to distinguish differences between the two halves (with or without miscanthus) and the overall effect of water infiltration on the apparent resistivities. To calculate the apparent resistivities, geometric factors (κ) must first be calculated to transform the measured resistance (Everett, 2013).

The apparent resistivities can then be easily calculate by multiplying the geometric factor by the measured resistance. The analysis focuses on the mean apparent resistivity of the overall profile but also for each part of the profile (in or out of the miscanthus parcel). This mean is calculated for every measurement as a function of time.

The Figure 3-13 shows this evolution of the mean apparent resistivities over time for all repetitions. As expected, the injection of water has a direct effect on the resistivities because they are directly decreasing. On these graphs, it is also visible that the injection has been started a bit later for the second and third repetition (after 2 measurements) while it has been directly started after the first measurement for the first repetition. Also, the end of injection, which happens earlier on the first graph, is visible as a sudden increase in resistivity. This increase is assumed to be linked to the disappearance of the water sheet flow that has already been mentioned. Indeed, it is logical that this body of salted water had a direct effect on the measured resistivity due to its high conductivity, a large part of the decreasing resistivities at the start is probably induced by this establishment. The last observations of these graphs concern the distinction between the different parts of the bands, the distinction has been made by calculating the mean position of the AB, MN electrode dipoles and sorting when it was situated in the miscanthus part or not. While this method allows to have a distinction between the zones, these values are principally indicative and not quantitative because they represent the value of the resistivity at theoretical points but can be influenced by the surrounding soils that is for some point not in the attributed half of the profile. The starting resistivity is always greater in the miscanthus than in the bare soil part, but the decrease in resistivity within the miscanthus is more pronounced especially when comparing the starting and ending values. For the first profile, during the experiment, the absolute mean in the miscanthus becomes smaller than the mean in the bare soil zone showing a greater decrease while for the other repetitions lines are almost blending during the infiltration despite the higher starting value of the resistivities from the miscanthus half. Before 25 minutes of injection, the slope of the miscanthus line is steeper, showing a possible greater kinetic of infiltration in the first minutes of the experiment.

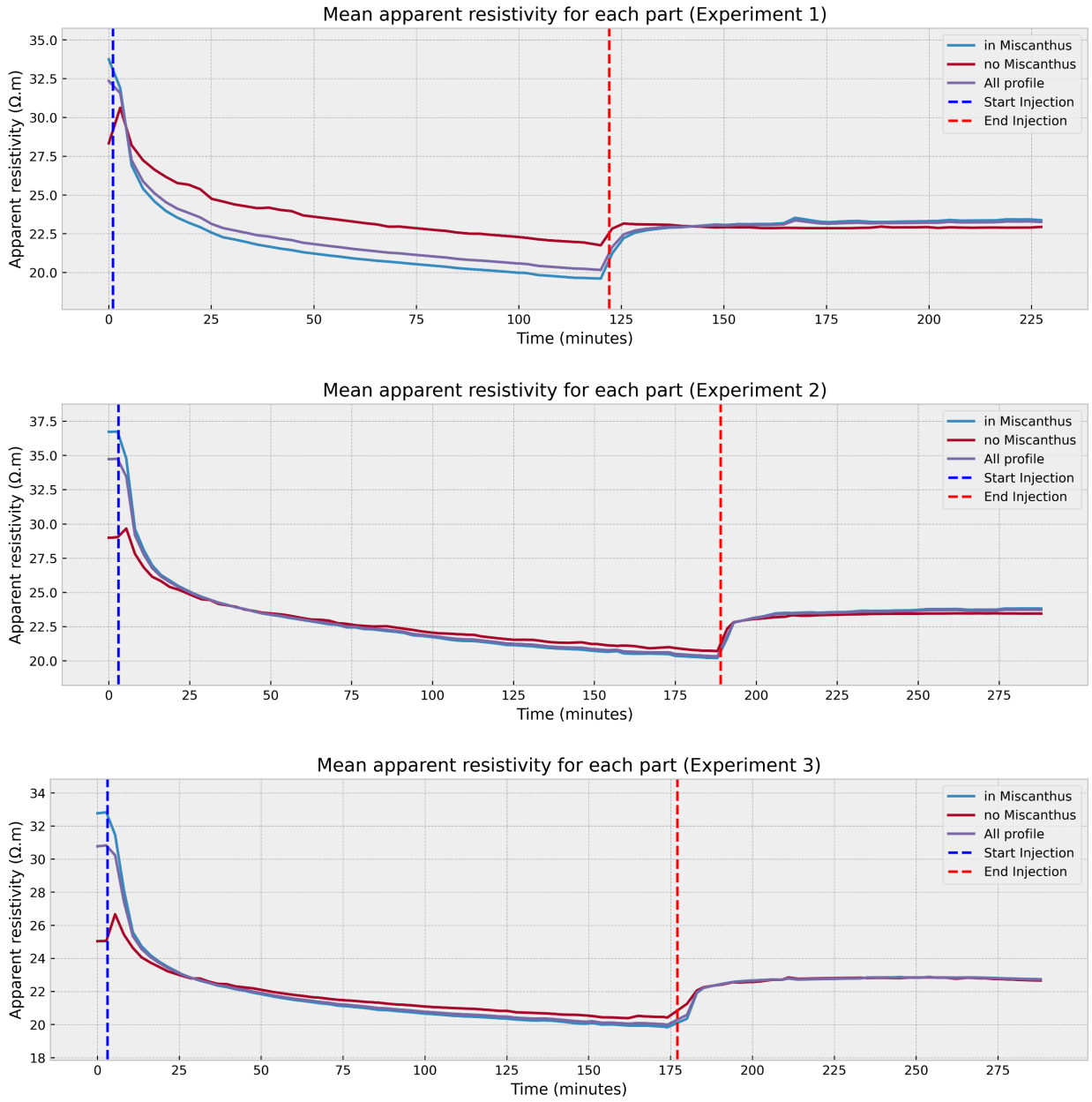

Figure 3-13: Mean apparent resistivity evolution with time on the overall profile and for pseudo-points in or out of the Miscanthus for each experiment

Another way to observe the evolution of resistivity is by the median of all apparent resistivities (Figure 3-14). The evolution of median follows the same overall decrease as observed in the mean evolution. The first experiment differs from the others especially due to the lesser decrease in the bare soil part of the profile such evolution was present on the mean graph but is more accentuated by the median plot. This accentuation of the lesser decrease is also present in the two other experiments, confirming that there is a quicker dynamic of resistivity decrease in the miscanthus part.

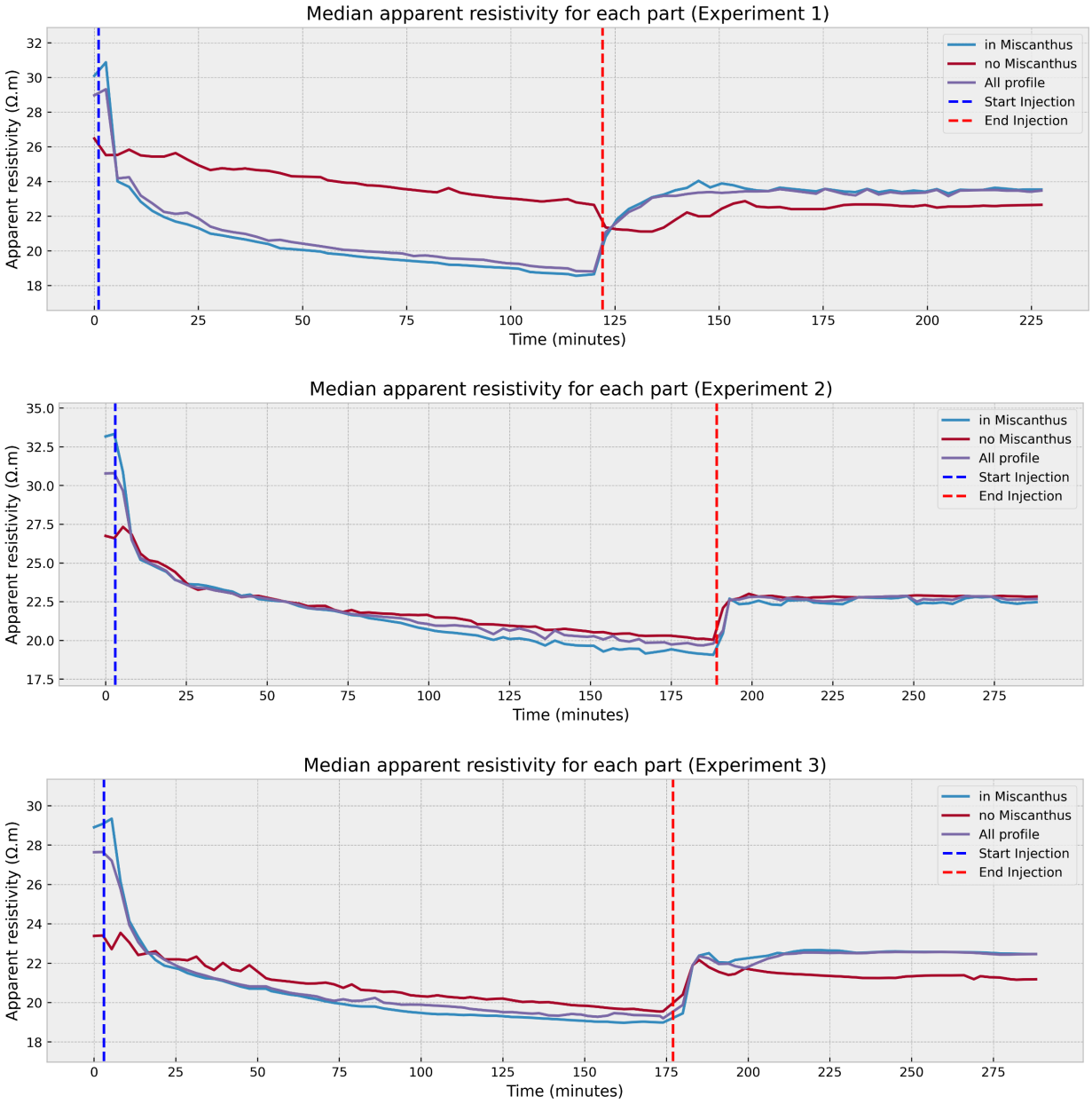

Figure 3-14: Median apparent resistivity evolution with time on the overall profile and for pseudo-points in or out of the Miscanthus for each experiment

To better observe the difference in decrease between both parts, the graphs of the mean decrease in the apparent resistivities are plotted on the Figure 3-15. The plots, in addition to showing the higher decrease in the miscanthus zone, also show the good repeatability of the data from the 3 different repetitions because all plots show similar result with same order of magnitude in mean apparent resistivity decrease values. Nevertheless, it cannot yet be concluded that a greater decrease in resistivity implies a greater infiltration especially when the starting resistivity is higher. A discussion about the interpretation of decrease in resistivity will be developed in further sections.

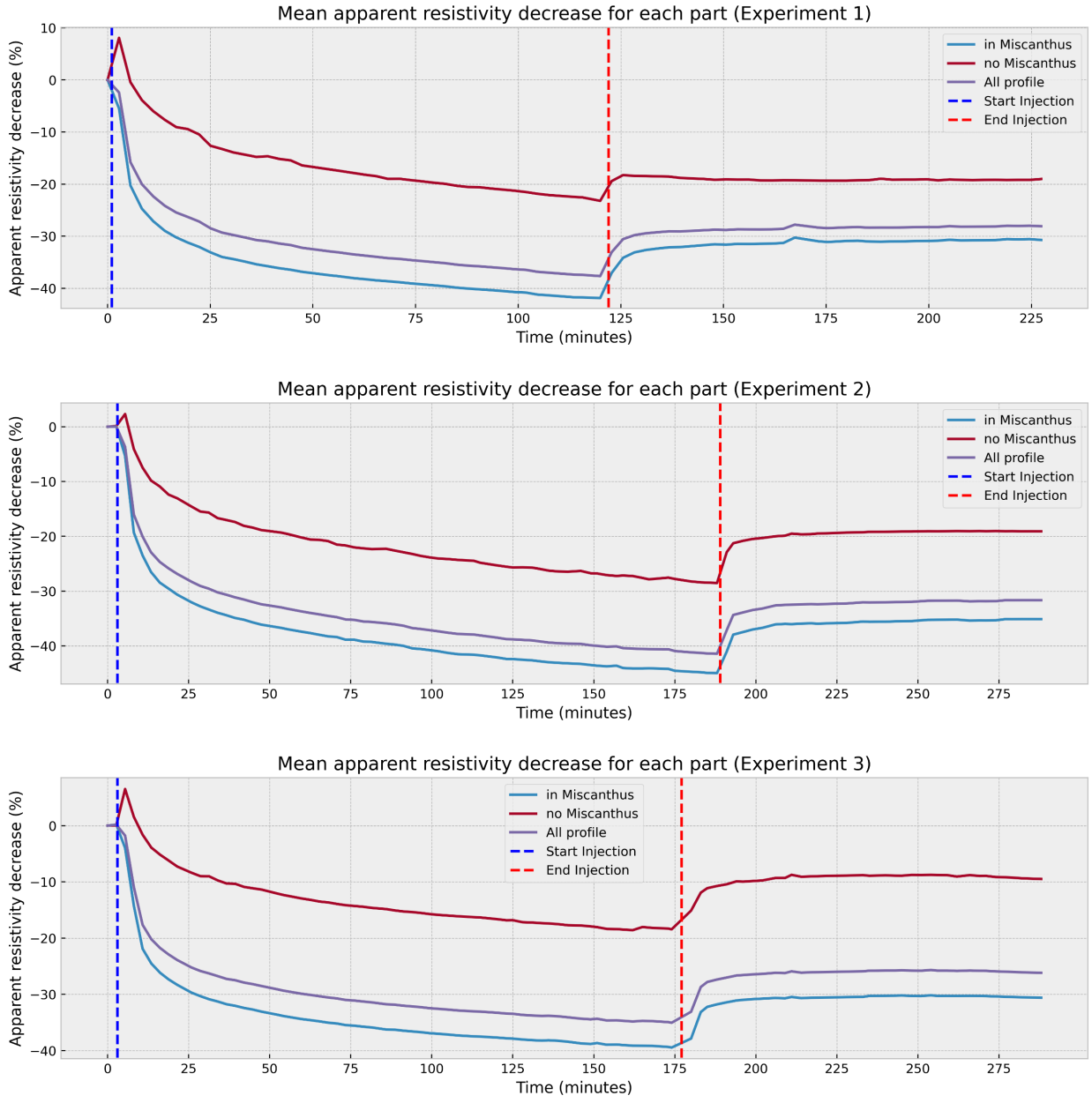

Figure 3-15: Mean apparent resistivity decrease evolution with time on the overall profile and for pseudo-points in or out of the Miscanthus for each experiment

Standard deviations are also fluctuating with time, the 3 Figures are present in the Annexe 2. They usually increase when the water sheet flow is establishing and then decrease until the end with a sharp decrease when the injection is stopped and the water sheet flow disappeared.

Apparent resistivities from the perpendicular profiles can only be analysed with before and after measurements, meaning that it is not possible to describe the dynamics of their evolution but only a relative difference between the start and the end of the experiment (Table 3-3). As with the longitudinal profile, it is often observed a greater final decrease in resistivity in the miscanthus part than what is observed in the other part but there is still an overall greater starting resistivity in the Miscanthus part. In contrast to the longitudinal profile, the standard deviations are greater after the infiltration, this is probably because on the perpendicular profiles, the water is only injected on a 1 m wide region while on the longitudinal one water was infiltrated all along the profile. This effect creates heterogeneity along the profile: while the borders remain dry, the centre becomes wet.

Table 3-3: Apparent resistivity analysis of the Background and After measurements of the perpendicular profiles in or out of the miscanthus

Experiment	Perpendicular profile	Background (Ω.m)			After (Ω.m)			Decrease (%)	
		Mean	Median	Std	Mean	Median	Std	by Mean	by Median
1	Miscanthus	33.11	32.18	10.99	26.44	22.21	13.10	-20.16	-30.97
	No Miscanthus	25.50	24.19	7.04	20.82	18.24	8.33	-18.38	-24.57
2	Miscanthus	34.04	32.17	12.28	27.12	22.09	13.96	-20.33	-31.34
	No Miscanthus	28.03	26.50	6.92	19.75	18.02	7.15	-29.56	-32.00
3	Miscanthus	25.97	25.10	7.70	21.57	18.93	9.14	-16.94	-24.56
	No Miscanthus	20.12	20.09	4.71	17.06	15.76	6.50	-15.19	-21.58

3.7. *Standard Inversion Processing*

3.7.1. Initial Conditions Results

Background inversion results can be processed first before proceeding with the timelapse processing. It can be first interpreted independently to see if any points of interest can be identified. The inversion process is a simple inversion with the regularization factor (λ) set to 100 and a data error fixed at 1% for the background, this processing gives good results with an average RRMS close to 0.5% and often converges quickly with only a few iterations.

Static images provide information about the starting conditions of the 3 repetitions of the experiment. The interpretation is important to discern the heterogeneity of the soil and the differences that exist between the two parts of the profile without considering the hydraulic properties at first.

Before analysing the longitudinal profiles (Figure 3-16), it is important to remind that the separation between the miscanthus part and the bare soil part is at X = 3 m, with the miscanthus on

the left side. The three profiles have similar resistivity distribution, being a good sign for the repeatability of the experiment because the starting conditions are similar.

Concerning this distribution of the resistivity, high resistive areas can be distinguished from the rest of the profile by their red colour. These zones are present on the surface of the profiles mainly on the left part, this resistive layer is more important between 2 and 3 m where it reaches up to 50 cm in depth. The extent of this high resistive layer is mainly concentrated in the miscanthus (0 to 3 m) but also overlap on the bare soil part, but very high resistivities are often limited to X = 4 m, nevertheless, even after this distance, the top part soil (30-50 first centimetres) is still more resistive than deeper soil.

This higher resistive layer can be influenced by several factors, firstly, the miscanthus, as previously mentioned in the introduction about miscanthus, root and rhizomes of miscanthus have a direct effect on the soil structure and cohesion. These influences on the soil structure in additions of the roots and rhizomes itself have a direct effect on the resistivity of the soil resulting in higher resistivity in those areas. A second effect that can explain this heterogeneity in resistivity is the plough pan, a layer of dense material resulting from heavy machinery passage when labouring the soil, it his often located a few decimetres deep. The soil has not been laboured since a long time because the miscanthus is a perennial plantation but probably was before, so a denser layer can be present beneath the top layer of soil, which may explain what is seen here and why there is also a presence of higher resistivities in shallow depth of the bare soil part. This interpretation is supported by in situ observations where during the last experiment, a trench was dug and difference in soil compaction was clearly visible at an approximate depth of 40 cm. Also, the contrast of this top layer between miscanthus soil and bare soil is possibly partially due to a difference of water content, because miscanthus theoretically maintains a lower water content in the soil (Winkler et al., 2020). It is also possible to distinguish an eventual second distinction between two horizons at approximately Y = 149.5 m where resistivities increase with depth but not as much as the top resistivities. This observation is mainly present on the two first profiles.

Despite the strong similarities between the profiles, some distinctions can still be discussed. From the observations just made at end of the previous paragraph, for the experiment 3, this distinction of the bottom layer is probably biased by the two areas of low resistivity especially noticeable on the right side of the profile at Y = 150 m. Because the last experiment was operated between the first and second one, the injection of salted water may have migrated horizontally, especially in the bare soil part, and thereby biased the background of the last experiment at depth, this effect of infiltration pattern in the bare soil part will be discussed further in following sections. For the other differences, the pattern of the high resistive top layer is similar between the profile, but it seems to have a slightly deeper extension in experiment 1.

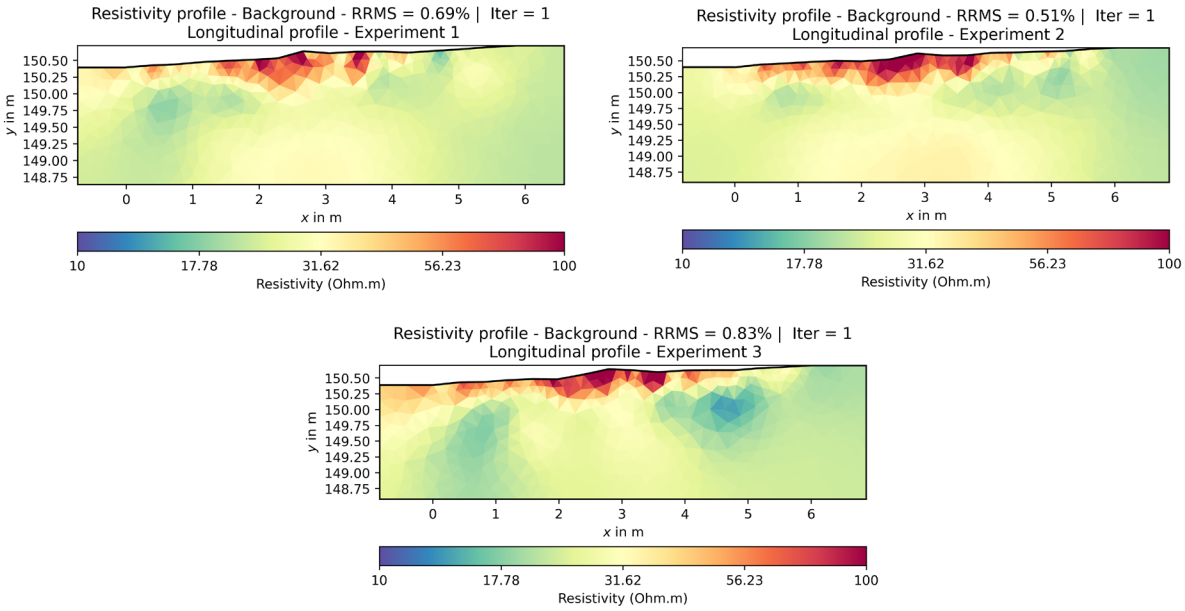

Figure 3-16: Initial conditions (Background) resistivity profiles of the longitudinal profile for each experiment

To confirm the different information retrieved by the analysis of the longitudinal profiles, the perpendicular initial conditions profiles are investigated. As a reminder, the two different profiles are 4.5 m long with 0.3 m electrode spacing and located in the middle of each part of the profile, i.e., at approximately x = 1.5 and 4.5 m on the longitudinal profiles. Like longitudinal profiles, inversion results for background have acceptable error (RRMS < 1.25%). These errors could be qualified as too low compared to the data quality, the risk is that artifacts could be created from the very start and not be reflected in the RRMS because of the data quality.

Figure 3-17 illustrates the inversion results for the perpendicular profiles, with the profile within the miscanthus on the left. As previously observed, a distinction of different horizons can be retrieved and confirmed. At approximately 150.25 m in depth, the resistivity decreases. The more resistive top layer is also more resistive in the miscanthus than in the bare soil profile. For the second distinction deeper, it is also visible but particularly on the profile not in the miscanthus where a change in resistivity can be observed from Y = 149.75 m for the first experiment and slightly deeper for the second.

On all profiles the traces of the plastic boards used to delimit the infiltration band are visible, they are located at X = 1.75 and 2.75 m. These boards have a direct effect on the soil structure in the data by creating a region of lower resistivities and due to the addition of bentonite that assures sealing of the boards to delimit the band.

Concerning the third experiment, the influence of both previous experiments is visible on the edges of each profile, large zones of very low resistivity are present before X = 1 m and after X = 4 m due to the proximity between the experimental bands. These background conditions do not reflect the natural soil state, infiltrated salted water has a direct influence on the soil resistivity by decreasing it. Particularly on the profile outside the miscanthus, it can be seen that the bluish area extends vertically but also horizontally as suggested on the longitudinal profile of the same experiment. Nevertheless, for shallow depth and inside the infiltration band the resistivity is similar to the previous experiments.

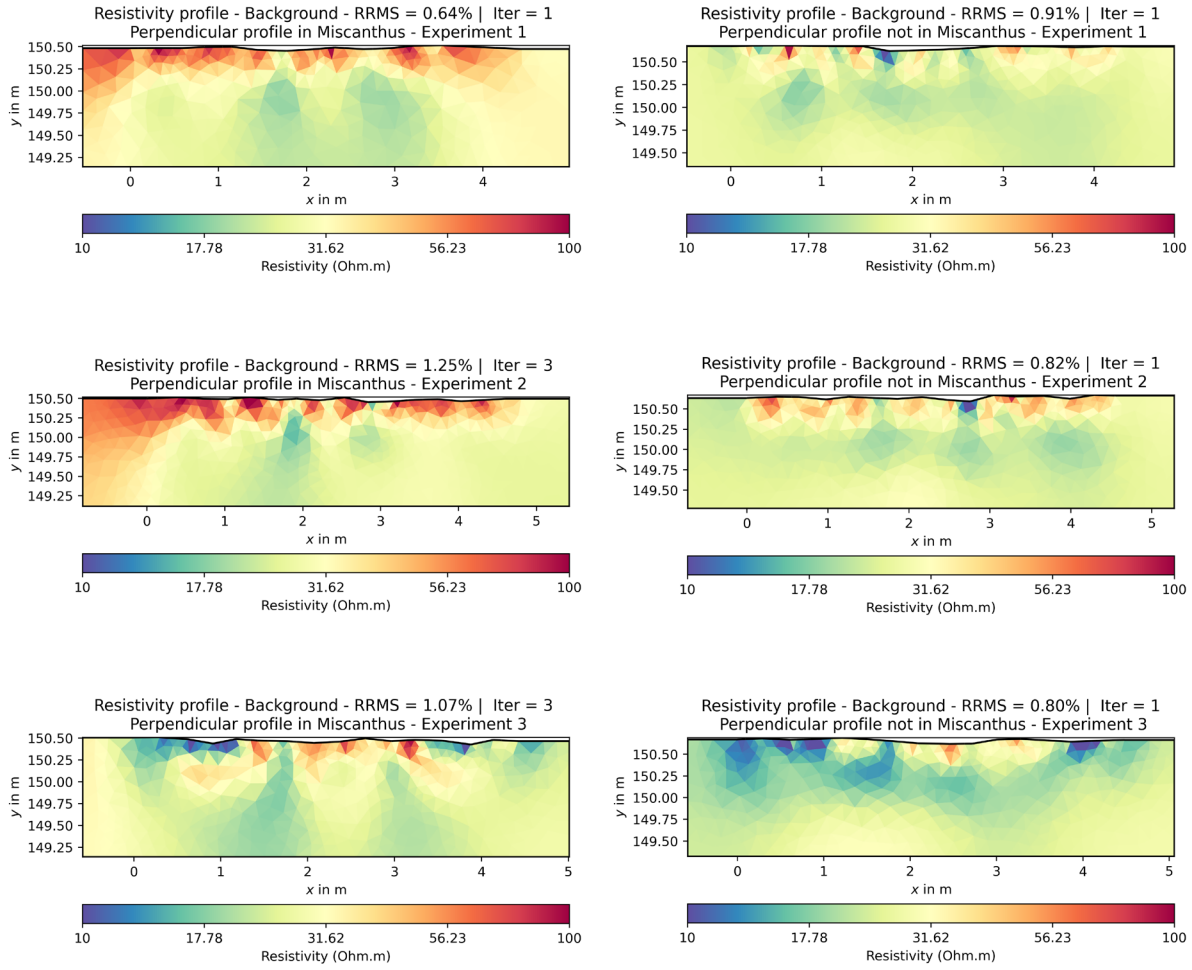

Figure 3-17: Initial conditions (Background) resistivity profiles of the perpendicular profiles in (Left) or out (Right) of the miscanthus for each experiment

To conclude the initial conditions analysis, the major point of interest is this higher resistive layer of approximately 30 to 50 cm. It is particularly more resistive in miscanthus, which influences the structure of the soil. This differentiation between the two parts of the profile is already observable prior to infiltration, it is therefore important to understand that a difference of resistivity during the infiltration process can be directly due to its starting resistivities, which are not

homogeneous and then could impact the interpretation of a relative resistivity decrease. This aspect of interpretation is further discussed in Section 3.9 of this work using petrophysical relations.

3.7.2. Before and After

As a first assessment of the infiltration on the different profiles, timelapse processing is performed on the final measurements of each experiment. This is an effective way to characterize the final state of the infiltration and any potential problems with inversion processing that can occur before processing a large quantity of data. The standard processing consists of using as background the results previously interpreted in the previous section, with these images it is possible to constrain the inverse problem for the processing of the after-infiltration measurement. The applied constraints are a starting and reference model corresponding to the background and a first-order spatial smoothing constraint.

Figure 3-18 reveals the results of this inversion for the longitudinal profiles with the after-experiment results and the relative change between the background previously shown. Resistivity profiles after infiltration reveal a completely different pattern than what was observed on the background results. Indeed, the top resistive layer is no longer visible on the profile, but a low-resistive layer with a different geometry is present, this is the direct effect of infiltration of water, reducing the resistivity of the soil.

When looking at the differences between background and after experiment, this decrease in resistivity can be quantified and highlighted. Nevertheless, the decrease in resistivity is not the only observation that can be made, indeed, increase in resistivity can be observed beneath what is assumed to be the infiltration front. Physically, an increase in resistivity can be explained by different phenomena like the effect of drying soils (Haaken et al., 2016), a temperature effect (Zhao et al., 2020) or even biogas migration in the case of landfills (Clément et al., 2010). Since water is infiltrated, there is no reason that soil dry beneath the infiltration front, a slight temperature effect can be induced by the infiltration of water but the water has an overall temperature close to 20°C and these soils at this period of time do not have major temperature difference compared to injected water and furthermore, the water is not reaching this depth according to the first estimations of the infiltration and of course, no biogas migration is expected because this is an agricultural field. The explanation for this increase in resistivity is therefore not physical but is induced by the processing, these areas are artifacts. As previously detailed in the literature review a lot of studies have reported these types of artifacts in infiltration timelapse monitoring: (Blazevic et al., 2020; Fernández de Vera et al., 2017; Haaken et al., 2016; Austin et al., 2017; Clément et al., 2009; 2010) and some of these authors also developed various types of inversion regularization to try to be exempt of these artifacts. Some anomalies are also present on the surface of the profile, while some cells have no variation from one frame to another (white cells in the resistivity change profiles) and others increase in resistivity, this can be due to electrodes interferences and also by artifacts creation.

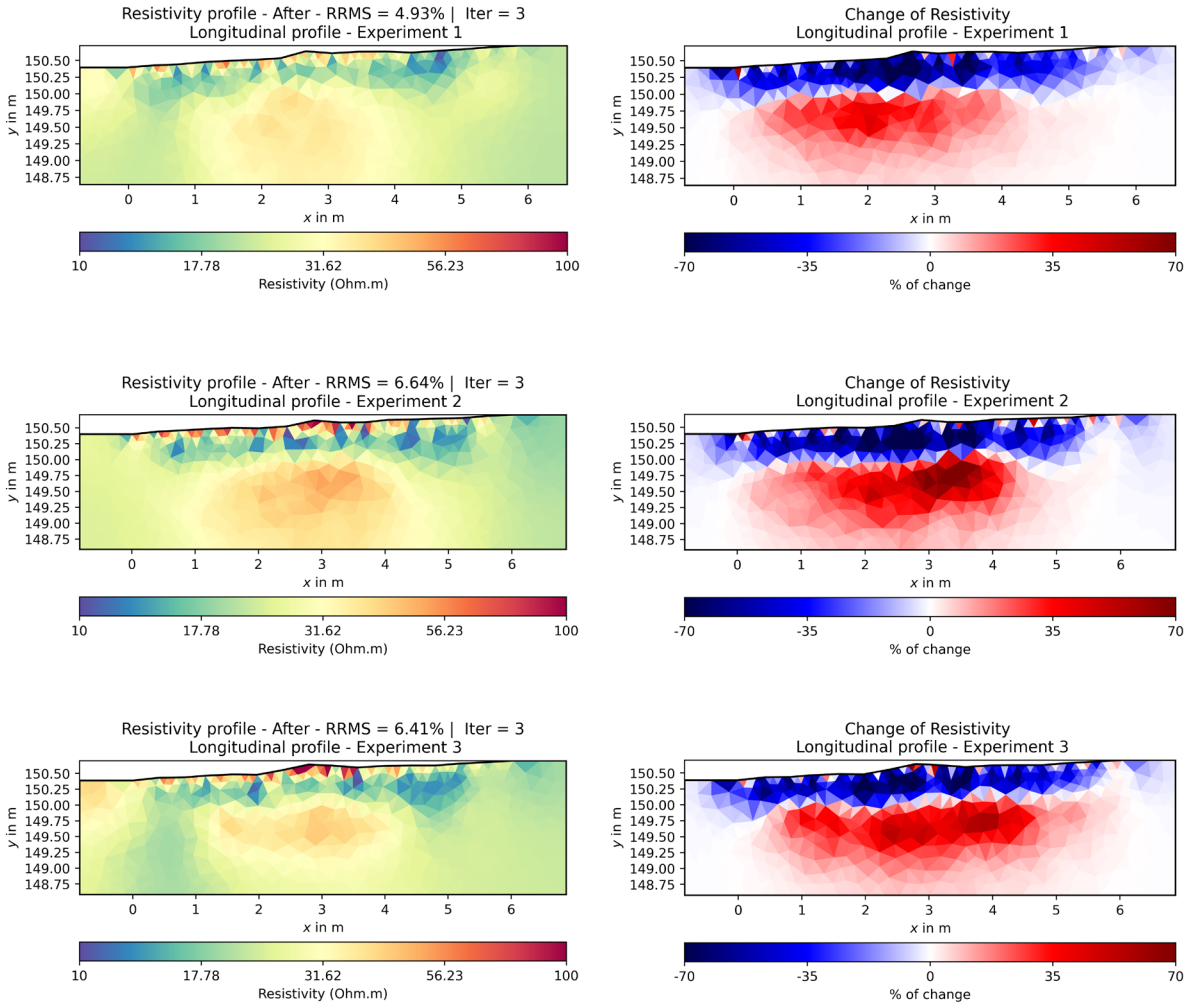

Figure 3-18: After-Infiltration resistivity profiles (Left) and change of resistivity compared to the Background (Right) of the longitudinal profile for each experiment

It is important to mention that these artifacts become more prominent when reducing the regularization factor (λ) reaching increases of several hundred percent in resistivity (reduction of the smoothing).

The same inversion processing was repeated on the perpendicular profiles (Figure 3-19 & Figure 3-20). These results also possess large artifacts of high-resistivity artifacts below the infiltration front but also at the sides of the infiltration band for the second experiment. Artifacts are again present on the surface cells. Decreases in resistivity are visible on sides of the profiles but with lower absolute values than where infiltration occurred in the middle of the profiles, this is important to distinguish these false zones of decrease to avoid misinterpreting them as infiltration, in this case due to their lower value, a simple threshold of resistivity decrease can be applied to mask them. Another observation on these profiles is that artifacts tend to be less present on the profile that is not in the miscanthus half.

Because only 1 m of these profiles is in the infiltration band, neither side of the profile is influenced by the infiltration, at least on the surface, and this is important to see that the observations compared to the background images with the upper more resistive layer are the same on the resistivity profile except in the third experiment, which is influenced by the earlier ones.

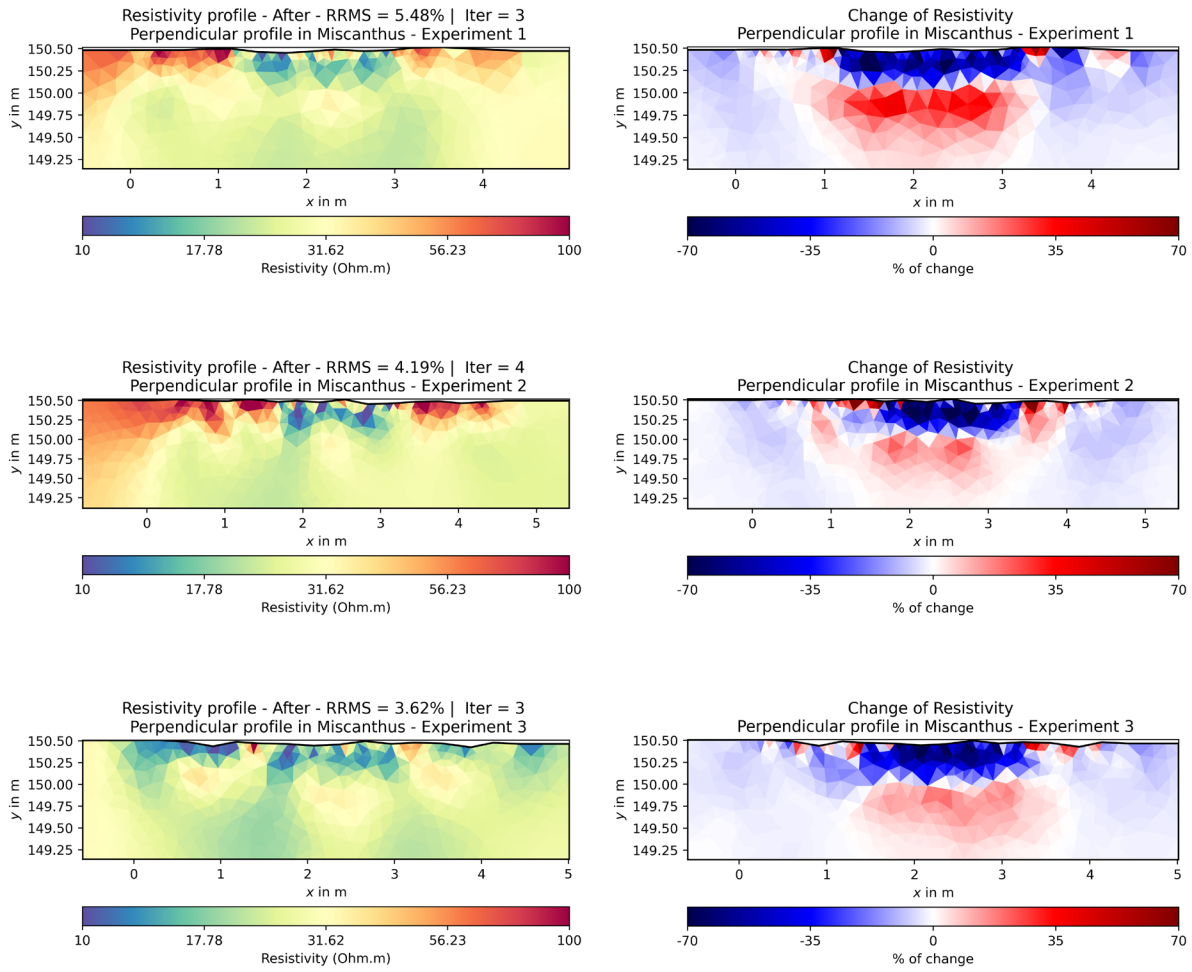

Figure 3-19: After-Infiltration resistivity profiles (Left) and change of resistivity compared to the Background (Right) of the perpendicular profile in miscanthus for each experiment

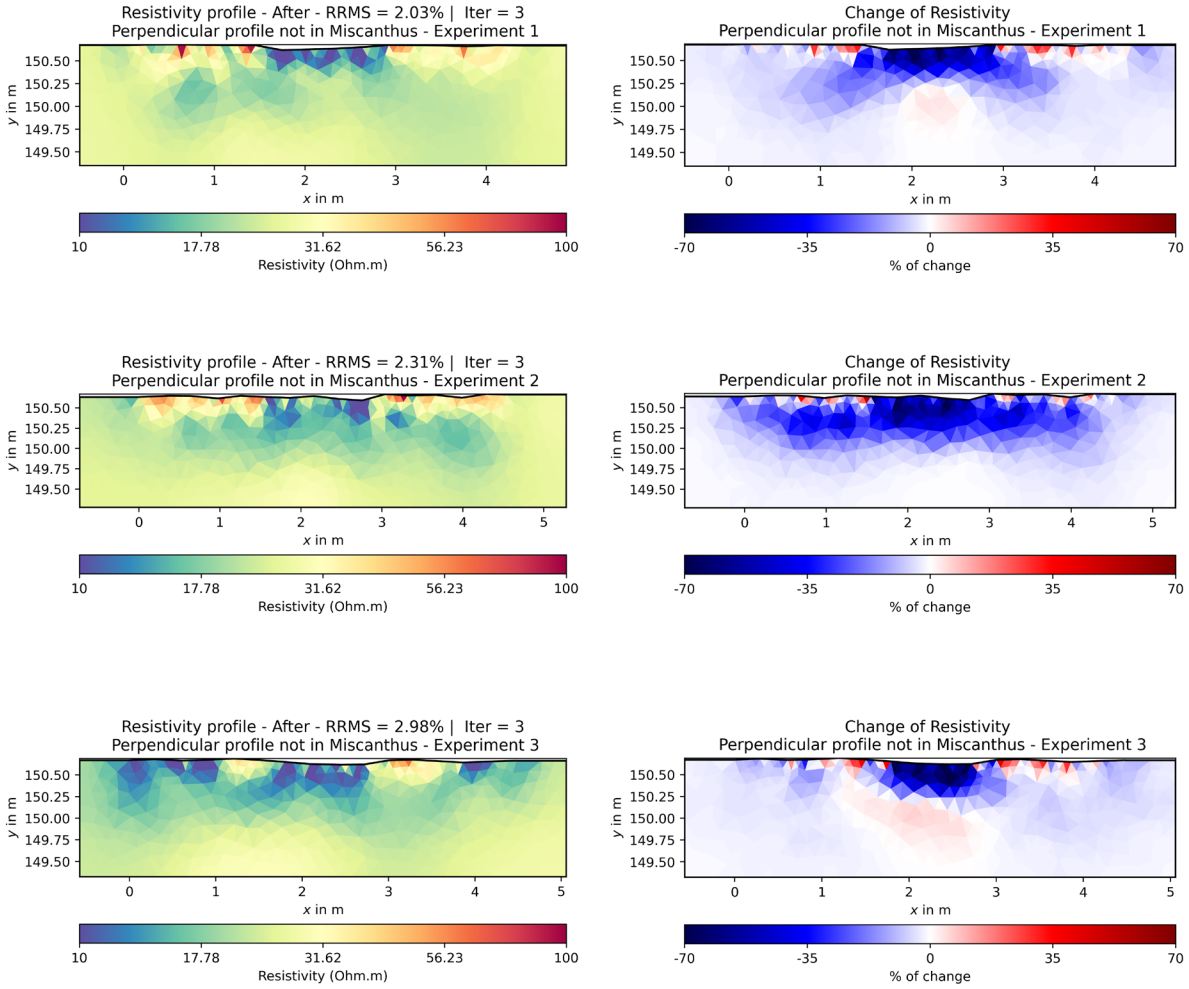

Figure 3-20: After-Infiltration resistivity profiles (Left) and change of resistivity compared to the Background (Right) of the perpendicular profile out of the miscanthus for each experiment

When proceeding to timelapse processing it is important to also analyse the sensitivity of the images, to be sure that what is represented in the inversion results is representative. Cells with a too low sensitivity do not accurately represent the reality of the model. The main issue that could occur is that there is an important change in sensitivity between background and after measurement data, the comparison between both timesteps can be misinterpreted because the resolution is not the same.

Figure 3-21 shows the coverage for all the three profiles of experiment 1 (the other coverage are available in Annexe 3 and Annexe 4). What can be retrieved from these images is that background and after measurements are sensitive for about the same extension and the same depth. From these images, it can be seen that all the main observations of resistivity decrease, and artifacts of resistivity increase are all in the sensitive areas. An additional piece of information is from the profile in Miscanthus, the extreme right part of the profile is not sensitive, therefore, resistivity values in this area must be interpreted with caution, fortunately, no phenomena of interest is appearing in this area, only the interpretation of the initial conditions is biased, as it appeared homogeneous while some heterogeneity is likely present, as in the rest of the profile.

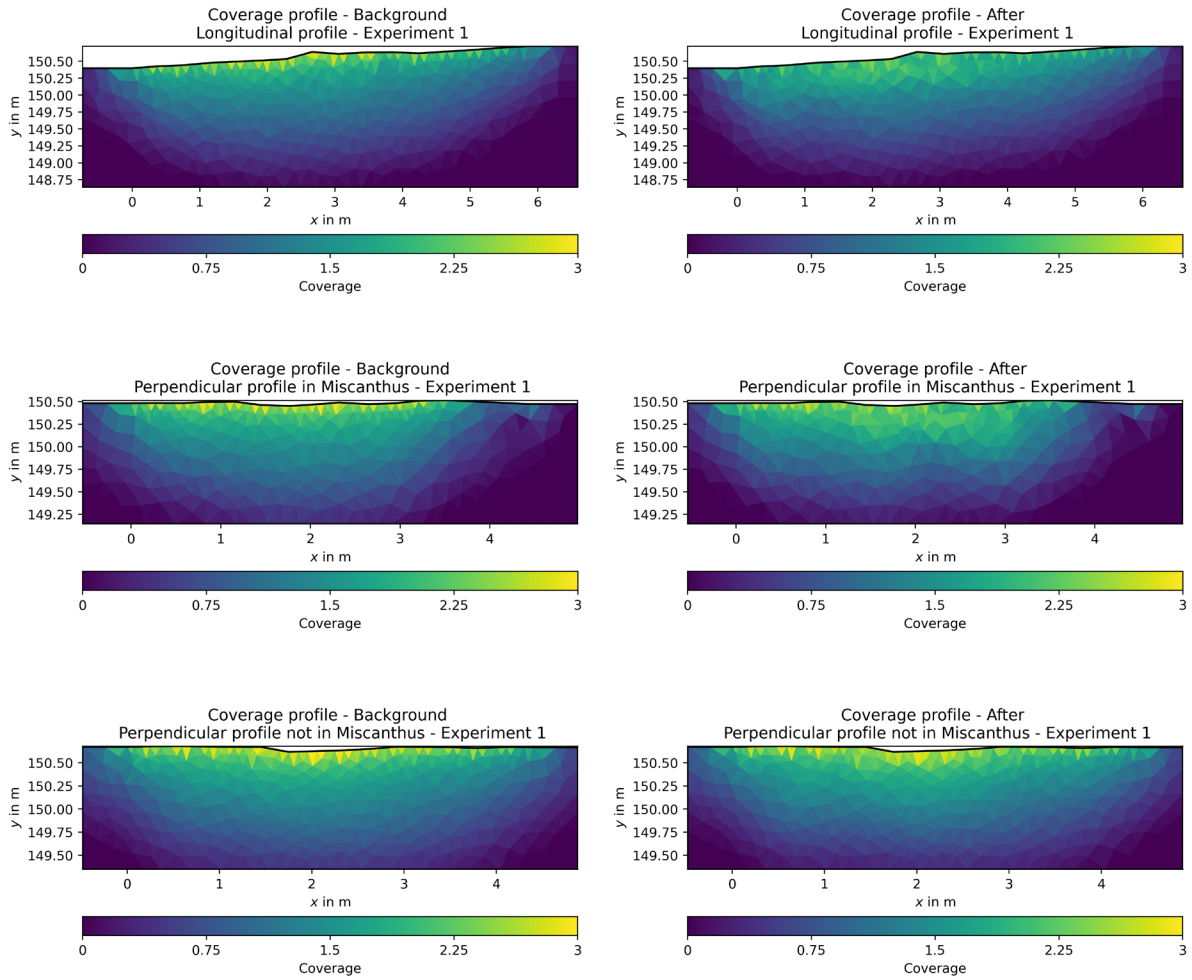

Figure 3-21: Coverage profiles of background (Left) and after-Infiltration (Right) of each profile for experiment 1

3.8. *Time-constrained Processing*

The results shown in the previous section represented the infiltration pattern by a decreasing resistivity zone as expected. However, lots of artifacts were generated when using an inversion processing with starting and reference model as the background. Before going into the interpretation of the different results, images with the fewest possible artifacts are processed using a full inversion algorithm with time constraints described in the Inversion theory section (Section 2.3). This algorithm has been proven to reduce artifacts for temporal processing (Kim et al., 2009 & Karaoulis et al., 2013) but also multi-frame processing based on frequency for IP data (Günther & Marting, 2016).

Firstly, the before and after measurements are processed and compared to the standard inversion to assess their representativity and accuracy. Once validated, the profiles can be interpreted before processing all timelapse frames during infiltration and addressing the related issues.

3.8.1. Before and After

Figure 3-24 to Figure 3-30 show the before and after results with full inversion of the longitudinal profiles. Many observations can be made from these images. While artifact generation has been significantly reduced by the application of the time-constrained inversion processing, it is particularly visible on the change of resistivity profiles, where only a slight increase in resistivities is observed beneath the zone of decrease. In terms of magnitude these artifacts are significantly lower than what was observed in the standard processing. Some surface artifacts showing increased resistivity have also been removed but some invariant cells are still present. As with the standard processing, decreasing the regularisation factor (λ) tends to increase artifact generation, this is why the same value of the regularisation parameter was used for both processing scheme, because trial and error revealed that this value is the first that decrease significantly and even almost all artifacts ($\lambda = 100$).

While reducing artifact generations, another issue that has arisen is the over-smoothing of the resistivity profiles by using the time-constrained scheme and a high regularisation factor. Smoothing between each frame is introduce due to the full inversion. The result: a complete change of the representation of the resistivity profiles, especially with the background. As a result, the error and misfit of the results have increased as RRMS of profiles demonstrate. The number of iterations is now the same for all profiles, as they are inverted simultaneously.

The question that occurs before interpreting the profiles is to know if the result of the full inversion despite the greater error, is representing the dynamic of the system. To prove that phenomena are still represented, the computed data is compared to the measured data. A comparison with the results of these graphs using the standard inversion is also performed.

Figure 3-22 represents the different comparisons between computed and real apparent resistivities for the longitudinal profile of the second experiment. Firstly, when analysing the

background, the standard inversion of the background revealed a particularly good fitting of the points on the identity line as the low RRMS suggested, confirming the accurate representation of the background as it was analysed in the initial conditions results. Concerning the full inversion result of the background, as shown in the following figure, the high resistivities are often miscalculated and underestimated, this is also what is visible in the inversion result of the Figure 3-24, Figure 3-25 and Figure 3-26 where the top highly resistive layer is less well represented compared to the standard inversion. Nonetheless, apparent resistivities below 35-40 Ω.m are close to the identity line.

Secondly, the after result with full inversion shows lower error compared to the background, misfits of the points are still present, and the effect of smoothing can be observed in the trend of the scatter plot that presents a smaller slope than the identity line, showing that lower resistivities are overestimated and high resistivities underestimated.

Finally, the final plots showing the ratio of the previous ones are important because they determine if the generated models represent well the phenomena. Meaning that if a change of resistivity is occurring in the real data, this change must be represented the same way in the generated models, the ratio enables representation of this change. As expected from the good results of the single inversion, for the standard processing the ratio fits the identity line satisfactorily. For the full inversion, the result is encouraging, while smoothing is clearly visible when observing the general trend of scatter plot, a trend line would also have a smaller slope than the identity line, but the trend is clearly visible, meaning that phenomena are represented but smoothed. From an interpretation point of view, this conclusion means that the pattern of infiltration can be interpreted with the full inversion result but mostly qualitatively, the quantitative interpretation becomes uncertain because of the smoothing that induces underestimation of the real relative change between background and after-experiment results.

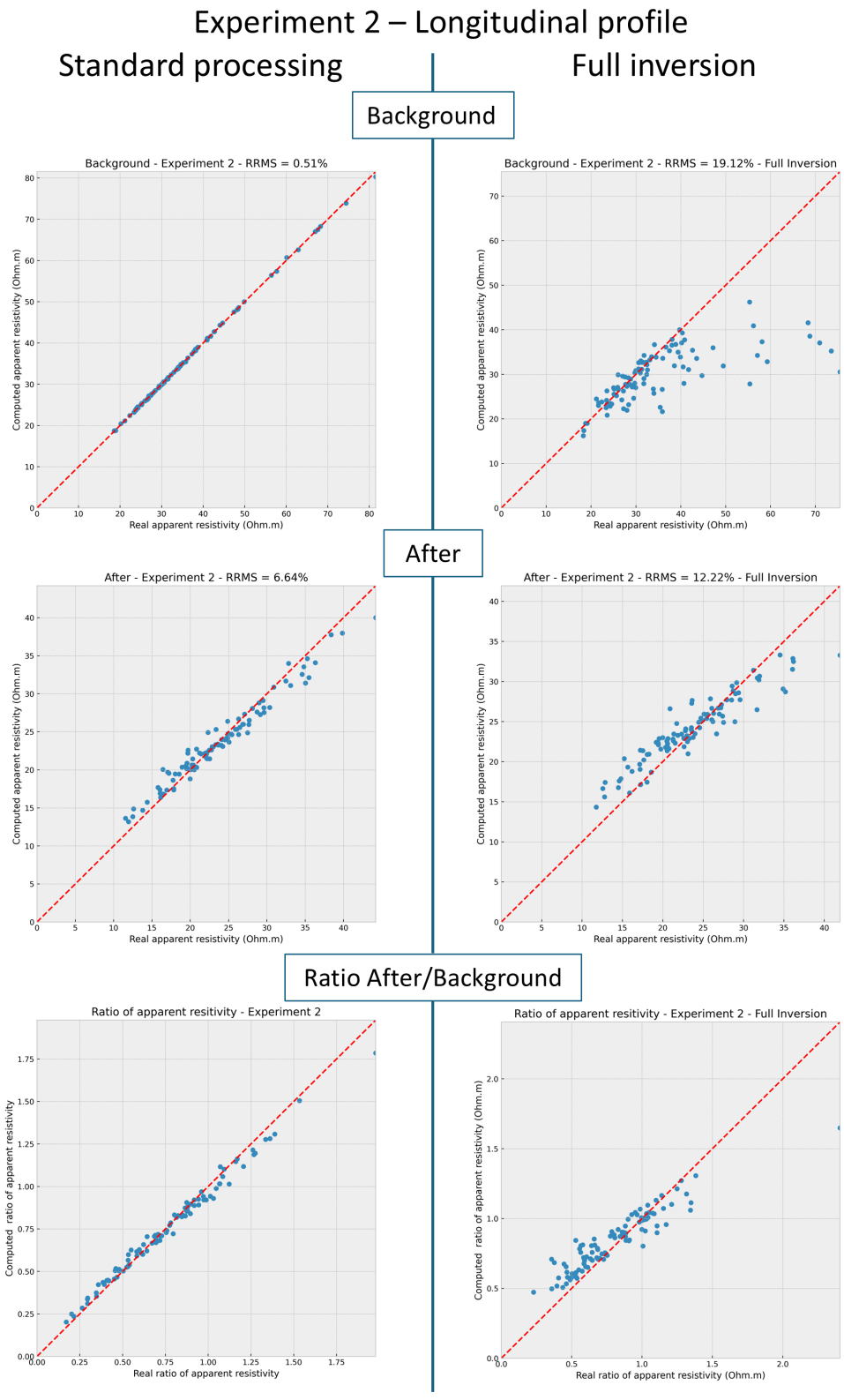

Figure 3-22: Comparison of the real and simulated data for standard and time-Constrained processing for the longitudinal profile of the experiment 2

For better clarity, only one comparison of computed and real resistivities data is shown in this section. Nevertheless, all plots have been generated for all profiles of all experiments and for both inversion schemes. Generally, the conclusions are the same as the discussion just made and all plots of comparisons are available in Annexe 5 to Annexe 13. In the Figure 3-23, slight changes appear when computing the perpendicular profiles, probably because of the smaller amount of change between frames because infiltration occurs only in the middle of the profile and not all along it like the longitudinal one. For the profile not in the miscanthus, the trend is almost parallel to the identity line, it seems that the points are just translated perpendicularly to the identity line, and for the profile in the miscanthus the overall look of the scatter plot is similar to the longitudinal profile. From the Annexe 5 to Annexe 13, it is shown that the perpendicular profiles, especially the one not in the miscanthus, have better fit between computed versus real apparent resistivities resulting also in smaller RRMS values.

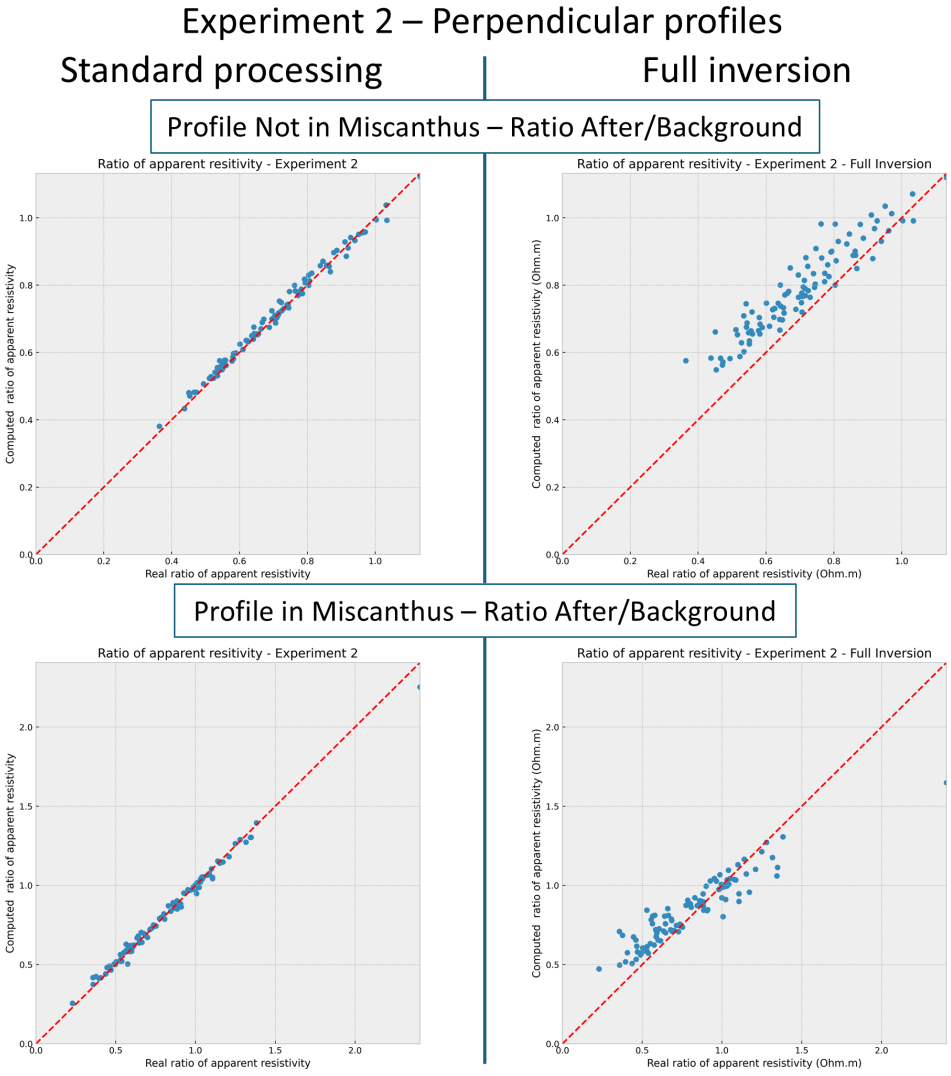

Figure 3-23: Comparison of the ratio of resistivity (After/Background) for the standard and time-constrained processing of both perpendicular profiles of the experiment 2

Now that the infiltration is known to be represented by the full inversion, time-constrained processing with artifacts removal, the different results of the before and after comparison can be interpreted.

First of all, the longitudinal profiles are studied in Figure 3-24, Figure 3-25, and Figure 3-26. The smoothing of resistivity profiles is clearly visible on the following figures in comparison to the initial conditions results. Indeed, the top layer of higher resistivity is no longer represented on the background profiles.

Secondly, infiltration patterns can be interpreted as the decrease in resistivity zones, these decreases are mostly concentrated in the first top 50 cm of soil. Infiltration patterns are similar for all experiments, what can be observed is that where water starts to flow on the right of the profiles (from X = 6 to X = 5 m), resistivity decrease is very low or even almost non-existent while the magnitude of the decrease augments as the X position decreases until reaching the miscanthus zone (X < 3 m) where the resistivity decrease is significantly greater, especially from X = 2 to 3 m. It is also important to note that this area of higher decrease correlates with the area of higher starting resistivities on the background profiles. Because of the longer duration of infiltration of the second and third experiment (3h vs 2h for experiment 1), it is expected to have greater infiltration, but no significant differences between profiles have been spotted. The first interpretation on these profiles is that an overall infiltration front is detected at approximately 40-50 cm depth with a greater decrease in resistivity at the beginning of the miscanthus part in the direction of the water flow.

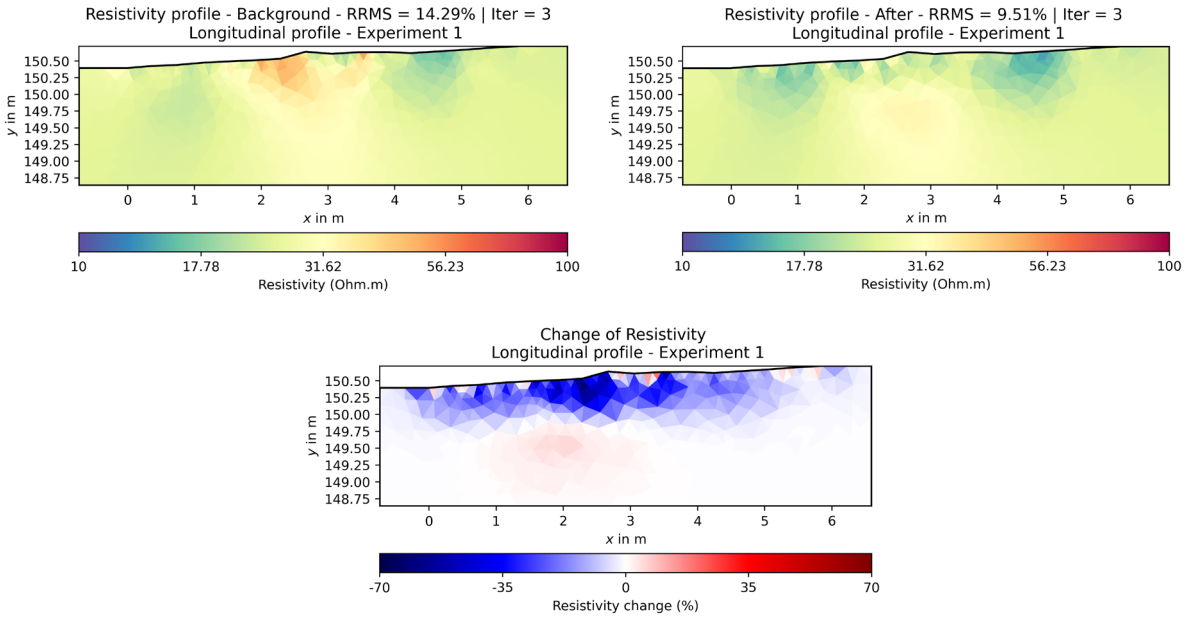

Figure 3-24: Time-constrained processing resistivity profiles results for Background (Top Left), After infiltration (Top Right) and change between (Bottom) for the longitudinal profile of experiment 1

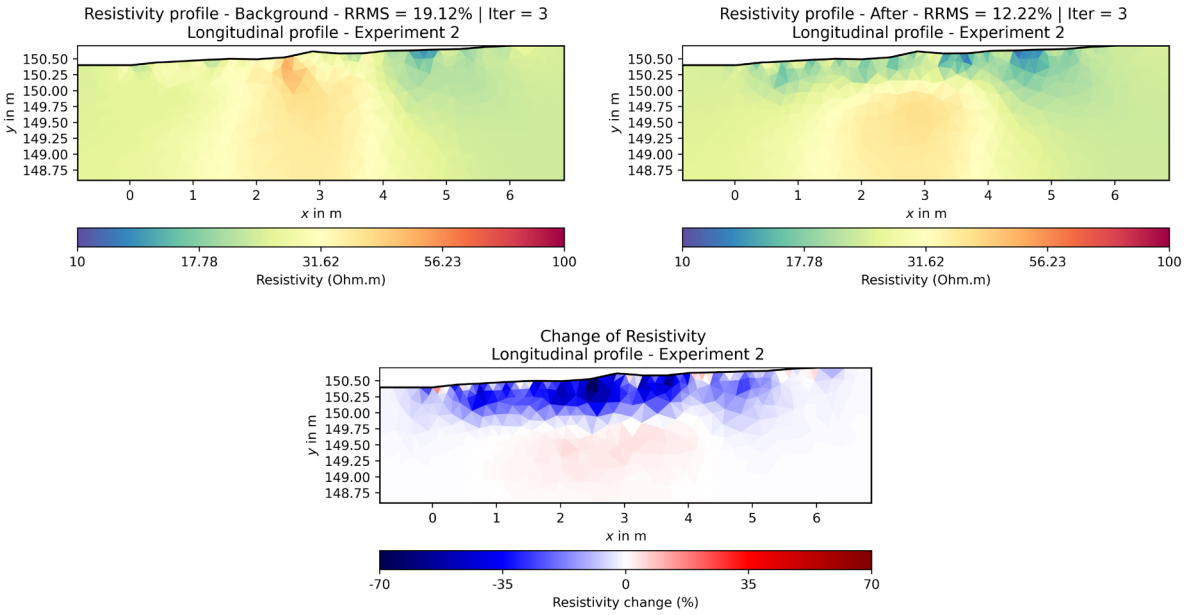

Figure 3-25: Time-constrained processing resistivity profiles results for Background (Top Left), After infiltration (Top Right) and change between (Bottom) for the longitudinal profile of experiment 2

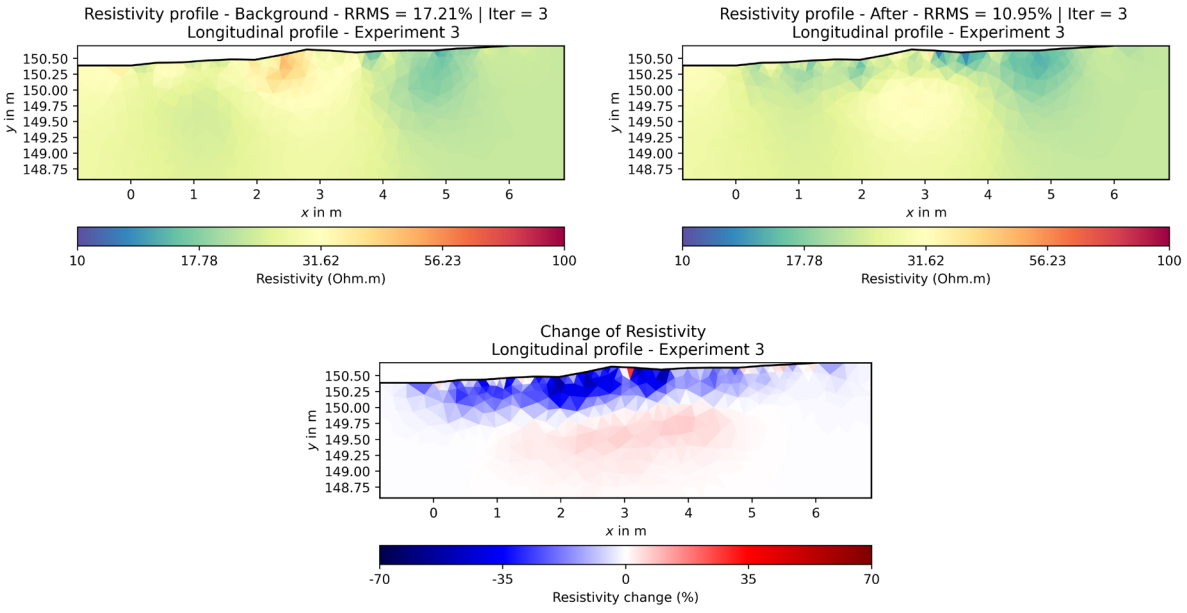

Figure 3-26: Time-constrained processing resistivity profiles results for Background (Top Left), After infiltration (Top Right) and change between (Bottom) for the longitudinal profile of experiment 3

Based on the different profiles, plots of the Figure 3-27 are generated. They are calculated using intervals of 15 cm of depth on the profile and retrieving the mean resistivity (weighted by the cell areas) for these intervals for a 2 m-wide zone in the middle of each of the two parts (with or without miscanthus). Then, the mean resistivity decrease is calculated for every depth interval and part of the profile.

From these representations, the same conclusion as the profile analysis can be retrieved, as the miscanthus half possess a greater resistivity decrease while the overall depth where no more decrease is observed seems to be equal in both zones and close between all experiments. Nevertheless, for a given percentage threshold, for example, 10%, this decrease is reached deeper in the miscanthus zone, this also correlates with the fact that the overall decrease in resistivities is greater in the miscanthus. Standard deviations at each depth can be high, which can express an overall heterogeneity in the decrease in resistivity within the same part of the profile.

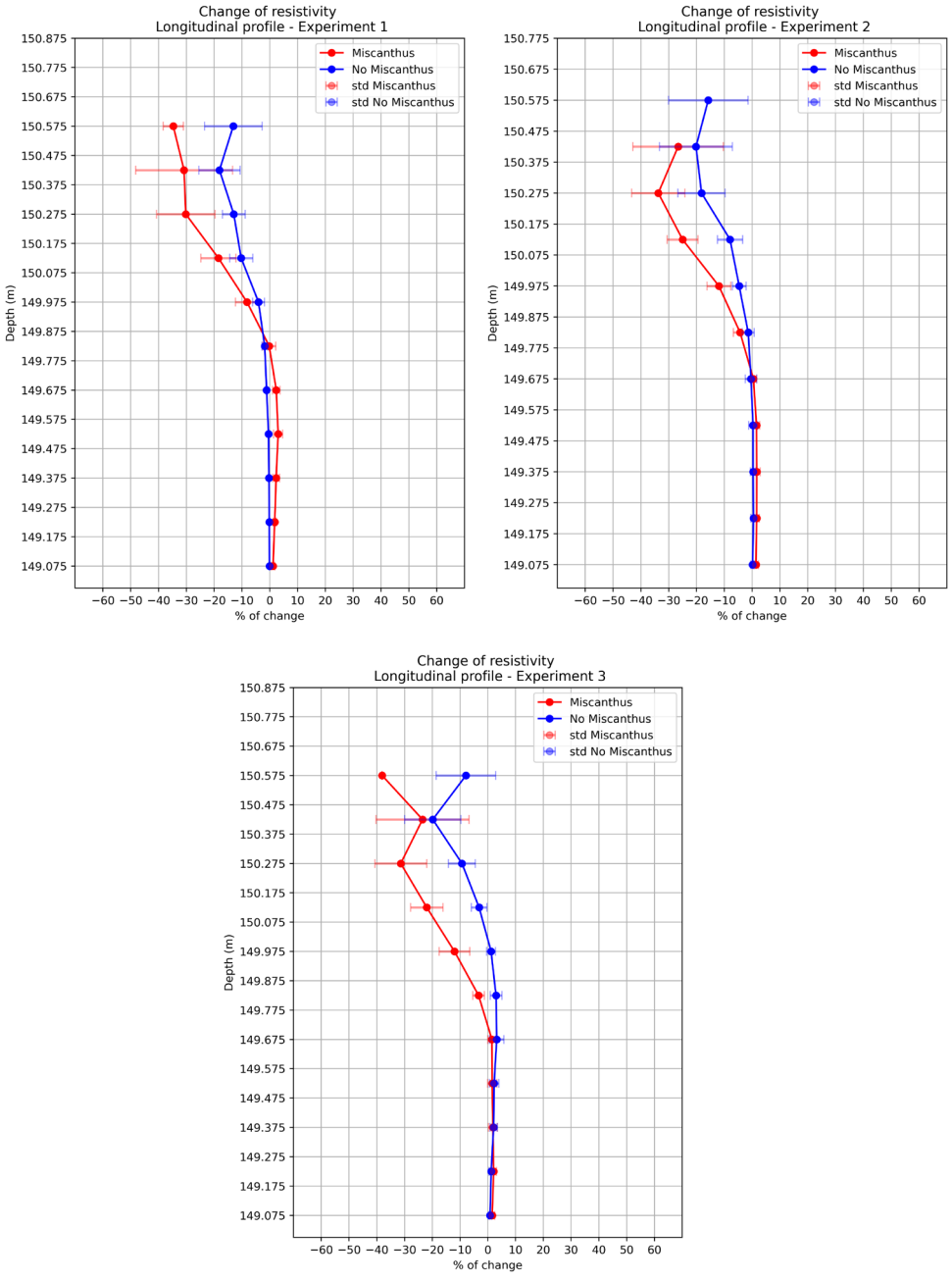

Figure 3-27: Vertical variation of resistivity in and out of the miscanthus for the longitudinal profile of each experiment

Perpendicular profiles are processed the same way in the next Figures (Figure 3-28, Figure 3-29, Figure 3-30) for each experiment. Generally, RRMS values are lower than those observed in the longitudinal profiles like already discussed in the computed vs real data. Here it can be seen that the top more resistive layer is better represented on the edge of the infiltration band, thanks to the fact that only minor changes appear in these zones so that the overall temporal smoothing has less effect. Artifacts of resistivity increase are still present in some top cells next to the infiltration but no longer beneath it.

Concerning the interpretation of the infiltration, the overall infiltration front seems to be similar to the solution of the longitudinal profile with approximately 40-50 cm in total of infiltration. It can be seen also that the horizontal extent at the surface is larger than the infiltration band width (1 m). This can be explained by the fact that the junctions between plastic boards were not impervious but also by lateral flows of water. During the experiment, wet soils were observed out of the infiltration band next to the plastic boards, it is therefore concluded that this horizontal extension at the surface is real. Differences between profiles in or out of the miscanthus are present and are reviewed for each experiment.

For the first experiment (Figure 3-28). While the resistivity decrease area in the miscanthus seems smaller and have a lesser vertical extension, this observation needs to be criticized. Indeed, the bare soil half of the miscanthus decrease in resistivity reaches a deeper extension vertically and horizontally but this is mainly a low decrease in resistivity that occurs at greater depths and more laterally, it can then be misinterpreted as water infiltration. Due to the high conductivity of the infiltrated water, the right interpretation will be that the saturated zone is limited to areas of higher resistivity decrease. In this case on the profile not in the miscanthus: x = 1.5 m to 3 m and to a depth up to 150.35 m at maximum. This interpretation is supported by the after-infiltration resistivity profile that clearly highlights this area as low resistivity. The extent of this area can be explained by the inversion smoothing or artifacts of resistivity decrease. Also, in the profile within miscanthus some similar low decreases in resistivity on both sides of the profiles are present.

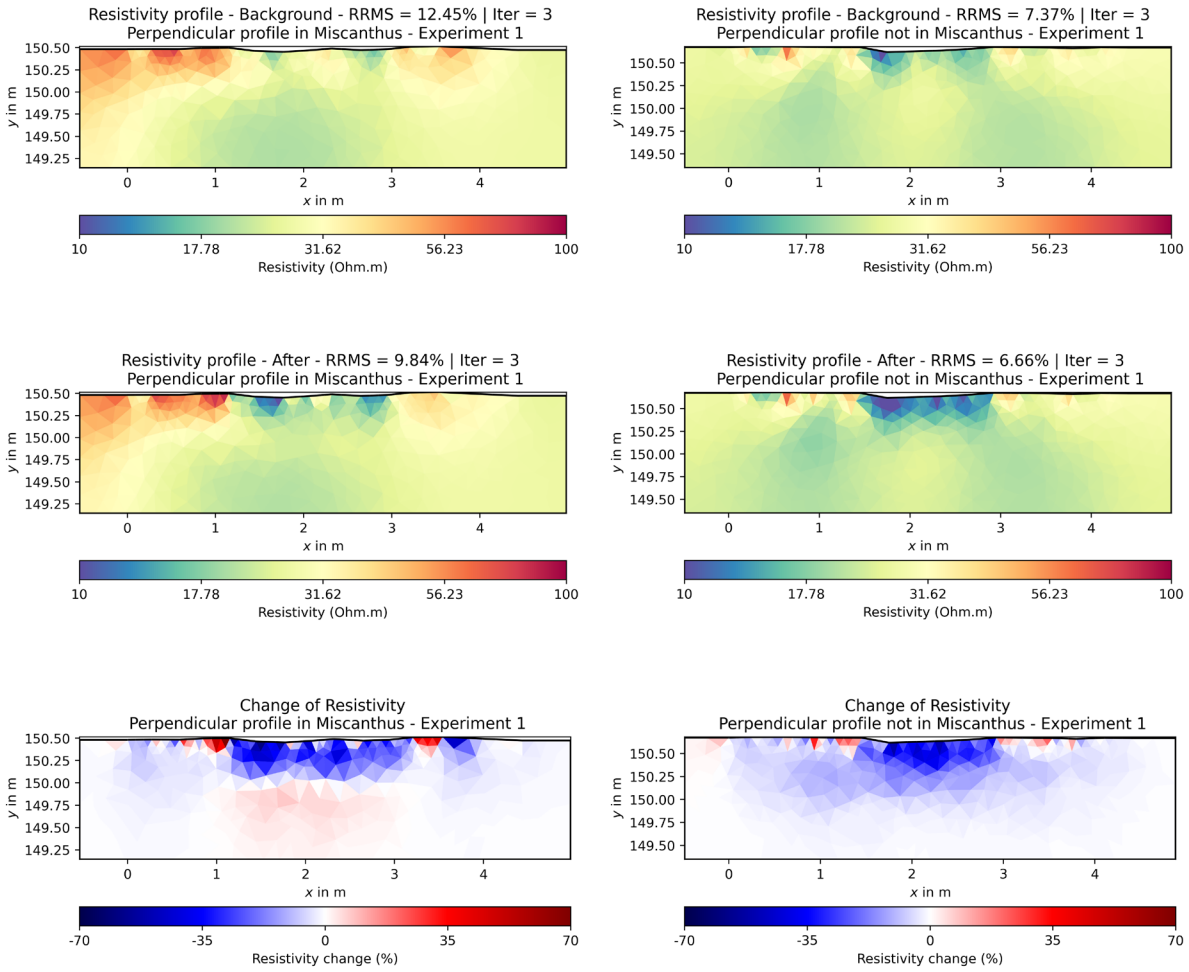

Figure 3-28: Time-constrained processing resistivity profiles results for Background (Top), After infiltration (Middle) and change between (Bottom) for the perpendicular profiles in (Left) and out (Right) of the miscanthus of experiment 1

Secondly, for the experiment 2 (Figure 3-29), similar patterns are present for the profile in the miscanthus, and also a larger zone of resistivity decrease in the bare soil profile. This time, the larger zone of decrease shows a higher magnitude than in the first experiment, particularly horizontally, it is then possible that lateral flows of water were more present in this part compared to the miscanthus half. This is not an effect of the temporal-constrained scheme because a similar pattern had already been observed in the standard processing solution (Figure 3-20).

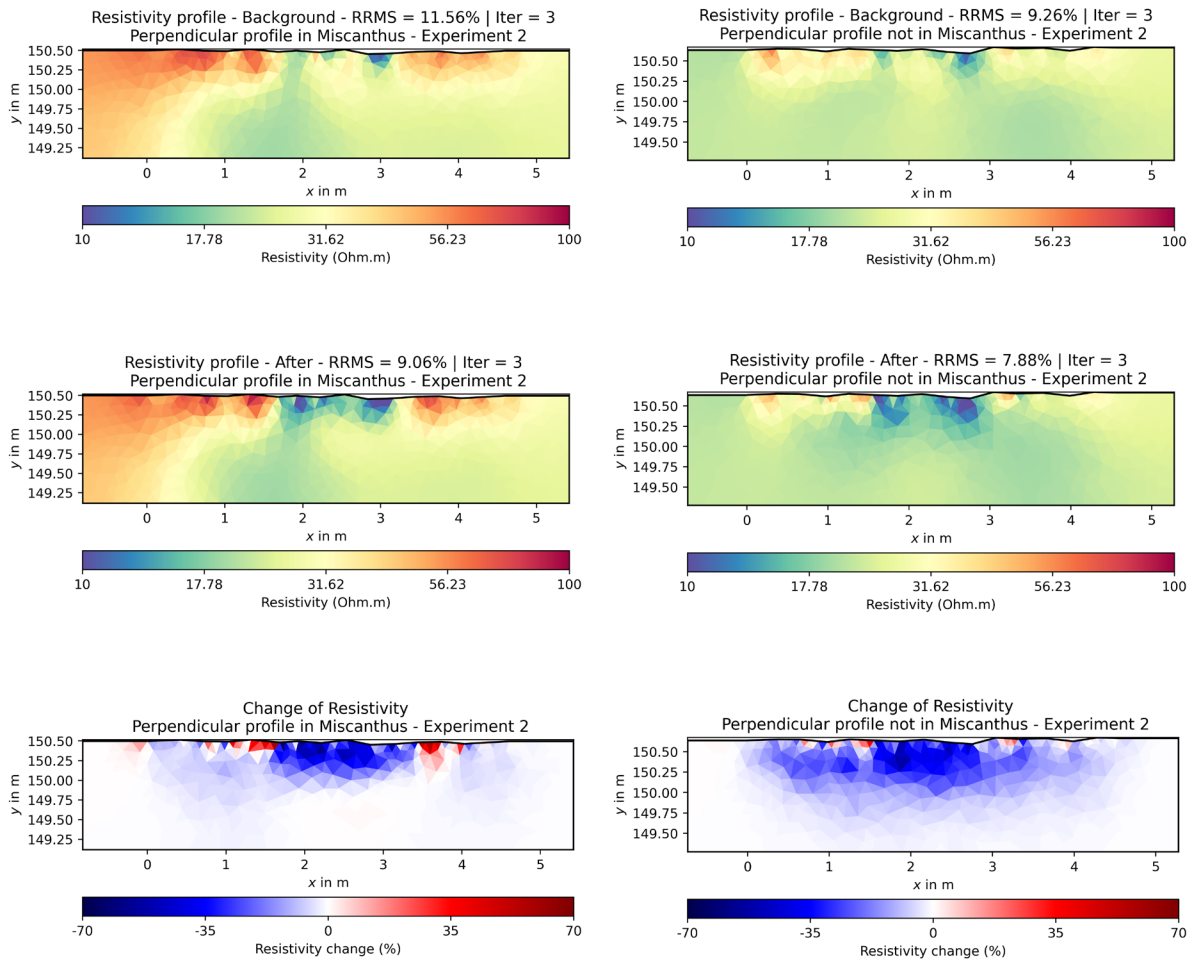

Figure 3-29: Time-constrained processing resistivity profiles results for Background (Top), After infiltration (Middle) and change between (Bottom) for the perpendicular profiles in (Left) and out (Right) of the miscanthus of experiment 2

Finally, for the last experiment (Figure 3-30), again, same pattern of infiltration is retrieved from the change of resistivity profile in the miscanthus. In this case, less lateral extension of the resistivity decrease zone for the profile outside the miscanthus, it is even seen here that the lateral extension at the surface is close to 1 m, so no leaks, or at least fewer leaks, were present through the plastic boards. Moreover, the vertical extension is similar to previous experiments.

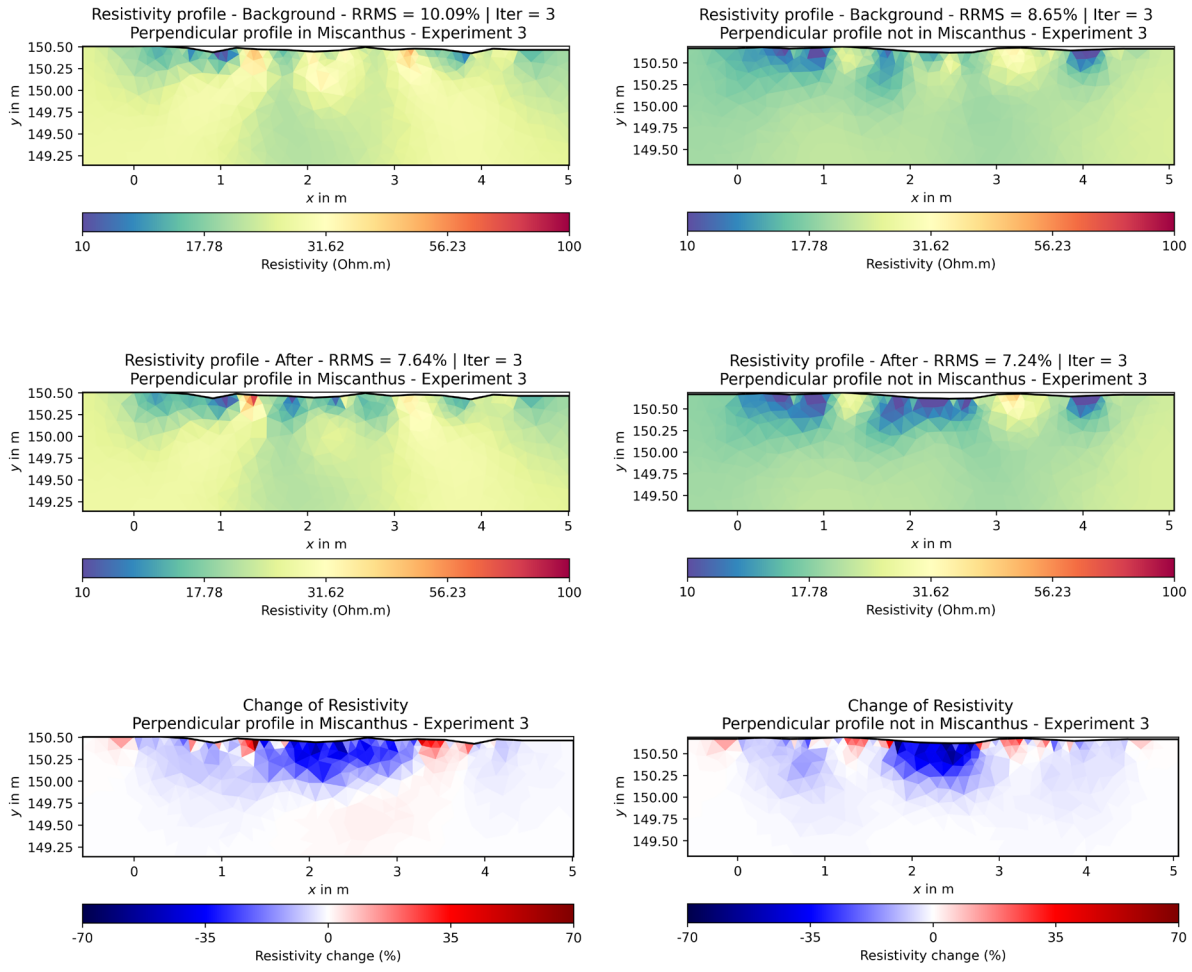

Figure 3-30: Time-constrained processing resistivity profiles results for Background (Top), After infiltration (Middle) and change between (Bottom) for the perpendicular profiles in (Left) and out (Right) of the miscanthus of experiment 3

Before and after analysis of the different profiles with the time-constrained processing revealed an overall final infiltration pattern. The generated images were free of major artifacts of increase resistivity. It has been proven that these results can reflect the relative change between the different images, nevertheless, quantitative assessment of the images is not possible due to the smoothing effect that impacts the resolution. To conclude, areas of high decrease in resistivities seem coherent to determine an approximation of the infiltration pattern. Some areas with lower decrease needs to

be analysed with caution because they could represent an effect of the processing scheme (on the sides of the perpendicular profiles) or simply be an overestimation of the real infiltration, as seen in the simulated experiment.

Vertical mean resistivity changes for different depths graphs interval are available in the Annexe 14 for the perpendicular profiles and generally the magnitude of the decrease is similar between each profile.

3.8.2. Timelapse Analysis

The final infiltration pattern has been discussed in the previous sections, but this analysis only considers the initial and final results of the infiltration test where the water sheet flow is not present, with this kind of experiment, it is interesting to study the dynamics of the infiltration. The apparent resistivity study already highlighted an overall greater decrease at the start of the experiment that tends to stabilize for the miscanthus half. The objective is to study the high number of measurements that have been collected on the longitudinal profile during the experiment by the interpretation of the inversion results with the time-constrained processing described previously.

The major challenge when processing this data was the establishment of the water sheet flow. Its effect has been discussed in the simulated experiment, as a reminder: the top parts of profiles are misinterpreted by the effect of the water sheet flow because lower resistivities are calculated for this region. However, despite the misinterpretation of the real resistivity of the medium, the relative change between two images is still represented, but the infiltration simulation revealed an overestimation of the infiltration front that can also be partially due to the method used to simulate the electrodes.

First, the data processing was performed using the full inversion algorithm directly with all the timesteps together, but this method revealed an overall over-smoothing of all the images with high errors and no coherent evolution of the infiltration (overestimation at the start and even the whole profile showed a decrease in resistivity at the end) because of the temporal constraints applied between all frames. This technique is then omitted for processing all timesteps at once. The technique chosen was then to simply process for every timesteps with the time-constrained processing of the background and the chosen timestep, with a regularisation factor (λ) equal to 100 like the previous processing. In this way every frame is temporally regularized by the background only, the drawbacks are that the background is at every step recalculated with the influence of the chosen step because the smoothing effect is coded to have an effect between each frame and not only the background having an effect on the step. Nevertheless, because it is known that the resistivity is already miscalculated due to the influence of the water sheet flow and the smoothing of the processing, the real point of interest is the relative change between frames which is calculated for every timestep.

The last issue that was encountered with the processing of all the timelapse frames is the background. The background used previously did not include the water sheet flow because the measurements were acquired before the start of the infiltration test. The consequences are that once

the water sheet flow is established, despite all the smoothing effects, artifacts of increased resistivities appeared again, probably because of the important contrast that the water sheet flow creates. To avoid this problem, it has been chosen to select the background as the first measurement that were taken when the water sheet flow was established, in that way the relative change can still be studied with no effect of resistivity increase below the infiltration front. However, the bias of increased resistivities below due to artifacts and lower resistivity on top because of the water sheet flow and the temporal constraint is still present on the resistivity profile, which is why mainly the relative change will be studied in this section (Figure 3-31).

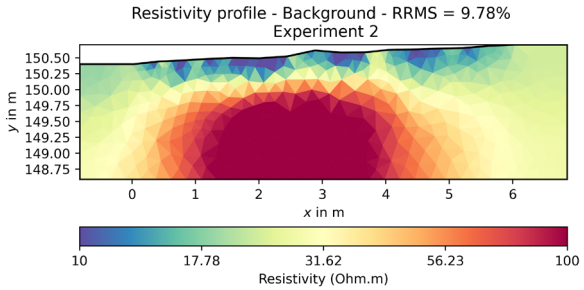

Figure 3-31: Background inversion result with the water sheet flow for time-Constrained processing of the last frame for the longitudinal profile of the experiment 2

It is important to mention that there are also 2 hours of measurements after the infiltration, but these data did not reveal important variations, probably because the range of time was too small to observe any drying phenomena.

Due to the limitation of the format of this work, the results for every frame cannot be displayed, it has then been chosen to show a few timesteps of results, depending on the experiment, showing the major points of interest. Again, as a reminder, about the following images, the miscanthus parcel is always from X = 0 to 3 m and the bare soil part from 3 to 6 m, with the water flowing from right to left.

To begin with, the first experiment had an infiltration time shorter than the two others, the last frame is then at 114.39 min, the time displayed is always the time after the background image, i.e., the time after the establishment of the water sheet flow. Before analysing the different images of resistivity decrease at different timesteps (Figure 3-32), it is important to observe that all frames have a similar error, indeed, the RRMS is close to 10% for every frame.

Now, when analysing the different frames, it can be seen that the dynamics of the infiltration is more important at the start of the infiltration test. For the first 3 frames shown, it is seen the resistivity decrease is firstly seen in the miscanthus part, especially at the start and the end of this band (x = 0 m and 3 m). Later in the test, the resistivity starts decreasing also in the bare soil part but at a smaller magnitude as was previously observed in the before and after study. Between the last three frames, it is seen that only slight changes are appearing with an increase in the magnitude of the relative change, but no significant pattern evolution. This suggests that the dynamics of the

infiltration is more important at the start of infiltration. Logically, because the soil is at the beginning unsaturated, the infiltration will be greater, but once the top part becomes saturated, the rate of infiltration becomes smaller. The last point that can be retrieved from the analysis of the timelapse of the first experiment is the similarity between the last frame and the after-infiltration image previously discussed. This shows that the same result is observed despite all the constraints that the water sheet flow imposes.

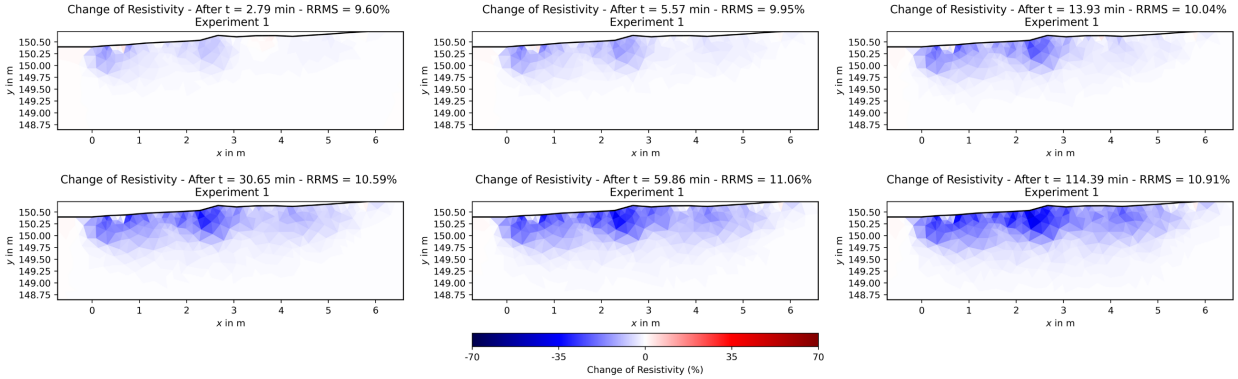

Figure 3-32: Change of resistivity of timelapse frames of the longitudinal profile for the experiment 1

The second experiment's infiltration time lasted longer, so the last frame with the water sheet flow is the one 166.9 minutes after its establishment. Like the first experiment, the dynamics of the infiltration seems quicker at the start of the experiment as the first 3 timesteps displayed suggest (Figure 3-33). On the contrary of the first experiment, the fastest decrease in the miscanthus part seems less important in this experiment and similar changes appear in the bare soil half especially between 3 and 4 m, but this could still be due to the effect of miscanthus. Generally, the infiltration seems more homogeneous for this experiment across the overall profile and especially in the miscanthus zone, because for the first experiment, the two zones at the start and the end of the miscanthus half seemed to have a greater decrease possibly indicating some preferential infiltration zones. Again, for the 3 later frames in the infiltration phase, the change between them is less important, despite the large time gaps between the images, also suggesting a decrease in the kinetics of the infiltration with time. The overall infiltration, as previously seen in the simulated experiment, is overestimated by the decreased resistivity zone, but it is coherent to consider the highest resistivity zone of the final frame as the infiltration as it also correlates with the before and after analysis of the same profile.

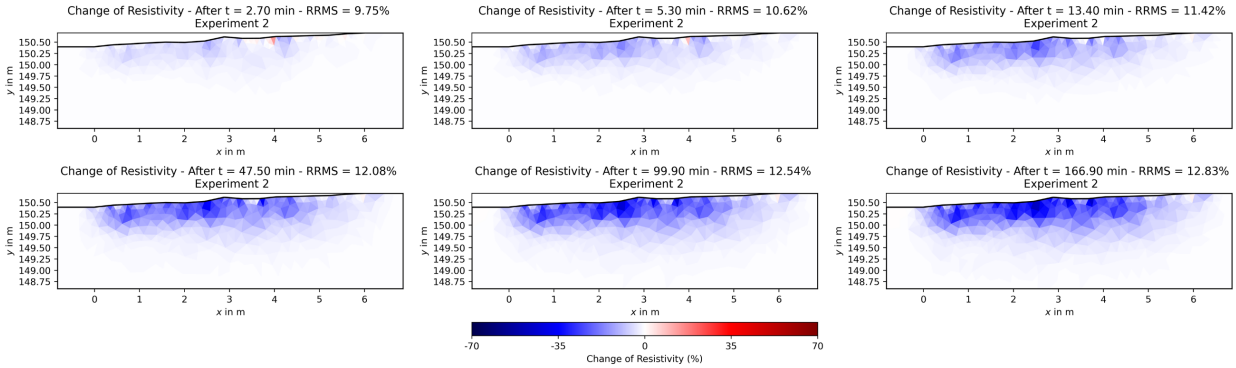

Figure 3-33: Change of resistivity of timelapse frames of the longitudinal profile for the experiment 2

Finally, the last experiment presents a mix of the observations from the first two (Figure 3-34). The variability of the kinetics of the infiltration is also visible. Additionally, preferential zones of infiltration are present in the miscanthus part at the very start of the experiment, but not as clearly as in the first experiment. The overall infiltration pattern stays coherent with the previous timelapse results of other experiments, but also with the conclusion of the before and after analysis.

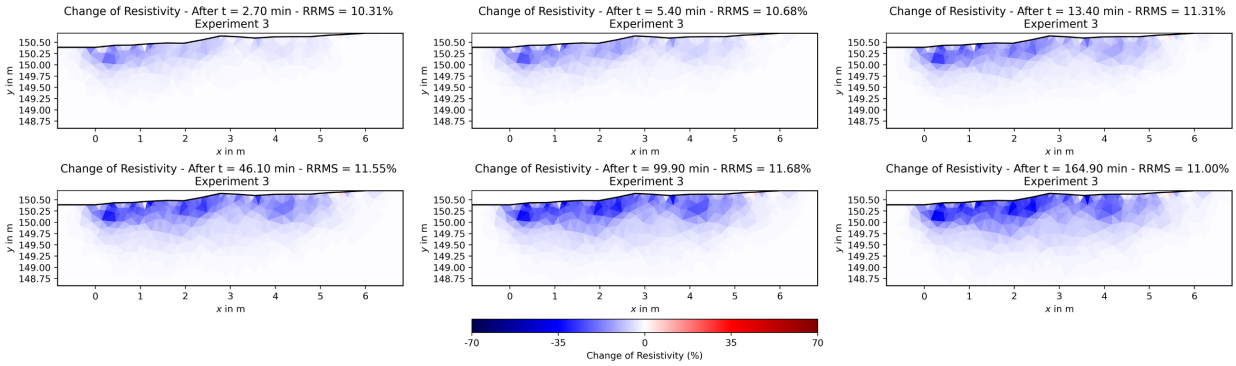

Figure 3-34: Change of resistivity of timelapse frames of the longitudinal profile for the experiment 3

Figure 3-35 shows side-by-side, close timesteps of every experiment and isolines of resistivity decrease of 10 and 20%. These images highlight the similarities that exist between the experiments in the infiltration pattern. The isolines also bring a better view and enable confirmation of previous observations about infiltration rates that decrease in the latest timesteps.

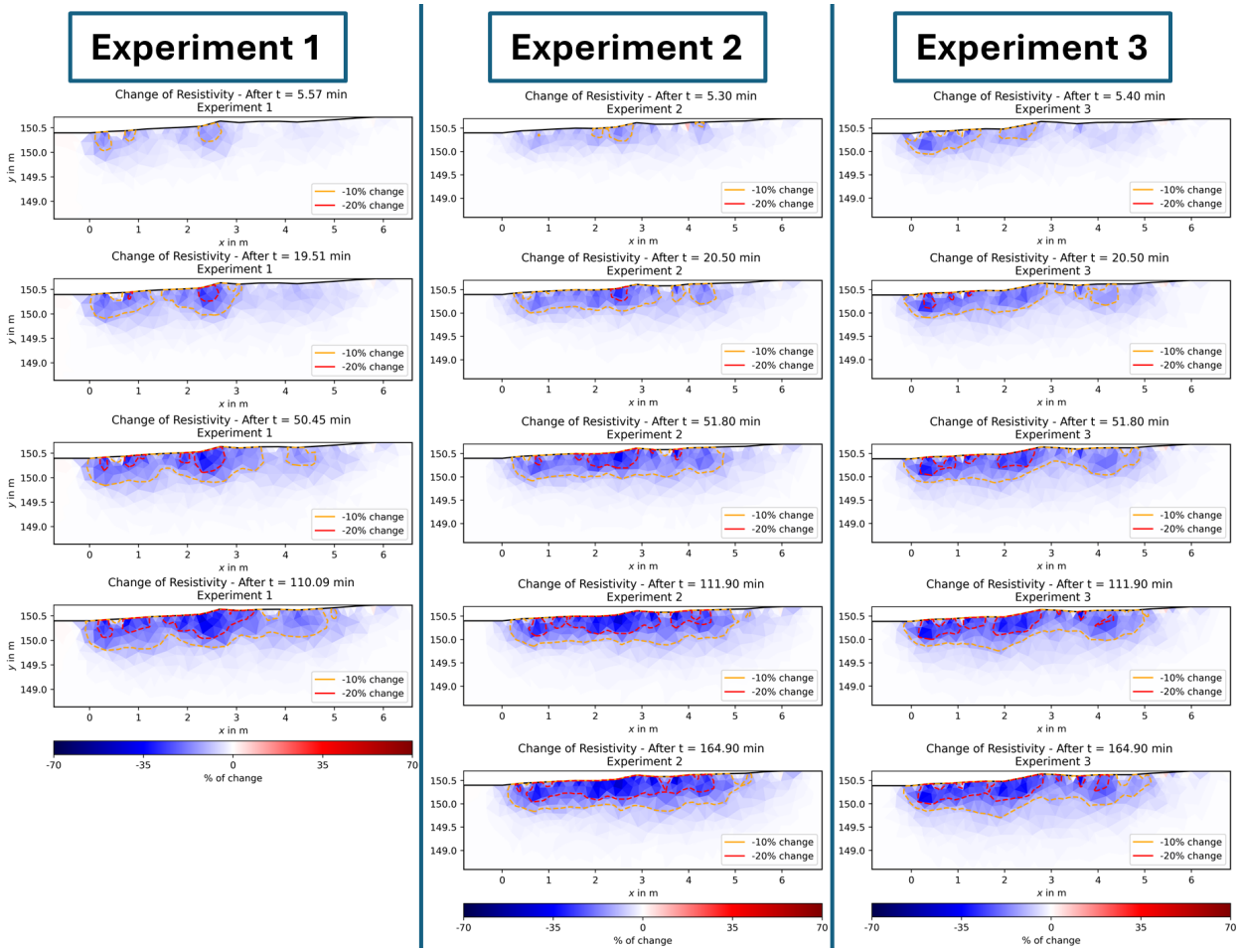

Figure 3-35: Change of resistivity and isolines of resistivity decrease of the longitudinal profiles for all experiments and similar timesteps

As previously shown also in the before after section, the mean resistivity by depth steps in the middle of each part of the profile can also be represented. As a reminder, these figures are plotted by using the mean resistivity in a 2 m large band in the middle of each half for each depth range of 0.15 m. Here only the results related to the last experiment are represented for the same timesteps as the previous Figure 3-34. All the plots for the first two experiments are available in Annexe 15 and Annexe 16.

These plots (Figure 3-36) confirm the previous observations with a greater decrease in the miscanthus half and at the start of the infiltration test. What is interesting is that directly after the start of infiltration, the depth where resistivity is decreasing is already high (about 0.6 m). This can

be due to several factors such as the influence of the water sheet flow that impacts the result by overestimating the depths of infiltration but also because of the limited resolution that is directly dependent on the electrode spacing (40 cm). In the first timesteps it is clearly visible that only the miscanthus half shows a significant relative change of resistivity, while the decrease in the other half appears later. As time passes, the more the change between frames becomes smaller as observed in the profile representations. Generally, the same observations are retrieved for the two previous experiments (Annexe 15 and Annexe 16).

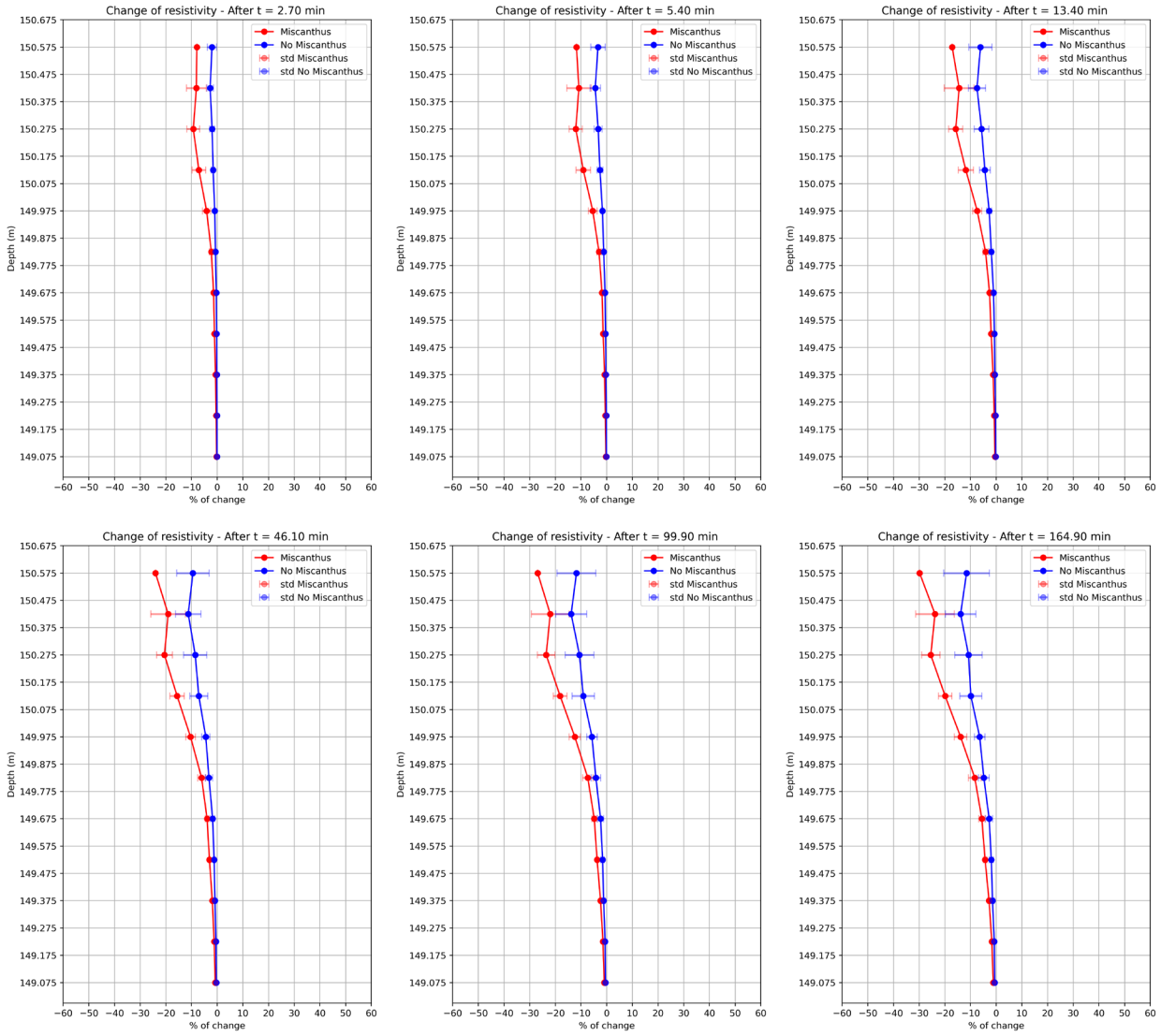

Figure 3-36: Timelapse vertical change of resistivity in or out of the miscanthus for the longitudinal profile of the experiment 3

To ensure that the different timesteps reproduce well a coherent and comparable model, the sensitivity can be retrieved by the coverage profiles of the timesteps, which reveal similar coverage between all frames, assuring the same representation of the model (Figure 3-37). If compared to the before and after coverage, it can be seen that these models are less sensitive to greater depths probably due to the influence of the water sheet flow, but the main observations of resistivity decrease are in the high coverage zone, confirming we partially represent the physical reality of the model. It is also interesting to highlight that there is no coverage difference between the miscanthus and the bare soil half. Other experiments' coverage profiles are available in Annexe 17 and Annexe 18.

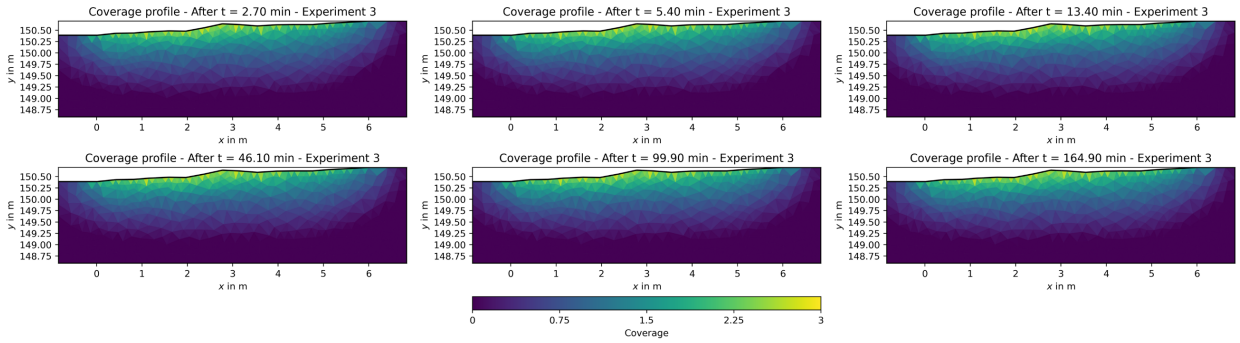

Figure 3-37: Coverage profiles of timelapse frames of the longitudinal profile for the experiment 3

Studying infiltration by analysing the profile images is sometimes difficult. Therefore, it has been decided to represent the evolution of resistivity and resistivity change with time by retrieving the resistivity value of every cell above a chosen depth, to construct a graph similar to the one of apparent resistivity evolution but with real resistivity calculated. To do that, all cells above 149.8 m are retrieved (depth chosen after analyses of the change and resistivity profiles, so that the high resistivity artifact is not taken into account and the overall infiltration front is included), these cells are then separated into 0–3 m and 3–6 m zones to separate the miscanthus and the bare soil part and the weighted mean by cell area and median are calculated for each zone and the overall profile between 0 and 6 m. Of course, all these steps have been repeated for all experiments. As a reminder, due to the water sheet flow effect and smoothing of time-constrained processing, the calculated resistivity values cannot be considered as precise and accurate values but can be used to study the relative change and in general, the kinetics of the effect of infiltration on the resistivities.

Figure 3-38 shows the evolution of the mean resistivity for all experiments. If compared to the apparent resistivity graphs (Figure 3-13), common features can be identified. Firstly, the starting resistivity is higher in the miscanthus than in the bare soil as previously observed in the initial conditions profiles. Secondly, the decrease at the start and the overall decrease are greater in the miscanthus. After approximately 20 minutes, it can be seen that lines are almost parallel, suggesting a homogenisation at this stage of the evolution of resistivities. An anomaly that occurred during the second experiment is a small increase in resistivities at approximately 85 minutes. No physical explanation about this phenomenon has been found, except maybe a perturbation of the water sheet

flow changing the conditions at this moment due to erosion of some soil for example, but if that happened, it was not noticed visually during the experiment. After this small increase the trend is the same as the other experiments.

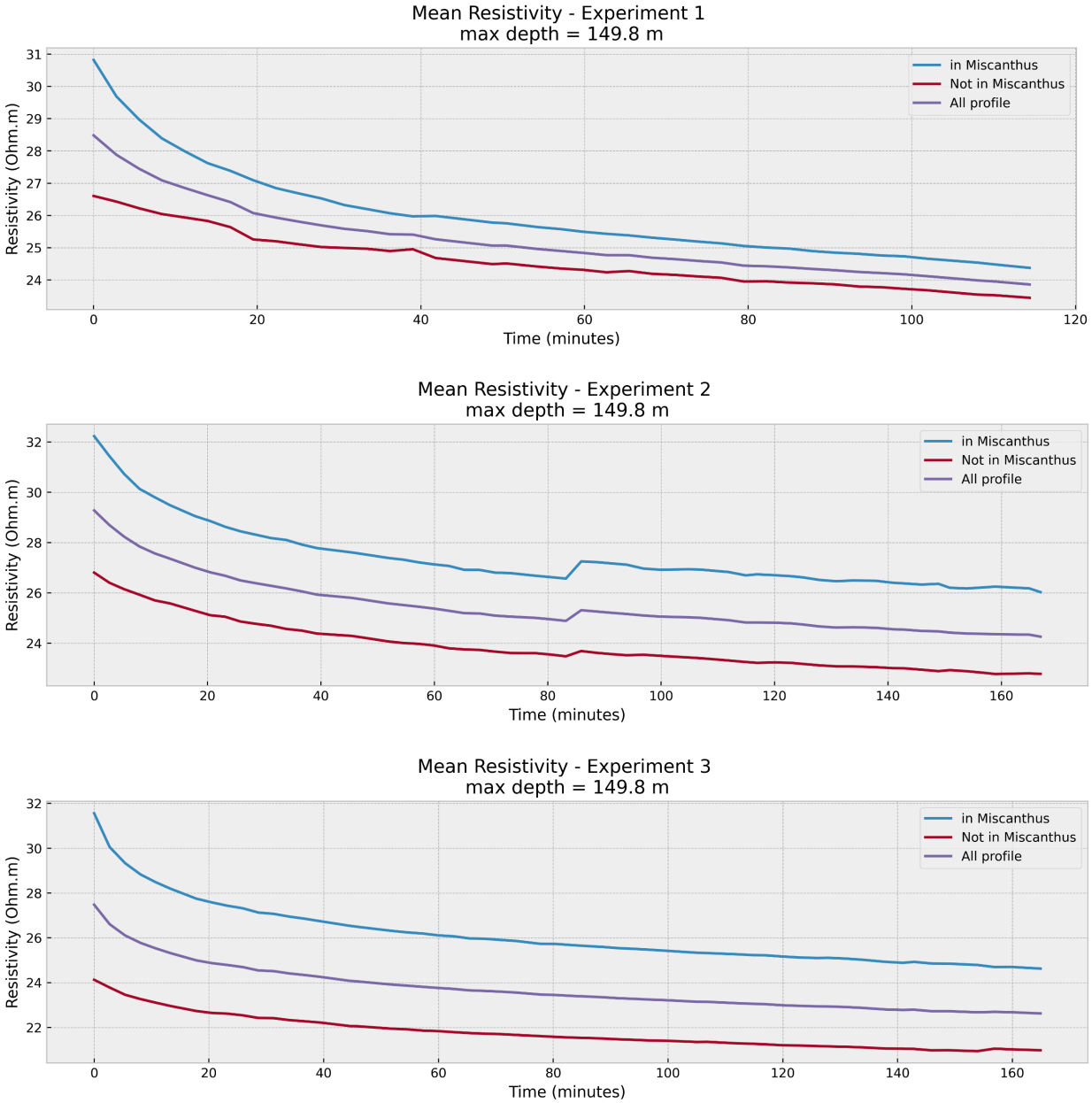

Figure 3-38: Evolution of the mean of the calculated resistivities from surface to a depth of 149.8 m with time-constrained processing in and out of the miscanthus for the longitudinal profile of each experiment.

In Figure 3-39, like the apparent resistivities, the evolution of the decrease with time is also plotted and it can be seen that it also has a very similar pattern of decrease, depending on the half considered and on the overall profile. However, the magnitude of the decrease is less important in these graphs, probably due to the previously discussed effect of smoothing and the water sheet flow.

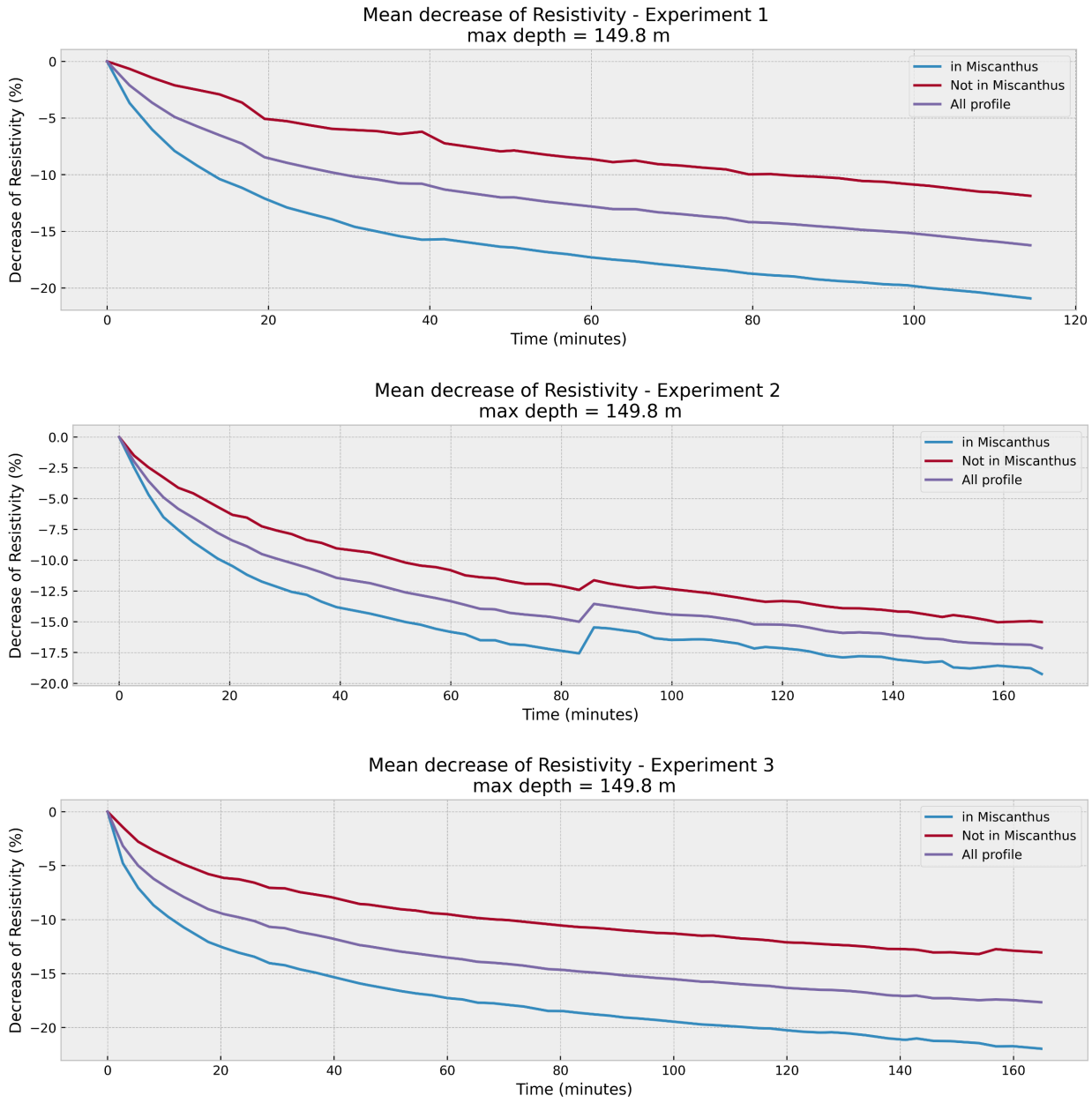

Figure 3-39: Evolution of the mean decrease in the calculated resistivities from surface to a depth of 149.8 m with time-constrained processing in and out of the miscanthus for the longitudinal profile of each experiment.

Median graphs are also plotted (Figure 3-40), and in general reveal the same observations. But it is even better highlighted that the kinetics of the decrease, i.e., the slope of the line, is greater at the start of the experiment in the miscanthus half. It is particularly obvious when looking at the graph of the first experiment (it was already the case in the apparent resistivity graph). But again, from 30 to 40 min the slope is the same in all parts.

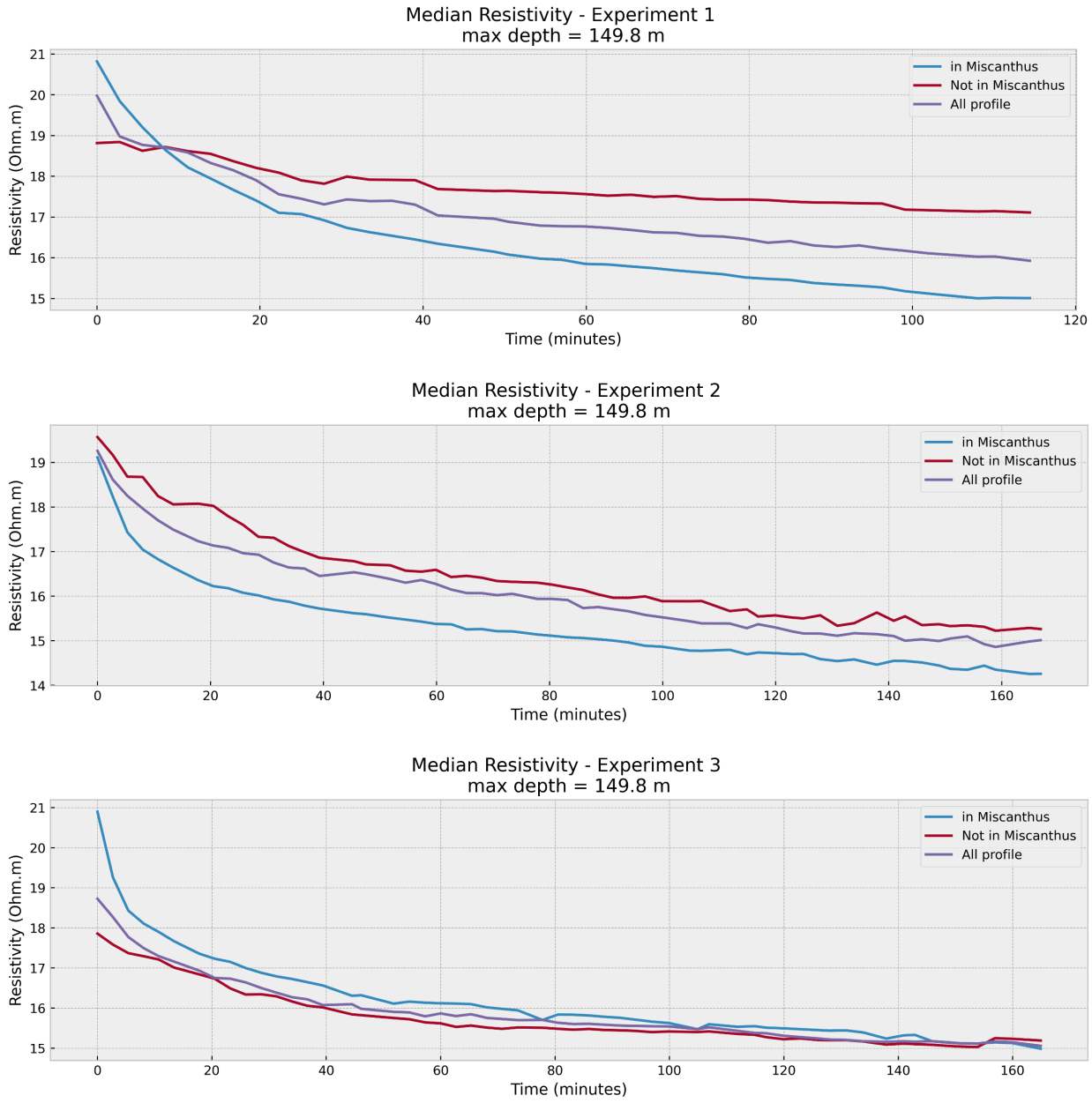

Figure 3-40: Evolution of the median of the calculated resistivities from surface to a depth of 149.8 m with time-constrained processing in and out of the miscanthus for the longitudinal profile of each experiment

3.9. *Water Content modelling - Limitations of Archie's Law Application*

From the theory section, it has been explained that resistivity can be converted to water content. Unfortunately, the representation of this water content for this experiment has not been successful for several reasons.

Firstly, the different empirical parameters necessary to model the water content were not measured, making it difficult to well represent the real relationship between resistivity and water content for this specific soil. Nonetheless, some testing was done with estimations and hypotheses on these parameters, but did not yield satisfactory results with saturation not exceeding 30% at the end of the infiltration. Also, water content measurements were taken before the infiltration at various depths but not after. If some water content measurements were made after, an estimation of the parameters could have been made with the results of the resistivity from inversion.

Secondly, the pore water resistivity of the initial water composing the soil is unknown and the resistivity of the injected water is extremely low. This could have an unknown effect on the validity of the empirical law.

Thirdly, the results of the resistivity profiles do not represent exactly the real resistivity in both processing methods:

- For the standard processing: the artifacts bias the real resistivity in these areas of the profile, but top resistivities are still assumed to be well modelled.
- For the time-constrained processing: it has been proved that the individual resistivity profiles are oversmoothed by the multiple constraints, making it difficult to precisely represent the real resistivity of the profiles, and by extension, to apply the empirical law.

Finally, because of the nature of the soil (silty soil), the validity of the law can be questioned, as Brunet et al. (2010) stated that the law is valid for medium to coarse grained soils.

All these reasons resulted in an inability to accurately represent the water content evolution of the soil, the parameter that could have indicated if the infiltration was more important in the miscanthus part. All that has been demonstrated is that the decrease in resistivity is greater in this half, but this conclusion cannot be interpreted directly as a higher water content overall. Indeed, the following demonstration based on Archie's law proves that the initial conditions are directly affecting the translation of a variation in resistivity into a variation in water content.

Let's start by recalling Archie's law in the absence of clay:

$$\rho = a\,\rho_w\,\Phi^{-m}\,S^{-n}C = a\Phi^{-m} \tag{29}$$

If the saturation (S) is isolated and the constant parameters group into one only constant such as:

$$C = a\Phi^{-m} \tag{30}$$

$$and\ S = \left(\frac{C * \rho_w}{\rho}\right)^{\frac{1}{n}} \tag{31}$$

Once the formula (31) is established, let's consider two different timesteps with a given fixed decrease in resistivity such as:

$$\rho_2 = \rho_1(1-\alpha) \tag{32}$$

with α a given decrease in resistivity. Now, the saturation of both timesteps can be expressed as follows:

$$S_1 = \left(\frac{C\rho_{w1}}{\rho_1}\right)^{\frac{1}{n}} \tag{33}$$

$$S_2 = \left(\frac{C\rho_{w2}}{\rho_2}\right)^{\frac{1}{n}} = \left(\frac{C\rho_{w2}}{\rho_1(1-\alpha)}\right)^{\frac{1}{n}} \tag{34}$$

Because adding a term to the right of the equality that is equal to 1 does not modify the equality, the term $\left(\frac{\rho_{w1}}{\rho_{w1}}\right)^{\frac{1}{n}}$ multiply the right term. S_2 can be rewrite and ΔS calculated:

$$S_2 = \left(\frac{C\rho_{w2}}{\rho_1(1-\alpha)}\right)^{\frac{1}{n}} * \left(\frac{\rho_{w1}}{\rho_{w1}}\right)^{\frac{1}{n}} \Leftrightarrow S_2 = S_1 * \left(\frac{\rho_{w2}}{(1-\alpha)\rho_{w1}}\right)^{\frac{1}{n}} \tag{35}$$

$$\Delta S = S_2 - S_1 = S_1 * \left(\frac{\rho_{w2}}{(1-\alpha)\rho_{w1}}\right)^{\frac{1}{n}} - S_1 = S_1\left(\left(\frac{\rho_{w2}}{(1-\alpha)\rho_{w1}}\right)^{\frac{1}{n}} - 1\right) \tag{36}$$

$$\Leftrightarrow \Delta S = \left(\frac{C\rho_{w1}}{\rho_1}\right)^{\frac{1}{n}}\left(\left(\frac{\rho_{w2}}{(1-\alpha)\rho_{w1}}\right)^{\frac{1}{n}} - 1\right) \tag{37}$$

This final formula puts in evidence that the variation of saturation between two timesteps, is inversely proportional to the n-root of the starting resistivity, and by extension the water content too. So, for a given decrease in resistivity, the variation of water content is smaller if the starting resistivity was greater and inversely, for the same water content variation, the resistivity decrease is greater if the starting resistivity was greater. As an example, common value for n is close to 2 (Brunet et al., 2010), so if a starting resistivity of 100 Ω.m or 50 Ω.m is taken, for the same resistivity decrease, the water content variation will be approximately 40% greater in the lower resistivity area.

3.10. *Conclusion*

Based on the previous subsection, it is not yet possible to determine if the resistivity decrease means a greater water content increase in the miscanthus part, because of all the unknown parameters for expressing a coherent petrophysical relation between resistivities and water content. This direct relation would have been an efficient way to assess the infiltration potential of the miscanthus compared to the bare soil half, even in a quantitative way.

Nonetheless, the resistivity change profiles revealed some interesting infiltration patterns with a clear distinction between the two distinct halves of the infiltration band. The qualitative assessment of these profiles revealed a greater decrease in resistivity in the miscanthus where the more resistive areas of the profiles are as well. But especially, an earlier appearance of the infiltration pattern during the infiltration test in the miscanthus with timelapse analysis. In addition, the timelapse analysis revealed that the evolution of resistivities was notably different at the start of the experiment as the apparent resistivity studies already highlighted. Until 30 min into the experiment, the slope of the miscanthus line is steeper than the slope of the decrease in the bare soil half.

To better visualise the infiltration patterns, every longitudinal profile of each repetition is plotted in a 3D space (Figure 3-41). This representation allows us to determine that the experiment gave similar results every time it was repeated. The separation of each part of the profile is represented by the perpendicular transparent plane. The miscanthus part is on the right of the images, it means the start of the runoff infiltration is at the left of the image, i.e., at the top altitude of the profile. For the resistivity change figure, the legend is modified so only decreases in resistivity appears, the small remaining artifacts are then masked.

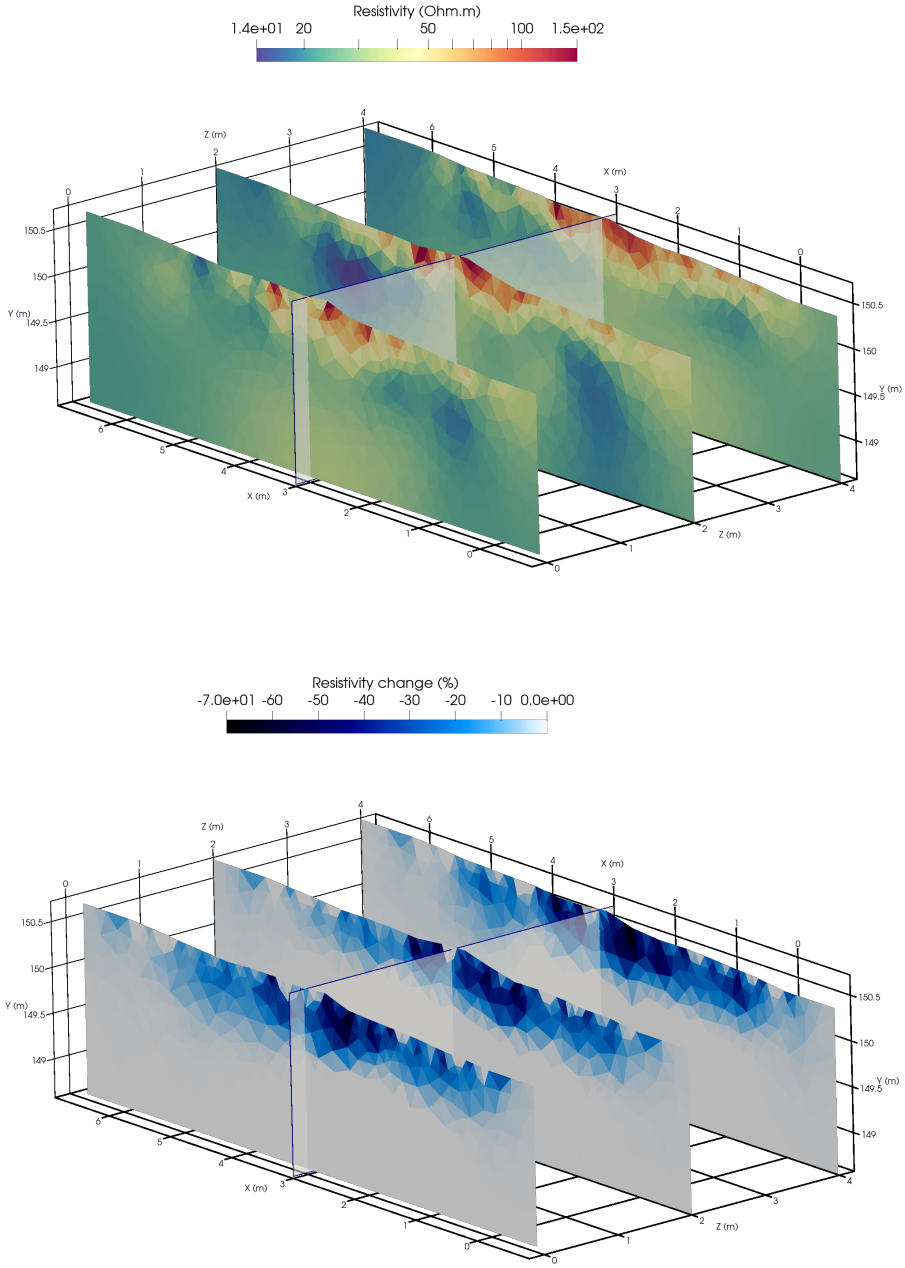

Figure 3-41: 3D representation of the initial conditions results (Top) and the resistivity change after infiltration with time-constrained processing (Bottom) of longitudinal profiles of each experiment

For the experiment 1, the perpendicular profiles are also represented with their respective longitudinal profile (Figure 3-42). In this image, the infiltration front coincides between longitudinal and perpendicular profiles, reflecting a good representation of the infiltration pattern. Again, the differences between both halves are highlighted in this view, in the initial conditions and in the infiltration pattern. The orientation is the same as the previous figure.

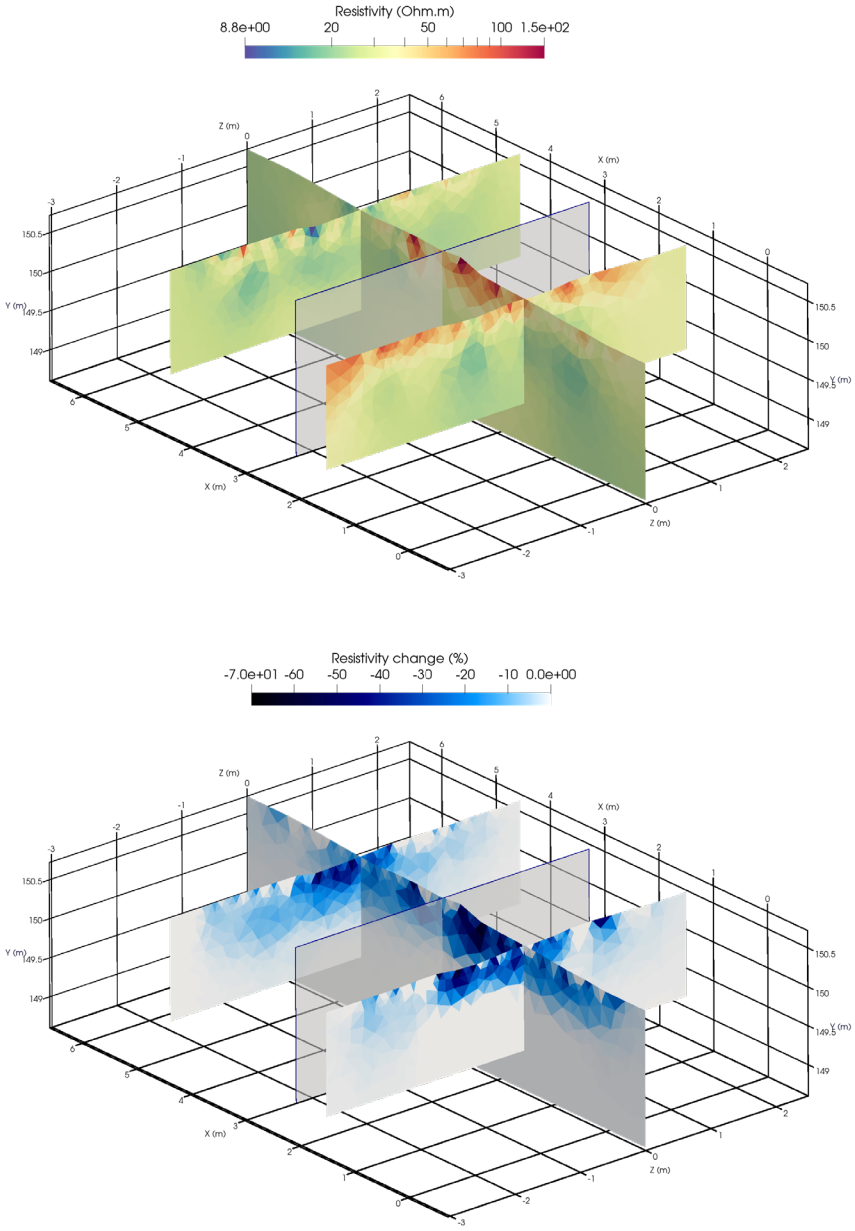

Figure 3-42: 3D representation of the initial conditions results (Top) and the resistivity change after infiltration with time-constrained processing (Bottom) of the longitudinal and perpendicular profiles of experiment 1

The interpretation of the overall infiltration is still complicated, especially due to limited knowledge of the water content. But it has been revealed that infiltration seems to be limited to the upper portion of the soil, this correlated with the change of horizon in the initial conditions. The interpretation is that the hydraulic properties of the lower level of soil do not allow infiltration to occur at this time scale, then infiltration is limited to the upper boundary of this horizon. This could explain the more important lateral variations in the perpendicular profile not in the miscanthus where water flows laterally because it cannot flow vertically anymore, like the study of (Hübner et al., 2017) where they prove that layered structures were limiting the vertical infiltration. If this is true, it means that in the miscanthus part, the capacity of water retention could be more important because no lateral fluxes are observed, so water is still accumulating directly below the band, rather than to flow laterally. Another unknown is the presence of fluxes in the direction of runoff within the first layer of soil. This higher decrease in resistivity in the miscanthus can't be directly translated in a better infiltration but the other observations comfort the idea of an eventual better infiltration, even with the initial conditions, where higher resistivities could imply lower starting water content, meaning a higher water deficit and then greater infiltration. It is also supported by the greater starting kinetics during the timelapse analysis in the miscanthus half.

4. Infiltration Stick

In this section, a new practical case of infiltration monitoring by ERT is investigated. The specification of this practical case is that compared to the first one, the objective here is not only to image infiltration but also to validate an acquisition tool. This tool is a stick that includes electrodes and an injecting system to measure infiltration rate in a small borehole. The objective here will be to compare the data acquired with this infiltration stick with a classic ERT setup with stick electrodes and see if the quality of the data is comparable and the data interpretable. It is mainly here to validate the experimental setup of the infiltration stick.

4.1. *Stick Configuration*

The infiltration stick has a total length of 230 cm, but the total length of the electrode array measures 200 cm. The diameter is only 5 cm large that can allow the stick to be inserted in small borehole even made by hand with an auger in soft unconsolidated soils. The stick is also composed of a tube system to allow an infiltration at the middle of stick where few holes are present to let the water flow in the studied environment. A junction is present on top of it so that a tube can be connected to the stick, tube that can also be connected to a pump allowing a constant injection during data acquisition. Concerning the electrodes, they are stainless steel rings and there is 8 of them along the stick, their geometry differs from classic electrode configuration because of their spacing that is not regular. Indeed, the three electrodes in the upper part of the stick are separated by 10 cm, the third and the fourth by 20 cm and the remaining ones by 40 cm. The full configuration of the infiltration stick is visible in the Figure 4-1, except for the injection hole located in the middle of the electrode array.

The Figure 4-2 shows the 3D model used to manufacture the stick. In these pictures, it can be seen an overview of the stick with a more detailed view of the top of the stick where the electrical cables are connected with the water input, but also the middle of the stick where the injection holes are located and the disposition of the different ring electrodes. In this representation, the wiring and water tubes inside the stick are not represented.

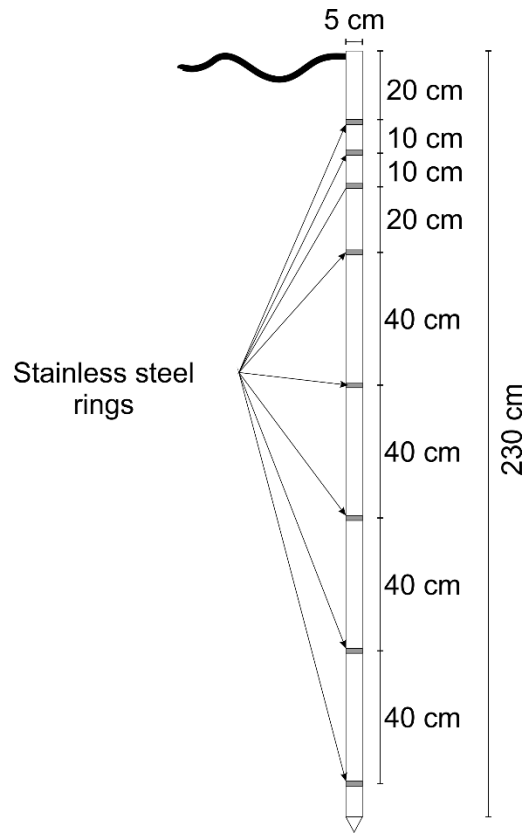

Figure 4-1: Schematic of the infiltration stick configuration

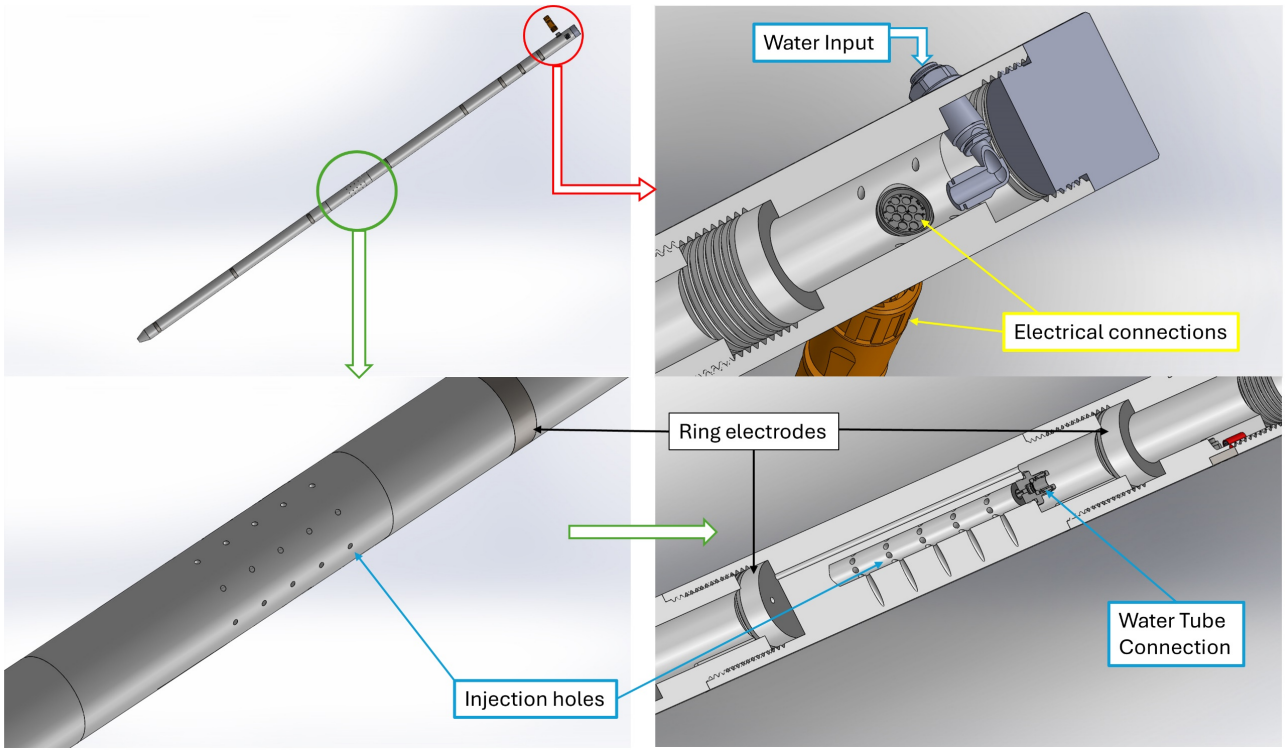

Figure 4-2: Detailed Views of the 3D model of the Infiltration stick

4.2. *Experiment*

To evaluate the Infiltration ERT stick, the experimental site chosen is the basement of the B52 building of the University of Liège that allows a direct access to a sand formation from the Oligocene. This is mainly a yellow sand nonindurated with some silex rocks present. However, a nearby borehole relates that this sand can also be sometimes indurated and has a thickness of approximately 2 m, i.e., greater than the depth of investigation that can be achieved with the chosen setup. (Robert & Bolly, 2015)

4.2.1. Experimental Setup

Because it needs to be compared to a reference, the stick will be used horizontally next to a classic setup. A small trench adapted to the dimensions of the stick is dug and it is installed inside it, then a sand cover is applied on top of it. At the same time, electrodes are planted approximately 10 cm from the stick with the same electrode configuration as the stick, i.e., 8 electrodes with irregular spacing. The stick is then connected to the ABEM Terrameter LS2 and with tubes to a pump, which is itself connected to a 120 L water tank.

The picture of the experimental setup from the Figure 4-3 shows the experimental configuration of the infiltration stick that is buried and represented by the red rectangle and the classic electrode array right next to it.

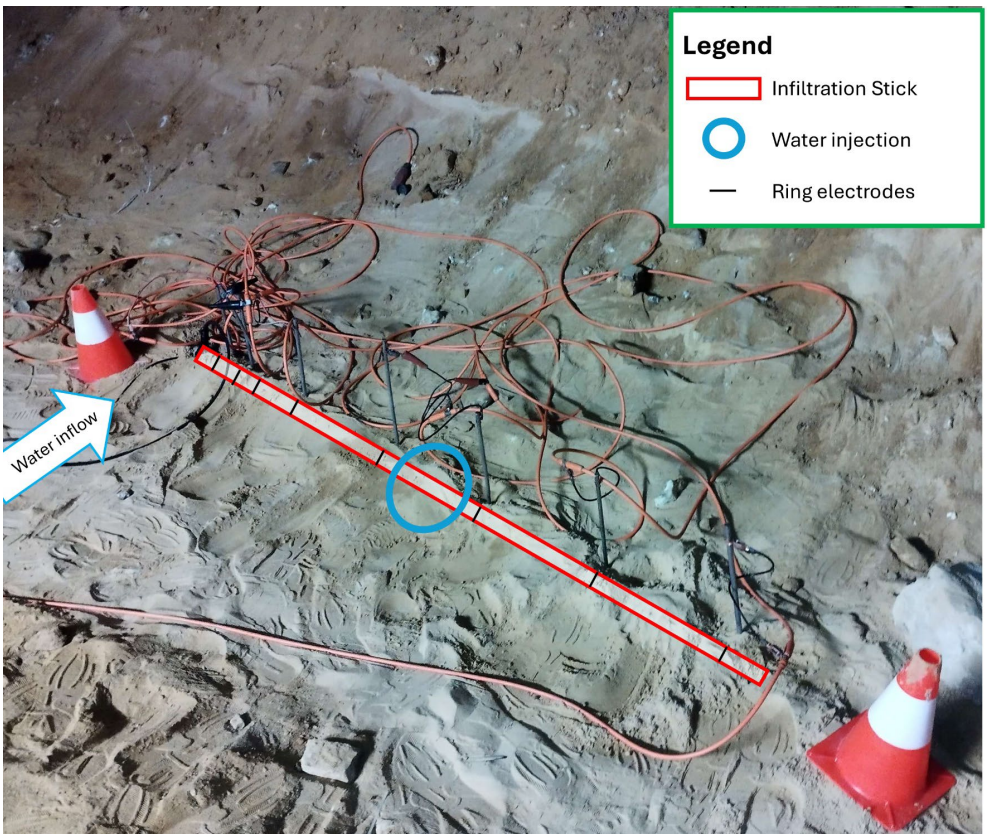

Figure 4-3: Picture of the experimental setup of the stick and the electrode array

4.2.2. Infiltration and ERT Parameters

Like the previous experiment, Dipole-Dipole array coupled with a Gradient array protocol is chosen. Due to the limited number of electrodes this combined protocol includes only 17 datapoints (9 and 8 respectively). The script for the automation of the ABEM Terrameter includes 10 measurements on the stick, 1 measurement on the electrode profile, another 10 measurements on the stick, 1 full reciprocal measurement on the stick, this protocol is then repeated. In 1 hour, 33 measurements are taken.

Concerning the infiltration rate, it has been measured by a bucket test that with a 32 rpm rate on the pump, the flow is about 0.42 L/min. Salt is also added to the injected water.

4.2.3. Course of the Experiment

The experiment was conducted on 26/04/2025. 2 background measurements were made before the start of the infiltration process on the stick and the classic electrode array. 2 full reciprocal measurements were also performed on both setups. The same acquisitions were also performed at the end of the infiltration. The water injection and timelapse experiment lasted from 10h54 to 15h53 for a total length of 5 hours and 2 minutes, at 15h24, the flow rate was doubled to consume the total volume of the 120 L of the water tank. The electrical conductivity of the injected water was 14.55 mS/cm, measurements of the conductivity were made during all the experiment, but the value did not fluctuate by more than 0.02 mS/cm.

A main issue occurred during the acquisition with the instrument making a lot of measurements unusable or sometimes not recorded. At the end, only the first hour and the third hour of acquisition were retrieved. Once the issue was discovered manual measurements were performed and correspond to the 30 last minutes of the experiment.

4.2.4. Challenges

The main challenge of this experiment is to assess the efficiency of the infiltration stick, by determining if this tool can be efficient to monitor infiltration evolution in a small borehole and its differences when compared to a classic setup.

It is important to assess the accuracy of this stick because for later experiments, this kind of equipment can be coupled with a classic surface profile as what was done in the previous experiment. This combination will allow a greater resolution in depth and to infiltrate water directly below the surface.

4.3. *Data Quality*

In the same spirit as the previous experiment, data quality must first be assessed before proceeding to processing. In this case, the assessment will be a bit different because it can already be used to compare the two different setups.

Firstly, the plots from the Figure 4-4 represent the comparison between the measured resistance in the normal array versus the measured resistance for the reciprocal array. A trend line is interpolated between these points and as a reminder, the closer the points are to an identity line, the better the quality. Figures display these plots for background and after measurements for both setups.

The distribution of the different scatter plots seems well distributed and does not seem to deviate significantly from the identity line as the trend line equations suggest. Indeed, both parameters of the trend lines are close to their ideal values (1 and 0 respectively). Only the data from the background of the stick have a greater second parameter, nevertheless, this higher value is not abnormal as it represents only a small value compared to the amplitude of the resistance value. It is also observed that for the after-infiltration measurement, this larger error is not present.

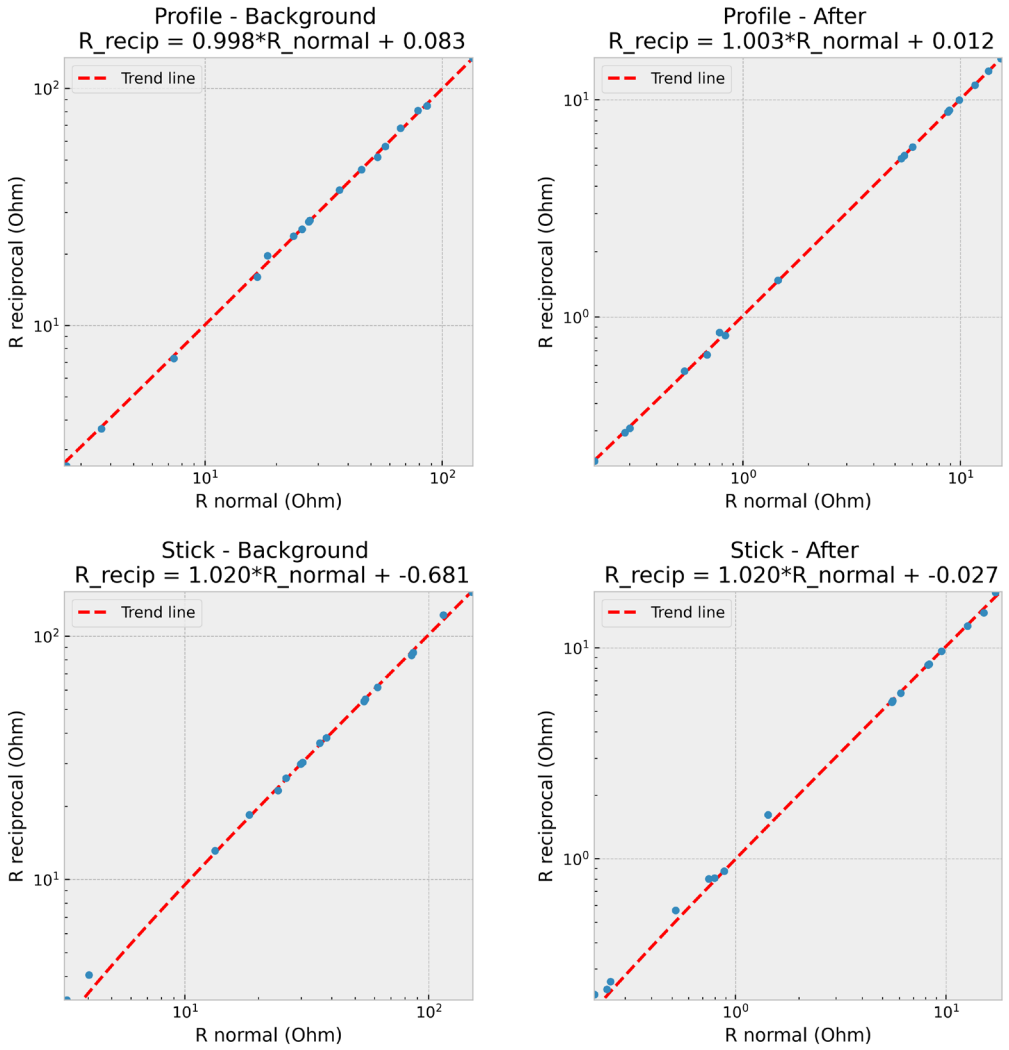

Figure 4-4: Resistance comparison of normal and reciprocal measurements for the electrode profile (Top) and the infiltration stick (Bottom) for Background (Left) and After Infiltration (Right) measurements

The analysis of the relative error between measurements also reveals an overall homogeneity in the data quality between measurement times and setups (Figure 4-5). No obvious or significant outliers are present, but errors can still reach important values, especially in the after-infiltration measurement where low resistances present a high relative error but never exceeding 10%. Nevertheless, majority of the points present a lower error than 3% and errors are generally greater in the after-infiltration data.

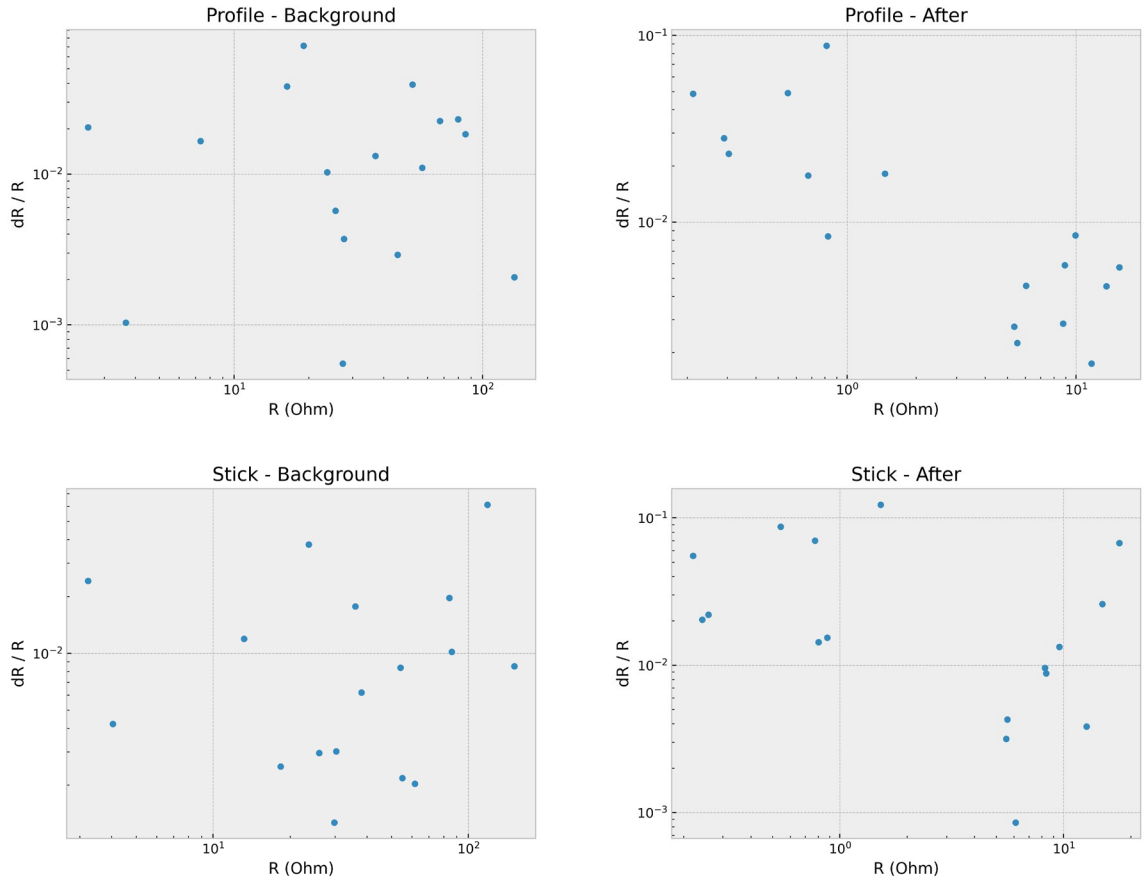

Figure 4-5: Reciprocal error in function of the resistance measurements for the electrode profile (Top) and the infiltration stick (Bottom) for Background (Left) and After-Infiltration (Right) measurements

Another way to visualise the relative error between normal and reciprocal measurements is by simply plotting all the error values on a histogram for every acquisition (Figure 4-6). As observed in the previous figures, there are generally a majority of measurements below the 3% threshold. The distribution of the errors is very similar between the setups for the same timestep. And as was inferred from the interpretation of previous figures, there is presence of more significant errors in the after-infiltration measurements compared to the background.

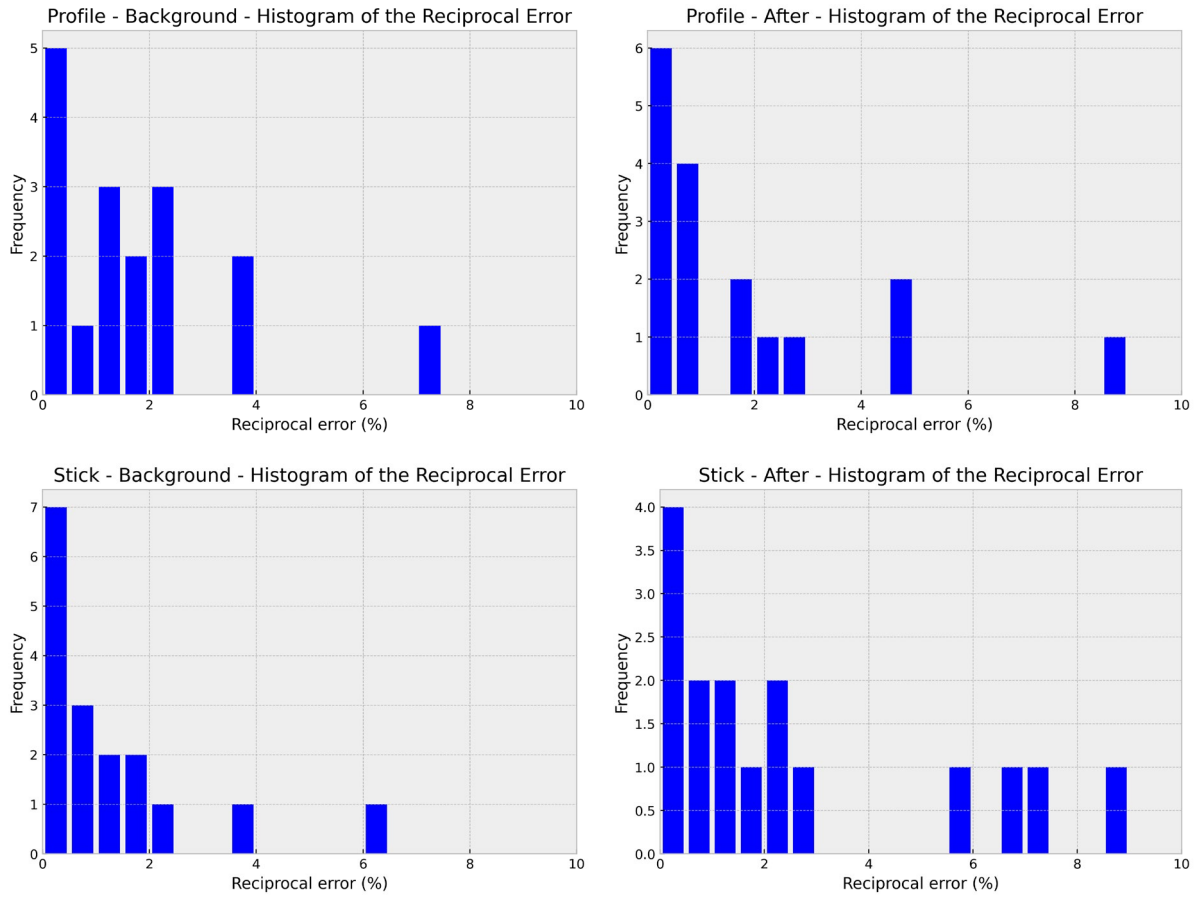

Figure 4-6: Histograms of reciprocal errors in function of the resistance measurements for the electrode profile (Top) and the infiltration stick (Bottom) for Background (Left) and After-Infiltration (Right) measurements

Because of the issues with the automated data acquisition, only 2 reciprocal measurements were collected during the infiltration. This amount of data does not allow a study with time of the reciprocal data like what has been done in the miscanthus experiment. Nonetheless, they can still be analysed separately the same way it is done with the background and the after-infiltration measurements. The two reciprocal measurements were performed after 33 min and 160 min from the start of infiltration, the different figures related to their analysis are available in Annexe 19. In this figure, it is still visible that early in the infiltration, the second parameter (b) of the trend line is still more important but has drastically decreased after 160 min. The overall distribution of errors in the histograms is similar to the background and after infiltration but there are more errors close to 3% and higher for the timestep at 33 min.

In conclusion, the overall data quality is satisfactory, and no major outliers are present. The input of infiltration does not modify the data quality considering the analysis of the two reciprocal datasets during infiltration. Concerning the comparison between the stick and the classic electrode profile, error distributions were similar for the same timesteps, but a slightly higher deviation of the points from the identity line on the scatter plot comparing the resistivities for the background data of the stick but is not considered a big issue due to the small value of this deviation and because

of the configuration of the stick. Indeed, the ring electrodes can have a limitation in their functioning because the stick was horizontal and only a thin layer of sand covered it, contact with electrodes and current line directions are probably not optimal.

4.4. *Results & Discussion*

This section will focus on distinct aspects. Firstly, comparing the different results of both setups with retrieving similarities and assessing the efficiency of the stick. Then, the data will be interpreted to specifically study if the infiltration can be characterised by the setups, but most importantly by the stick.

4.4.1. Apparent Resistivity Study

Like in the miscanthus infiltration test, the first study before proceeding to more complex processing is the study of the apparent resistivity.

To begin with, the 17 datapoints retrieved for each acquisition are compared between the setups for background and after-infiltration measurements. If the setups retrieve the exact same apparent resistivity for the same measurement point it means that the setups are equivalent. However, the spatial difference between the two setups (spacing between them of about 10 cm) and their interference with each other add some uncontrolled variability to the acquired data.

To analyse the data, scatter plots comparing the apparent resistivities for both setups are displayed (Figure 4-7). In these figures, it can be first assessed by observing the axes that background apparent resistivities are higher by one order of magnitude compared to the after-infiltration measurement. In the background, the points are sparse around the identity, but they still follow the general trend of the line. Some points are clearly deviating from the identity line, especially the highest apparent resistivity point. This deviation is no longer visible in the after-experiment figure, where the general trend seems to better fit the identity line.

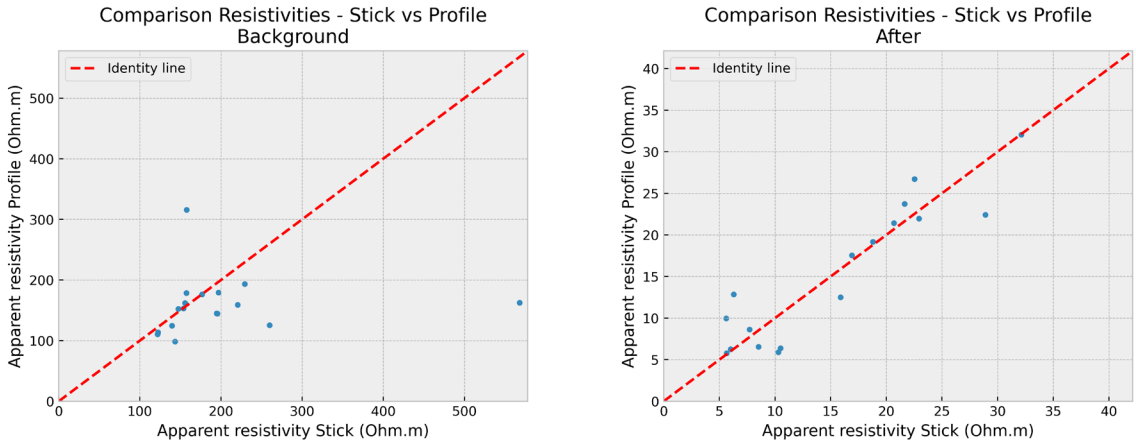

Figure 4-7: Comparison of the apparent resistivities of each setup for Background (Left) and After-Infiltration (Right)

A way to quantify the differences that exist between the two setups is to study the absolute difference and the relative difference between each datapoint.

Firstly, the absolute differences (Figure 4-8): for the background, most of the datapoints don't have an absolute difference greater than 50 Ω.m, this difference seems greater if the measured apparent resistivity is greater. Concerning the after-infiltration data, the absolute difference is lower, also because the measured apparent resistivities are lower, however, no trend appears in this scatter plot.

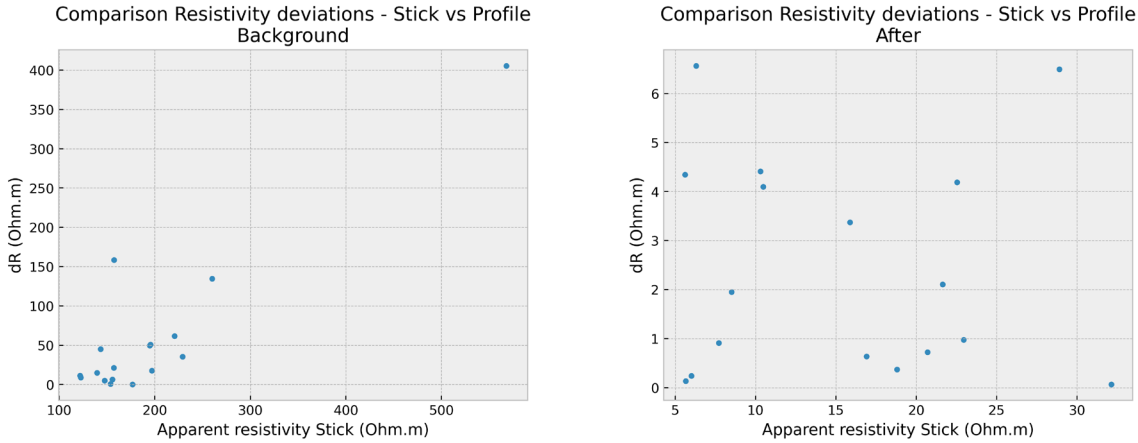

Figure 4-8: Deviation of resistivity between setups in function of the apparent resistivity value for Background (Left) and After-Infiltration (Right)

Relative differences give another point of view to the comparison (Figure 4-9). For the background, most of differences are lower or close to 30% while some points have significantly larger differences, these are two points that were further from the identity line in Figure 4-7. The same order of magnitude for the relative difference is observed in the after-infiltration scatter plot.

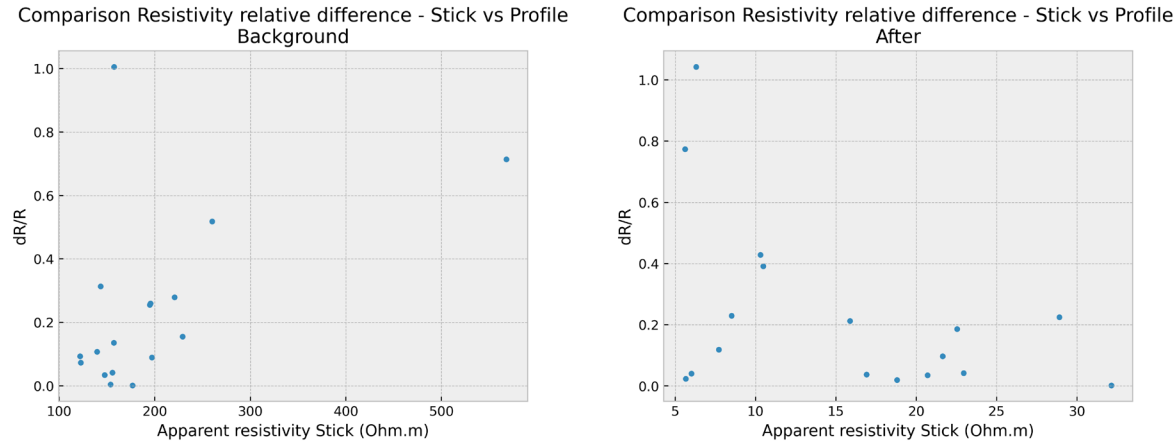

Figure 4-9: Relative difference of resistivity between setups in function of the apparent resistivity value for Background (Left) and After-Infiltration (Right)

From this analysis, it is observed that it exists similarity between the acquired data, that is a good sign of the efficiency of the stick, but some datapoints present greater deviations, it cannot be directly concluded that these differences are linked to the acquisition instrument, indeed, the positions of the setups and additionally their interference could explain these differences, but also the horizontal stick setup, which prevented an uniform soil cover around the ring electrodes.

After analysing the static apparent resistivities, the evolution between the different timesteps can be investigated by simply taking the mean and median of apparent resistivities for every timesteps (Figure 4-10). For reminder, there is only data during the first hour, the third hour and the last 30 min, the rest of the graph is simply a linear interpolation between the last and the first measurement of each sequence. The acquisitions on the electrode profile are represented by points with a linear dashed line interpolation between them.

In Figure 4-10, firstly, the dynamics of the resistivity evolution can be analysed. At the very start of the infiltration the resistivity first increases then drastically decreases very shortly after. The beginning of the decrease is very sharp and tends to stabilise after a few minutes to constantly decrease after approximately 50 min. Once the infiltration rate is doubled, the effect is a sharp decrease in the mean resistivity a few minutes later. Concerning the comparison between the stick and the electrode profile, the dynamic is remarkably similar especially with mean plot while the median is generally higher for the electrode profile, but the line possesses a slope close to the one of the stick line. The starting point is the same for the median for both setups but is smaller for the mean of the electrode profile. What is interesting is the increase at the start of injections especially visible with the median line, unfortunately, no acquisitions were performed on the electrode profile during this increase, making it difficult to determine if this phenomenon was real or an effect induced by the stick.

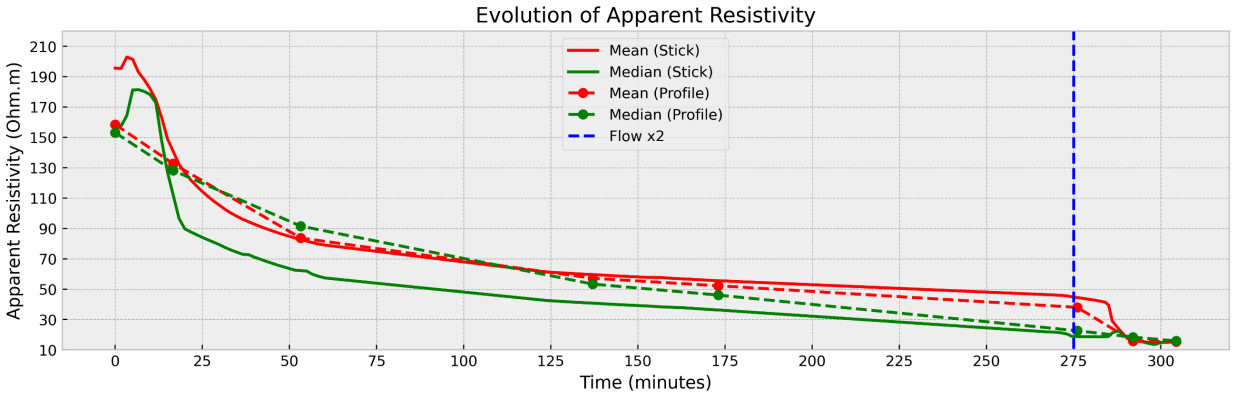

Figure 4-10: Evolution of the mean and median of apparent resistivities for each setup with time

One specific datapoint has been chosen to study the apparent resistivity evolution only for this point (Figure 4-11). This point relates to the measurement where the injection electrodes were situated at X = 0.4 m and 0.8 m, and the measurement dipole at X = 1.6 m and 1.8 m, so that the datapoint has a pseudo-position at X = 1.15 m, almost in the middle of the profile and a pseudo-

depth of 0.45 m. An increase in resistivity can be observed also at the start and a quickly decrease afterwards. A low resistivity is then reached after approximately only 25 minutes to reach values close to zero later on. Because of the exceedingly small value already reached, the increase in infiltration rate is not reflected on the graph. Concerning the electrode profile, the spike at the start is not visible because no data were taken during this time, the starting resistivity is close to the stick one, but the overall resistivity is clearly higher from 20 minutes to the end. This can be an effect due to the fact that the injection point is shifted compared to the profile.

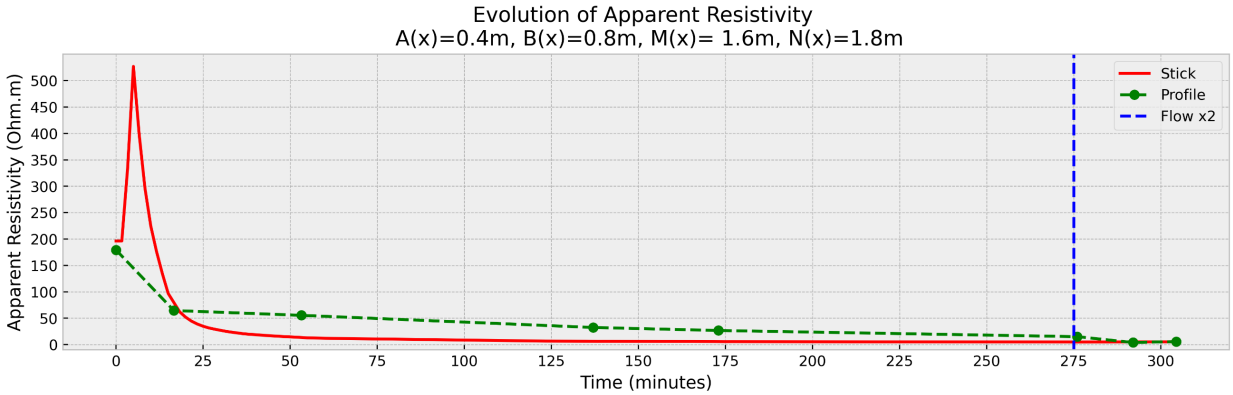

Figure 4-11: Evolution of the apparent resistivity of a single datapoint close to the middle of the profile for each setup with time

Evolution of the standard deviation of the apparent resistivities can also be plotted (Figure 4-12). It is interesting and encouraging for the use of the stick because both standard deviation evolutions have a similar pattern with an increase at the start followed by a decrease, a stabilisation during infiltration, and a sharp decrease when the infiltration rate is doubled.

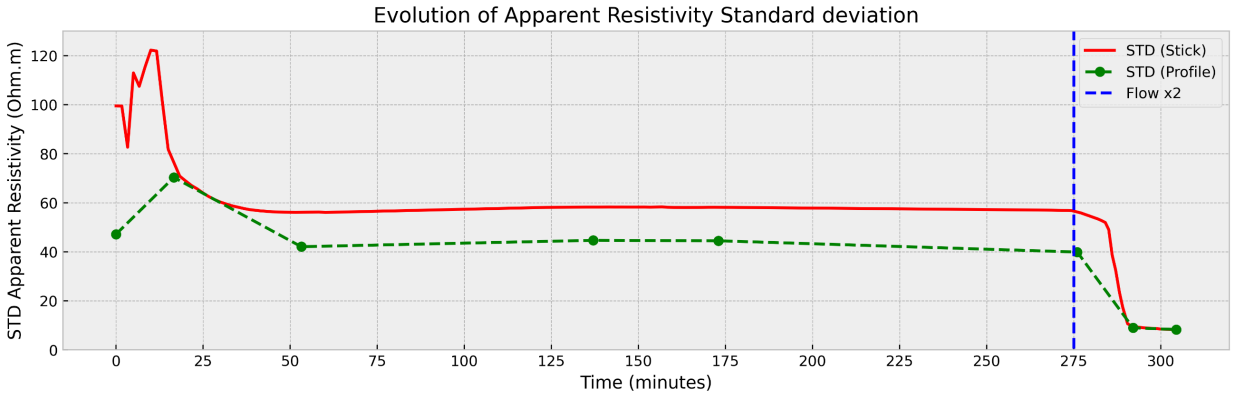

Figure 4-12: Evolution of the standard deviation of apparent resistivities for each setup with time

4.4.2. Inversion Results

Because of the limited datapoints for each acquisition due to the low number of electrodes, the inverse problem possesses a lot of unknowns compared to a classic ERT dataset, the consequence is that it is difficult to obtain a satisfactory result. It will then be difficult to interpret the different profile results.

The background result reveals an overall homogeneous background with comparable results between the stick and the electrode profile. This is interesting because despite the differences spotted in the apparent resistivity values, it can still represent the medium the same way, with the same areas of high resistivity on the top and right of the profile (Figure 4-13). However, overall higher resistivities are observed in the stick profile.

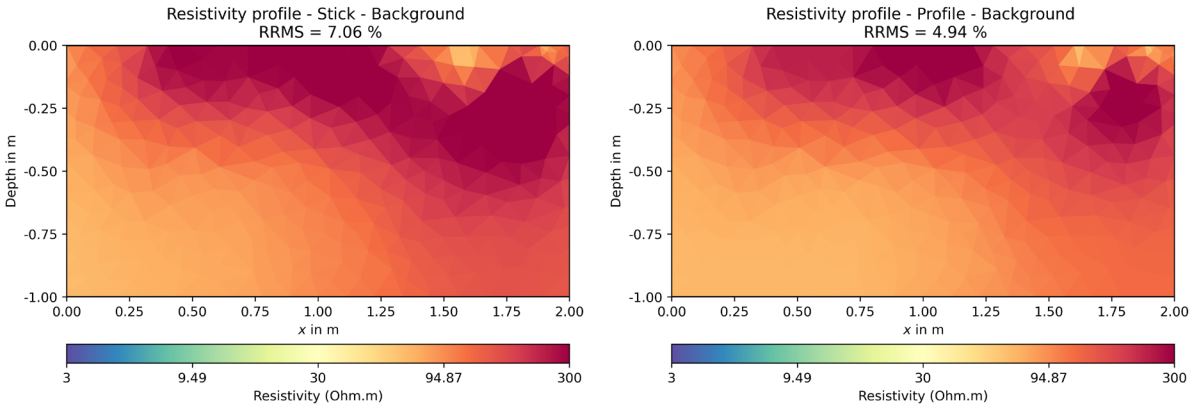

Figure 4-13: Background profiles for the stick setup (Left) and the electrode profile (Right)

Coverage profiles of background data are also similar, showing an overall comparable sensitivity between the two setups.

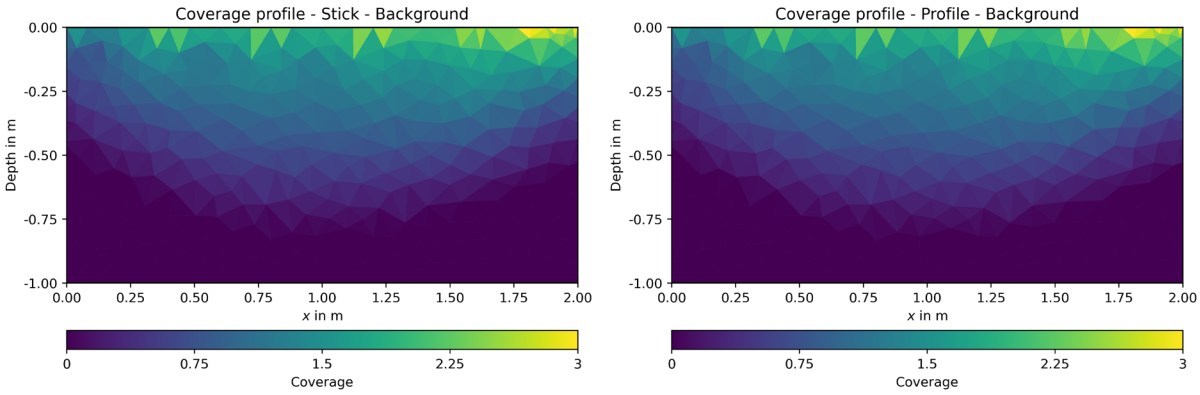

Figure 4-14: Coverage profiles of background for the stick setup (Left) and the electrode profile (Right)

Then, the timelapse frames were also processed using the standard processing scheme, because of the already high error due to the number of datapoints, no further processing was realised as it will not improve the solution, and the objective was mainly to assess the efficiency of the stick. Another issue that can also affect the timelapse frames is the too strong contrast with the background because of the very low resistivity of the injected water. It is also supposed that after a certain amount of time the interaction between setups becomes important as anomalies appear in the inversion results in the form of single cells with very low values, but this can also just be the effect of the accumulation of water creating very low resistivity areas that can't be described because of the background constraint. In Figure 4-15, this effect is clearly visible on the image after approximately 50 minutes. While in the images after 15 minutes, it is visible that on top of the profile and at a depth of about 25 cm, there is a resistivity decrease area related to the water infiltration, this is exactly the position of the injection of water, so despite the low resolution, high error, and low number of datapoints, changes of resistivities are still represented.

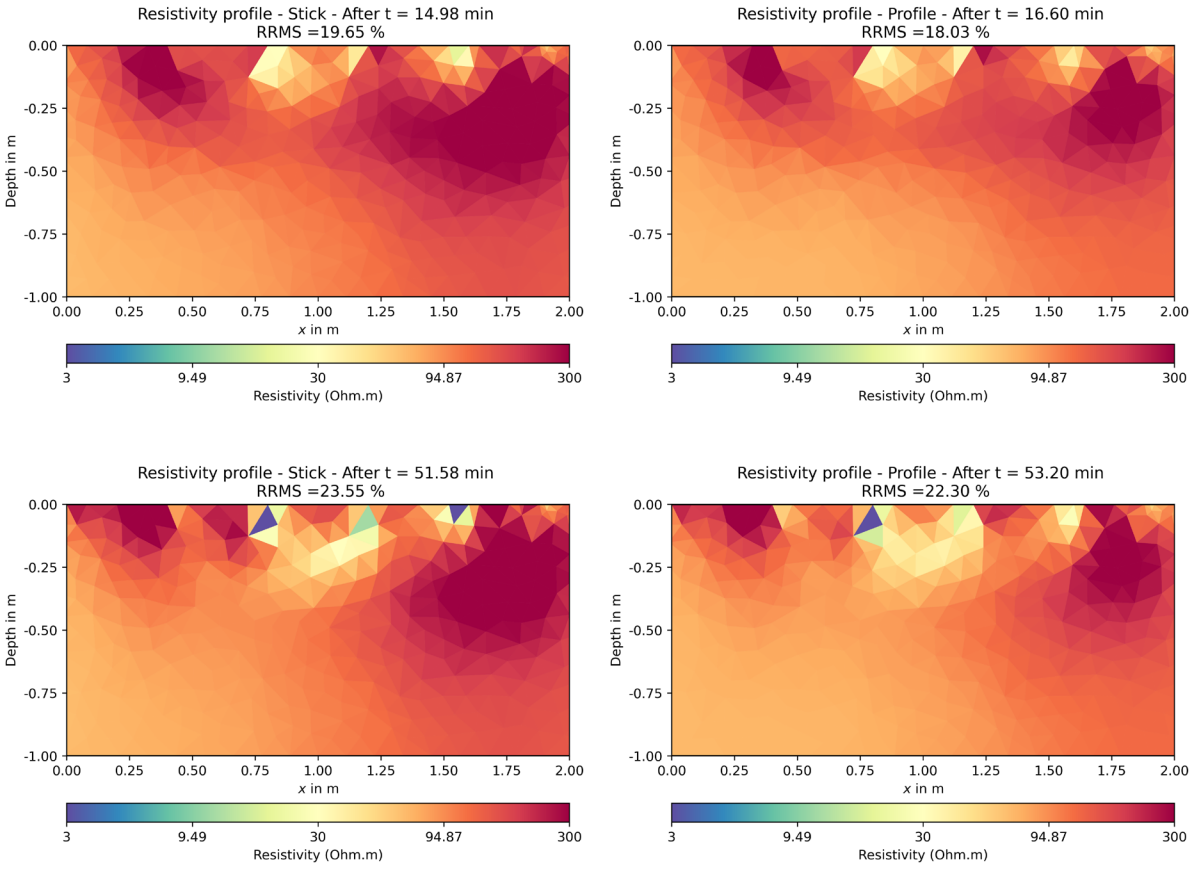

Figure 4-15: Resistivity profiles at two different timesteps for the stick setup (Left) and the electrode profile (Right)

4.5. *Conclusion*

Despite the issues that occurred during the acquisition and with data inversion, the objective of the infiltration stick test has been completed. With the various analysis operated on the data, it has been proven that the stick provides satisfactory data quality and can have results close to a classic electrode profile with the same spacing and configuration if the spatial differences between setups and their interactions are omitted. Also, better results are expected in a borehole because of the soil homogeneity around the ring electrodes, as only a thin layer of sand was present on top of the stick in this test, which could have a direct effect on the data quality and accuracy.

Finally, the inversion results proved that this setup is not intended to be used alone because of its limited number of electrodes. However, coupling this setup in a borehole with a classic surface electrode profile will help increasing the resolution and accuracy of the generated images, especially in depth. In addition, the stick allows infiltration of water directly into the ground.

5. Conclusion & Perspectives

Electrical Resistivity Tomography has proven its efficiency to study infiltration processes in various studies and in this work. It has been revealed to be a great tool to map infiltration patterns and water infiltration dynamics even without complex processing, with apparent resistivity study, for example. The timelapse inversion processing presented a few challenges, some that were already present in numerous studies principally including artifact generation, while other challenges were specific to the experiments conducted in this work (water sheet flow). Some of these issues were managed by using a forward model allowing control of the model and understanding of possible misinterpretations and sources of error. In the context where water infiltration is of major interest in different situations such as flash floods, aquifer recharges, pollution leaching…: having tools, that can better assess and manage the solutions to improve or simply study infiltration, is key.

The result of the conducted experiment, where infiltration was monitored by Electrical Resistivity Tomography in a miscanthus parcel, revealed positive indications of improved infiltration. However, limitations in the study prevent us from concluding this with full certainty. The hints that suggest this are: the greater dynamics of the resistivity decrease in the miscanthus zone and the overall greater decrease in this zone, although it is not necessarily proof of greater infiltration (cf. Section 3.9). If infiltration is studied on its own, without spatial distinction of the soil type, the imaging of infiltration is satisfactorily represented, with determination of an infiltration front that seems to be limited to a certain depth (40-50 cm) and is probably limited by a change of soil horizon, preventing deeper infiltration at this time scale. Despite overall over smoothing necessary to obtain an image without artifacts, interpretations of the infiltration patterns are conclusive. The three repetitions resulted in very similar results, demonstrating the consistency and reliability of the experiment. Also, hydraulic conductivities of soil samples revealed higher values in vegetated soils compared to bare soil, correlating with the results of the ERT data (2.3×10^{-6} m/s for the vegetated soil vs. 8.3×10^{-7} m/s for the bare soil).

Concerning the perspectives of the miscanthus experiment, firstly, there are several factors in the ERT setup that can be improved to acquire better data. The resolution can be drastically increased by reducing the spacing between the electrodes, for example from 0.4 m to 0.2 m, as it is usually done in studies that operate at this spatial scale. This reduction of the spacing can also come with an increased number of electrodes to keep the same overall depths of investigation. Directly with increasing the number of electrodes, the number of datapoints per acquisition will increase, also improving the resolution of the inversions and probably reducing the overall error of the inversion thanks to the increase in data volume. The drawback is the acquisition time that will be increased, therefore, if the same infiltration rate is applied to the system, the change during a single acquisition could be too high and then not representative of a specific time because, for example, the first datapoint can be acquired in a totally dry soil while the last datapoints will be acquired when water already partially infiltrated the top soil. With the performed acquisition in the

experiment, the time scale was small enough to consider the changes during acquisition negligible. Still concerning the ERT setup, the longitudinal profile was completely in the infiltration band, this could induce inaccuracies especially on the borders of the profile, so this profile could be partially out of the infiltration band, like the perpendicular profiles.

Secondly, because the change of the ERT setup implies also changing the infiltration rate to ensure a good acquisition of the data, the infiltration setup can be modified as well. At the same time, the water sheet flow can be controlled and possibly avoided. For that, a few possibilities can be investigated, the best way to monitor the miscanthus infiltration capacity will be to study the infiltration in natural conditions. This presents numerous constraints because acquisition setups need to be ready when significant precipitation occurs, and there is no control over the infiltrated water as well. Additional instruments could be necessary to retrieve information about the exact precipitation. If the same setup is kept to avoid the constraints of acquiring data at an undetermined moment and based on random factors such as the weather, the infiltration rate could be reduced because of the quick kinetics observed in this experiment with a 1 L/s injection, also, a lower injection rate might not create a water sheet flow if the flow is slow enough to infiltrate most of the water. Nevertheless, it is important not to deviate too much from the runoff conditions because these are exactly the conditions in which miscanthus is important, as it has been reviewed, to help avoid water erosion for example.

Thirdly, in the same spirit, other parameters of the experiment could be improved. Adding salt to the infiltrated water was, at the start, proceeded to try to enhance an important contrast, but maybe at the end, these additional contrasts, induced by a low resistivity of the water, were not necessary and even created problems, as the great magnitude of artifacts was probably partially due to this strong contrast between background and infiltration frames. This also increased the effect of the water sheet flow, as a lot of current was directed directly into this salted water. Most studies did not increase the conductivity of the infiltrated water and still observed changes, so it was not necessary, especially with the high injected volume.

Finally, for future infiltration timelapse ERT experiments, not specifically in miscanthus, as already mentioned, the infiltration stick can be a great tool to increase resolution in depth and allow infiltration directly below the surface. Of course, due to limited resolution alone, this stick must be used with classic surface ERT setups. If the combination of surface and borehole electrodes proves to be efficient, an improved stick can be designed with more electrodes, better adapted electrode spacings, and maybe a better tube system inside the stick, because now the infiltration rate is limited by the small diameter of the tube. From a processing point of view, the various regularizations that exist in the literature can be applied for those that have been revealed efficient like the invariant regions, minimum length constraint or simply temporal constraints. The first processing improvement compared to what's been done in the full inversion, time-constrained processing is applying the temporal constraint only on the timelapse frames and not on the background. To do that, modifications to the pyGimli source code must be performed. This will probably decrease the error in the background result. Region regularizations can also be further investigated, similar to

what's been done with the synthetic model but improved. Hydrogeological modelling with Hydrus, for example, could also be realised to confirm ERT results.

With all these improvements in experimental conditions and processing, it is expected that inversion results will improve in terms of errors and resolution. Also, if the removal of all factors that influence the accuracy of the resistivity mapping is successful and the correct petrophysical analyses are performed, it is encouraging that it will be possible to accurately map water content or at least provide a close estimation.

References

- Anderson, S.H., Udawatta, R.P., Seobi, T. & Garrett, H.E., 2009. Soil water content and infiltration in agroforestry buffer strips. Agroforest Syst., 75, 5–16. https://doi.org/10.1007/s10457-008-9128-3
- Archie, G.E., 1942. The Electrical Resistivity Log as an Aid in Determining Some Reservoir Characteristics. Transactions of the AIME, 146, 54–62. https://doi.org/10.2118/942054-G
- Austin, M.C., Ginger, B.P., Bradley, J.C. & Mine D., 2017. Forward modelling to investigate inversion artifacts resulting from time-lapse electrical resistivity tomography during rainfall simulations. Journal of Applied Geophysics, 145, 39–49. https://doi.org/10.1016/j.jappgeo.2017.08.002
- Bah, B., Engels, P. & Colinet, G., 2005. Légende de la Carte Numérique des Sols de Wallonie (Belgique). Service Public de Wallonie.
- Binley, A., Hubbard, S.S., Huisman, J.A., Revil, A., Robinson, D.A., Singha, K. & Slater, L.D., 2015. The emergence of hydrogeophysics for improved understanding of subsurface processes over multiple scales. Water Resour. Res., 51, 3837–3866. https://doi.org/10.1002/2015WR017016
- Binley, A. & Kemna, A., 2005. DC Resistivity and Induced Polarization Methods. In: Rubin, Y., Hubbard, S.S. (eds), Hydrogeophysics. Water Science and Technology Library, vol 50. Springer, Dordrecht. https://doi.org/10.1007/1-4020-3102-5_5
- Blazevic, L.A., Bodet, L., Pasquet, S., Linde, N., Jougnot, D., & Longuevergne, L., 2020. Time-Lapse Seismic and Electrical Monitoring of the Vadose Zone during a Controlled Infiltration Experiment at the Ploemeur Hydrological Observatory. France. Water, 12(5), 1230. https://doi.org/10.3390/w12051230
- Brunet, P., Clément, R. & Bouvier, C., 2010. Monitoring soil water content and deficit using Electrical Resistivity Tomography (ERT) – A case study in the Cevennes area, France. Journal of Hydrology, 380(1–2), 146–153. https://doi.org/10.1016/j.jhydrol.2009.10.032
- Clément, R., Descloitres, M., Günther, T., Ribolzi, O. & Legchenko, A., 2009. Influence of shallow infiltration on time-lapse ERT: Experience of advanced interpretation. Comptes Rendus Géoscience, 341 (10-11), 886–898. https://doi.org/10.1016/j.crte.2009.07.005.
- Clément, R., Descloitres, M., Günther, T., Oxarango, L., Morra, C., Laurent, J -P., & Gourc, J -P., 2010. Improvement of electrical resistivity tomography for leachate injection monitoring. Waste Management, 30(3). https://doi.org/10.1016/j.wasman.2009.10.002
- Dahlin, T. & Zhou, B., 2004. A numerical comparison of 2D resistivity imaging with 10 electrode arrays. Geophysical Prospecting, 52, 379–398. https://doi.org/10.1111/j.1365-2478.2004.00423.x

- Dietrich, S., Weinzettel, P.A. & Varni, M., 2014. Infiltration and Drainage Analysis in a Heterogeneous Soil by Electrical Resistivity Tomography. Soil Science Society of America Journal, 78, 1153–1167. https://doi.org/10.2136/sssaj2014.02.0062
- Du, L., Qin, T., Mizunaga, H., Zong, Z., Zhu, W. & Zhu, Z., 2024. Monitoring water infiltration in multiple layers of sandstone coal mining model with cracks using ERT. Open Geosciences, 16(1). https://doi.org/10.1515/geo-2022-0707
- Ducut, J.D., Alipio, M., Go, P.J., Concepcion, R.II, Vicerra, R.R., Bandala, A., Dadios, E., 2022. A Review of Electrical Resistivity Tomography Applications in Underground Imaging and Object Detection. Displays, 73. https://doi.org/10.1016/j.displa.2022.102208.
- Dumont G., Pilawski, T., Hermans., T., Nguyen, F. & Garré, S., 2018. The effect of initial water distribution and spatial resolution on the interpretation of ERT monitoring of water infiltration in a landfill cover. Hydrology and Earth System Sciences: Discussions, EGU. https://doi.org/10.5194/hess-2018-163
- Everett, M.E., 2013. Electrical resistivity method. In: Near-Surface Applied Geophysics. Cambridge University Press. https://doi.org/10.1017/CBO9781139088435.005
- Fan, B., Liu, X., Zhu, Q., Qin, G., Li, J., Lin, H., & Guo, L., 2020. Exploring the interplay between infiltration dynamics and Critical Zone structures with multiscale geophysical imaging: A review. Geoderma, 374. https://doi.org/10.1016/j.geoderma.2020.114431
- Fernández de Vera, N., Beaujean, J., Jamin, P., Hakoun, V., Caterina, D., Dahan, O., Vanclooster, M., Dassargues, A., Nguyen, F. & Brouyère, S., 2017. Tracer Experiment in a Brownfield Using Geophysics and a Vadose Zone Monitoring System. Vadose Zone Journal, 16. https://doi.org/10.2136/vzj2016.06.0051
- Firoozi, A.A. & Firoozi, A.A., 2024. Water erosion processes: Mechanisms, impact, and management strategies. Results in Engineering, 24. https://doi.org/10.1016/j.rineng.2024.103237.
- Frohlich, R.K. & Parke, C.D., 1989. The electrical resistivity of the vadose zone field survey. Ground Water, 27(4), 524–530. https://doi.org/10.1111/j.1745-6584.1989.tb01973.x (not consulted)
- Haaken, K., Furman, A., Weisbrod, N. & Kemna, A., 2016. Time-Lapse Electrical Imaging of Water Infiltration in the Context of Soil Aquifer Treatment. Vadose Zone Journal, 15. https://doi.org/10.2136/vzj2016.04.0028
- Hayley, K., Pidlisecky, A. & Bentley, LR., 2011. Simultaneous time-lapse electrical resistivity inversion. Journal of Applied Geophysics, 75(2), 401–411. https://doi.org/10.1016/j.jappgeo.2011.06.035.
- Hermans, T., Vandenbohede, A., Lebbe, L., Martin, R., Kemna, A., Beaujean, J. & Nguyen, F., 2012a. Imaging artificial salt water infiltration using electrical resistivity tomography constrained by geostatistical data. Journal of Hydrology, 438-439, 168–180. https://doi.org/10.1016/j.jhydrol.2012.03.021

- Hermans, T., Vandenbohede, A., Lebbe, L. & Nguyen, F., 2012b. A shallow geothermal experiment in a sandy aquifer monitored using electric resistivity tomography. Geophysics, 77. https://doi.org/10.1190/geo2011-0199.1
- Hübner, R., Günther, T., Heller, K., Noell, U., & Kleber, A., 2017. Impacts of a capillary barrier on infiltration and subsurface stormflow in layered slope deposits monitored with 3-D ERT and hydrometric measurements. Hydrol. Earth Syst. Sci., 21, 5181–5199. https://doi.org/10.5194/hess-21-5181-2017.
- Kam, J., Traynor, D., Clifton-Brown, J.C., Purdy, S.J. & McCalmont, J.P., 2020. Miscanthus as Energy Crop and Means of Mitigating Flood. In: Naddeo, V., Balakrishnan, M., Choo, K.H. (eds) Frontiers in Water-Energy-Nexus–Nature-Based Solutions, Advanced Technologies and Best Practices for Environmental Sustainability. Advances in Science, Technology & Innovation. Springer, Cham. https://doi.org/10.1007/978-3-030-13068-8_115
- Karaoulis, M.C., Kim, J.H. & Tsourlos, P.I., 2011. 4D active time constrained resistivity inversion. Journal of Applied Geophysics, 73, 25–34. https://doi.org/10.1016/j.jappgeo.2010.11.002.
- Lesparre, N., Nguyen, F., Kemna, A., Robert, T., Hermans, T., Daoudi, M. & Flores-Orozco, A., 2017. A new approach for time-lapse data weighting in electrical resistivity tomography. Geophysics, 82(6), 325–333. https://doi.org/10.1190/geo2017-0024.1
- Loke, M.H., Chambers, J.E., Rucker D.F., Kuras, O., & Wilkinson, P.B., 2013. Recent developments in the direct-current geoelectrical imaging method. Journal of Applied Geophysics, 95, 135–156. https://doi.org/10.1016/j.jappgeo.2013.02.017.
- Loukil, E., Gargouri, K., Ben Mbarek, H., Soua, N., Ouhibi, T., Gargouri, N.K., & Rigane, H., 2021. Application of electrical resistivity tomography method for the assessment of olive mill wastewater infiltration in storage basin site (southeastern Tunisia). Arabian Journal of Geosciences, 14. https://doi.org/10.1007/s12517-021-07565-7.
- Lu, D., Wang, H., Geng, H., Xia, Y., Wu, C. & Hua, E., 2022. Imaging and characterization of the preferential flow process in agricultural land by using electrical resistivity tomography and dual-porosity model. Ecological Indicators, 134. https://doi.org/10.1016/j.ecolind.2021.108498.
- Mazur, A. & Kowalczyk-Juśko, A., 2021. The Assessment of the Usefulness of Miscanthus x giganteus to Water and Soil Protection against Erosive Degradation. Resources, 10(7), 66. https://doi.org/10.3390/resources10070066
- Nguyen, F., De Lanève, C., Boutarfa, A., Swerts, G., Degrée, A. & Caterina, D., 2025. Electrical Resistivity Tomography Monitoring of an Infiltration Test in an Agricultural Context within a Miscanthus Parcel. EGU General Assembly 2025, Vienna, Austria, 27 Apr–2 May 2025, EGU25-18089. https://doi.org/10.5194/egusphere-egu25-18089.

- Philips, C.E. & Kitch, W.A., 2011. A Review of Methods for Characterization of Site Infiltration with Design Recommendations. Journal of the Nevada Water Resources Association, 6, 29–46.
- Robert, T. & Bolly, P.Y., 2015. Rapport final sur les essais de captage menés au Sart-Tilman. Technical report. AQUALE.
- Rücker, C., Günther, T. & Wagner, F.M., 2017. pyGIMLi: An open-source library for modelling and inversion in geophysics. Computers and Geosciences, 109, 106–123. https://doi.org/10.1016/j.cageo.2017.07.011
- Service public de Wallonie (SPW), 2022. Carte Numérique des Sols de Wallonie. http://geodata.wallonie.be/id/38c2a87e-d38a-4359-9899-9d4a6b9f0c2a
- Service public de Wallonie (SPW), 2024. Orthophotos 2023 Été (2024-01-26). http://geodata.wallonie.be/id/ad55c2ce-62ad-4c3c-b3cf-8fbc270a6b6e
- Telford, W.M., Geldart, L.P. & Sheriff, R.E., 1990. Appl. Geophys., 2nd ed. Cambridge Univ. Press, New York Port Chester, p. 770. (not consulted)
- Ward, S.H., 1990. Resistivity and induced polarization methods. In: Ward, S.H. (ed.), Geotechnical and Environmental Geophysics 1, Investigations in Geophysics, vol. 5. Society of Exploration Geophysics, 147–189. https://doi.org/10.1190/1.9781560802785.ch6 (not consulted)
- Watlet, A., Kaufmann, O., Triantafyllou, A., Poulain, A., Chambers, J. E., Meldrum, P. I., Wilkinson, P. B., Hallet, V., Quinif, Y., Van Ruymbeke, M., & Van Camp, M., 2018. Imaging groundwater infiltration dynamics in the karst vadose zone with long-term ERT monitoring. Hydrol. Earth Syst. Sci., 22, 1563–1592. https://doi.org/10.5194/hess-22-1563-2018.
- Waxman, M.H. & Smits, L.J.M., 1968. Electrical Conductivities in Oil-Bearing Shaly Sands. SPE J. 8, 107–122. https://doi.org/10.2118/1863-A
- Winkler, B., Mangold, A., von Cossel, M., Clifton-Brown, J., Pogrzeba, M., Lewandowski, I., Iqbal, Y. & Kiesel, A., 2020. Implementing miscanthus into farming systems: A review of agronomic practices, capital and labour demand. Renewable and Sustainable Energy Reviews, 132. https://doi.org/10.1016/j.rser.2020.110053.
- Zhao, K., Xu, Q, Liu, F., Xiu, D. & Ren, X., 2020. Field monitoring of preferential infiltration in loess using time-lapse electrical resistivity tomography. Journal of Hydrology, 591. https://doi.org/10.1016/j.jhydrol.2020.125278.

Annexes

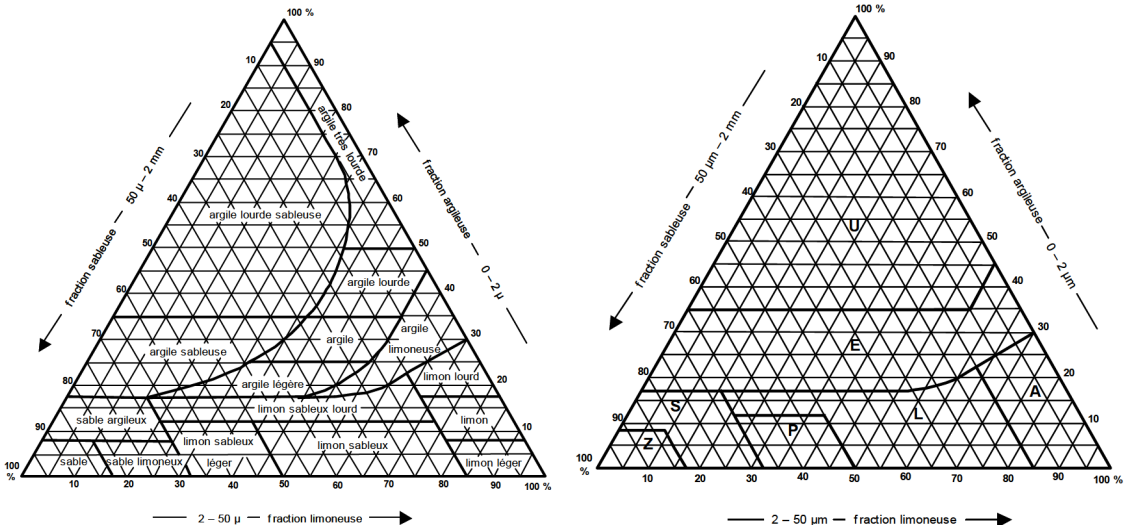

Annexe 1: Diagrams of soil texture from the digital soil map of Wallonia (soil from experiment is classification A) (Bah et al., 2005)

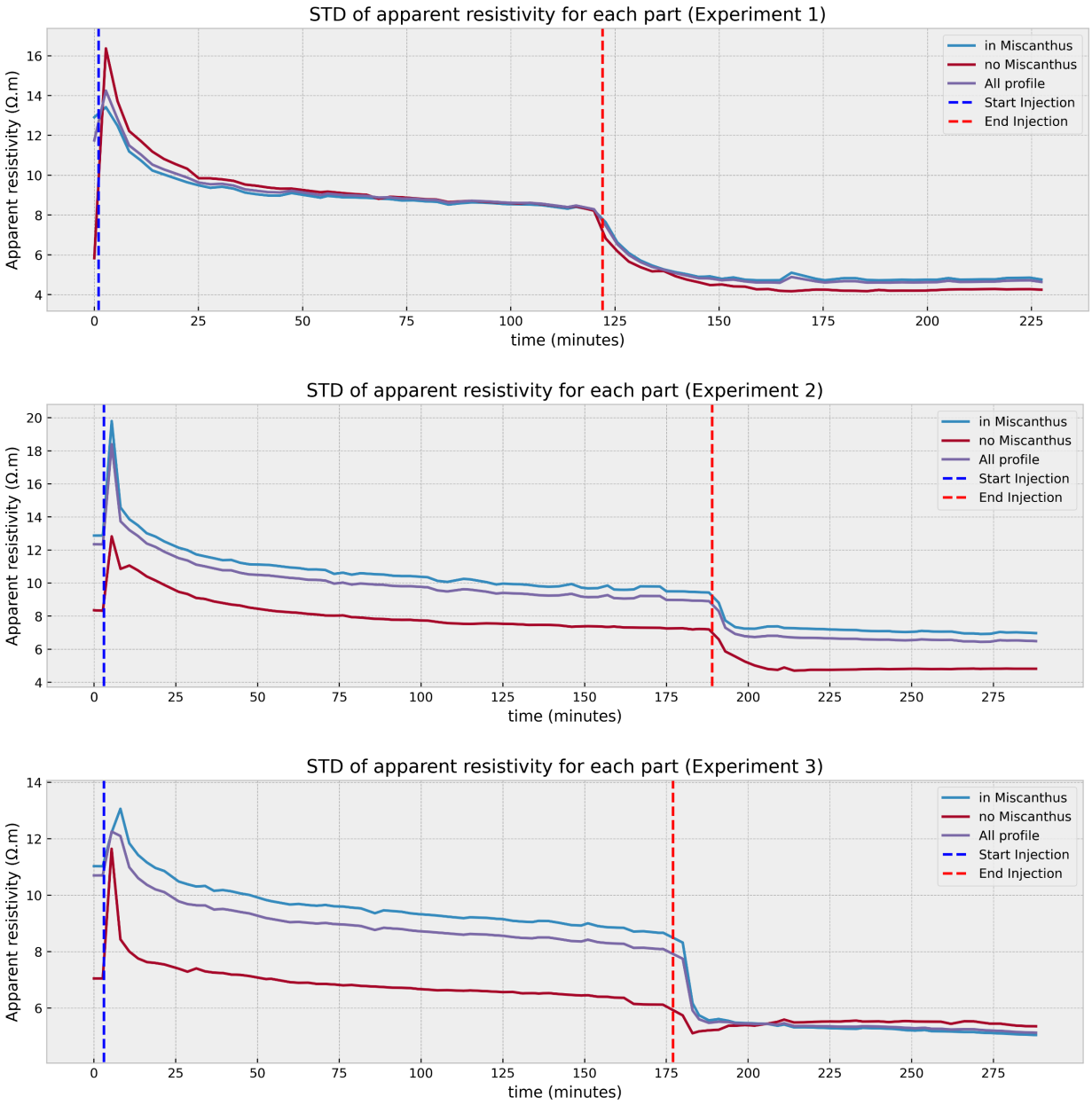

Annexe 2: Standard deviation of apparent resistivities evolution with time on the overall profile and for pseudo-points in or out of the Miscanthus for each experiment

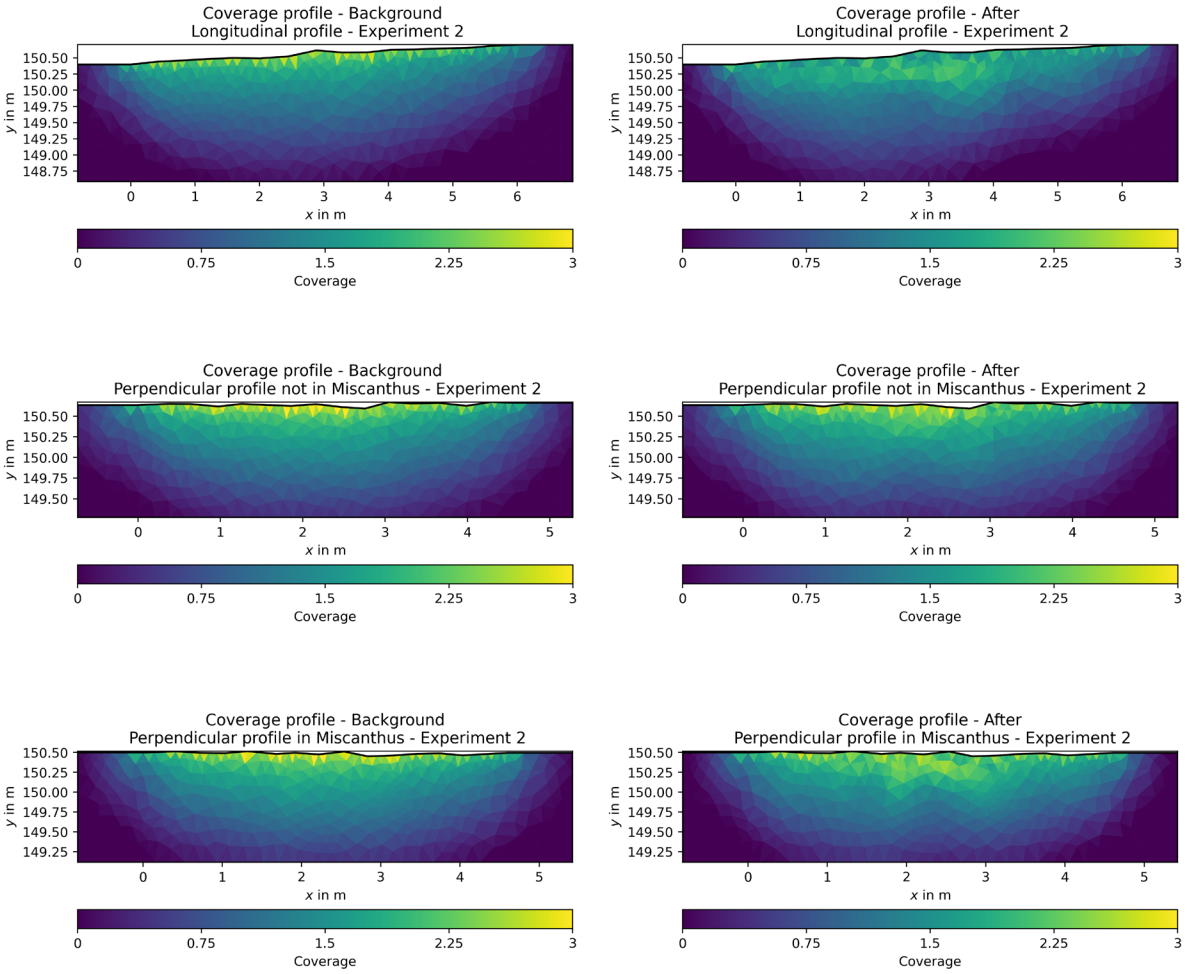

Annexe 3: Coverage profiles of background (Left) and after-infiltration (Right) of each profile for experiment 2

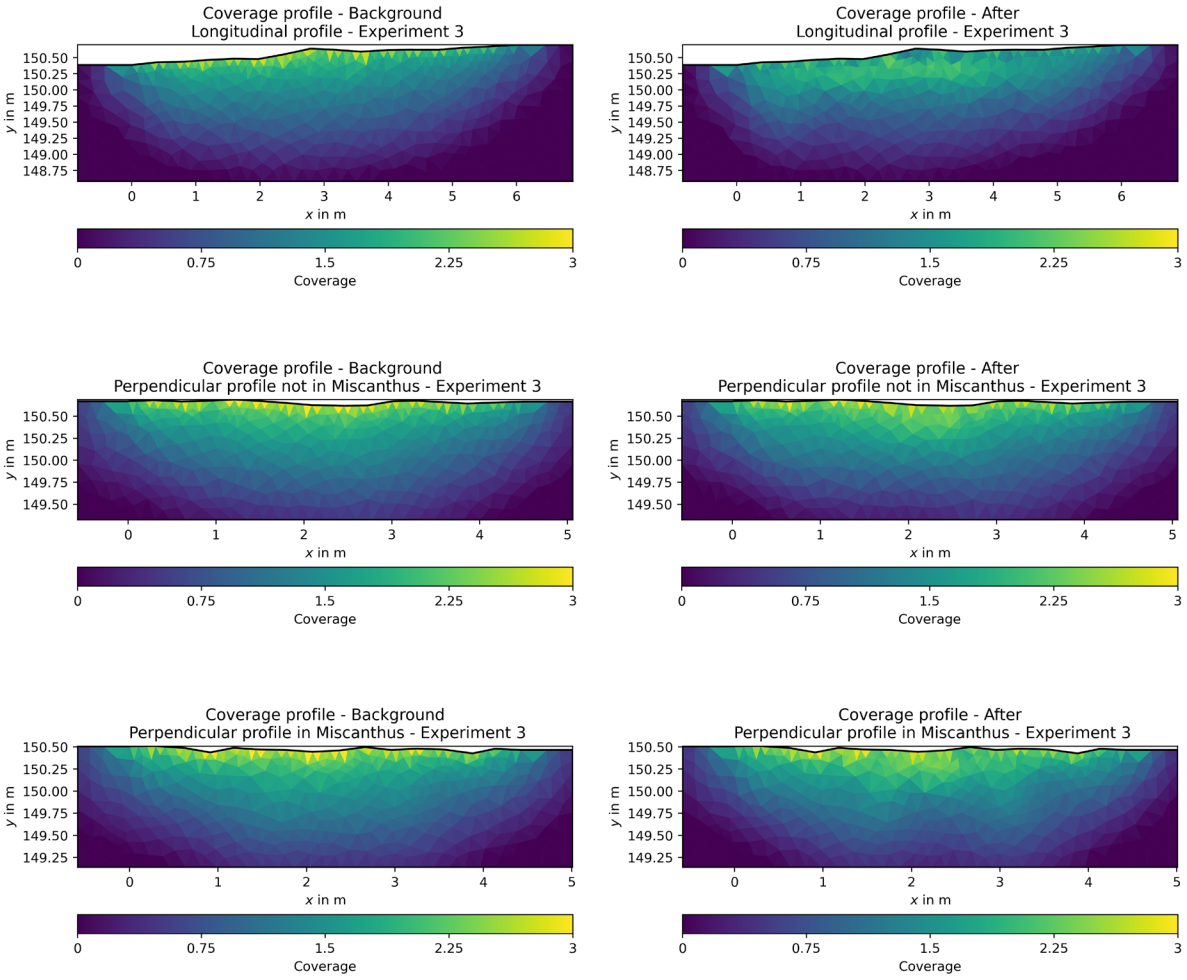

Annexe 4: Coverage profiles of background (Left) and after-infiltration (Right) of each profile for experiment 3

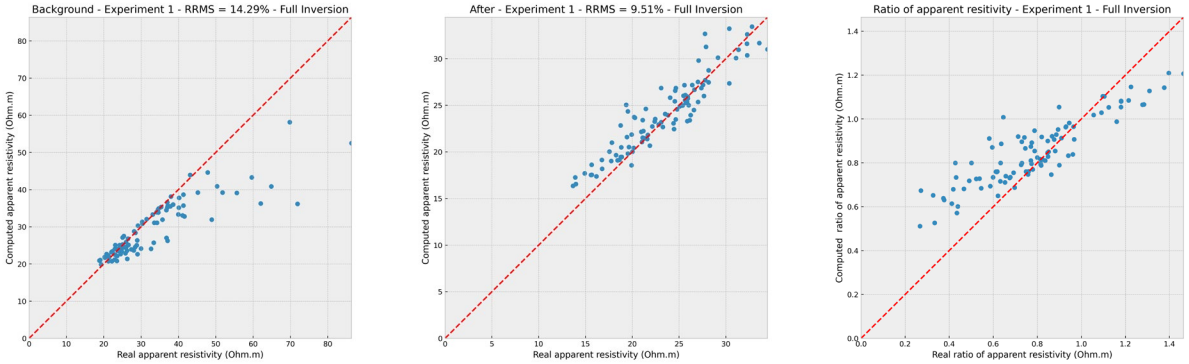

Annexe 5: Comparison of the real and simulated data for time-vonstrained processing for the longitudinal profile of the experiment 1

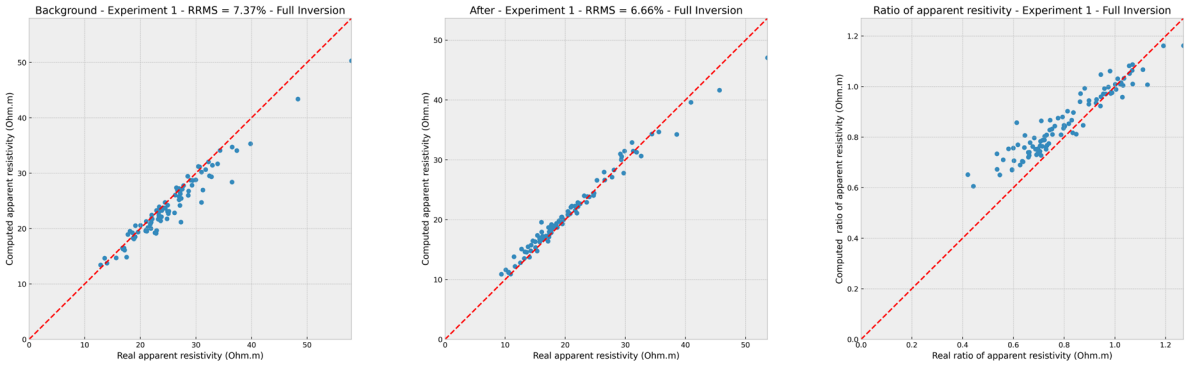

Annexe 6: Comparison of the real and simulated data for time-constrained processing for the perpendicular profile not in miscanthus of the experiment 1

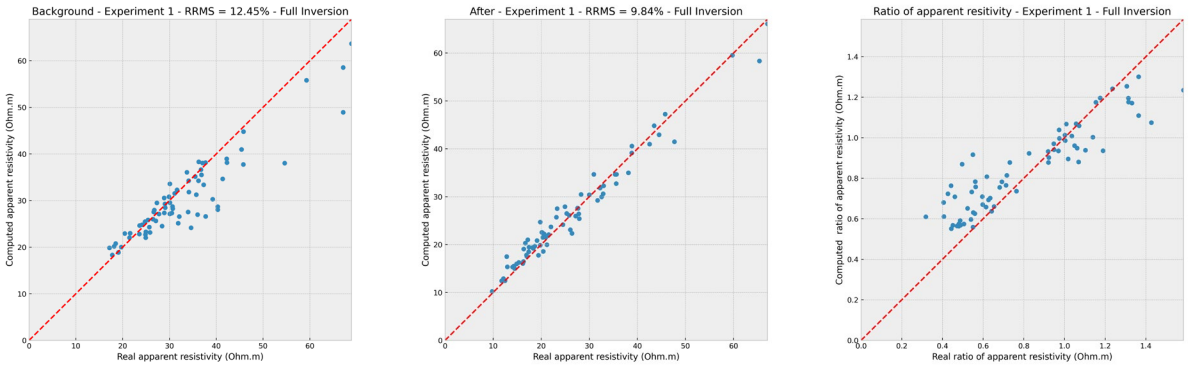

Annexe 7: Comparison of the real and simulated data for time-constrained processing for the perpendicular profile in miscanthus of the experiment 1

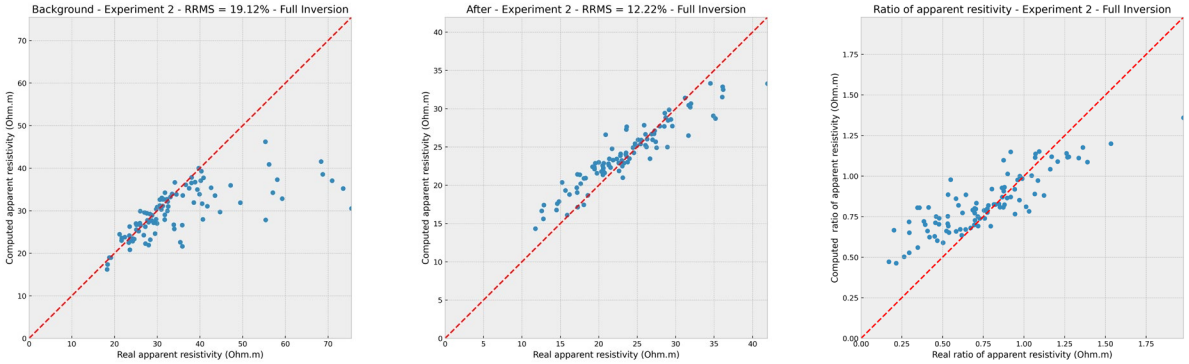

Annexe 8: Comparison of the real and simulated data for time-constrained processing for the longitudinal profile of the experiment 2

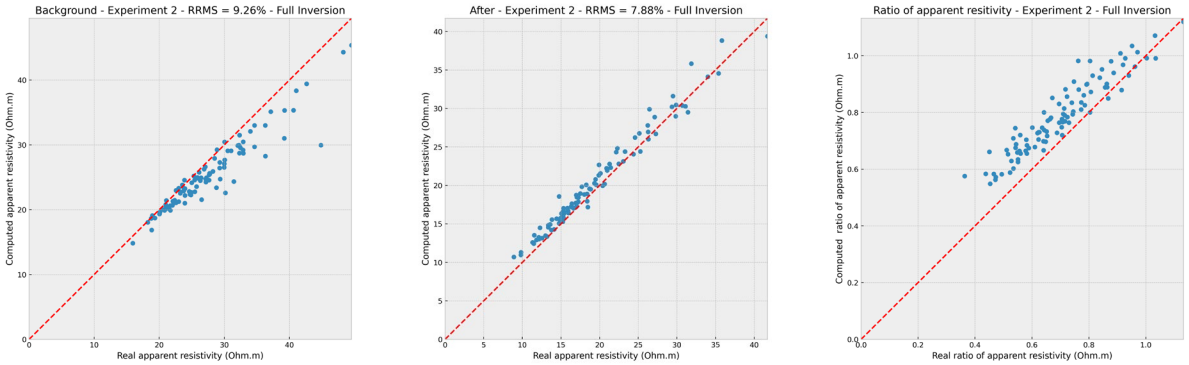

Annexe 9: Comparison of the real and simulated data for time-constrained processing for the perpendicular profile not in miscanthus of the experiment 2

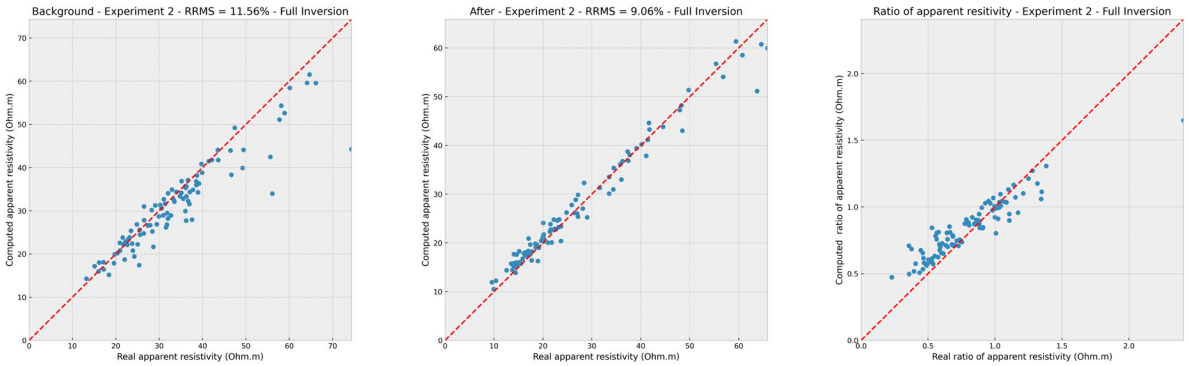

Annexe 10: Comparison of the real and simulated data for time-constrained processing for the perpendicular profile in miscanthus of the experiment 2

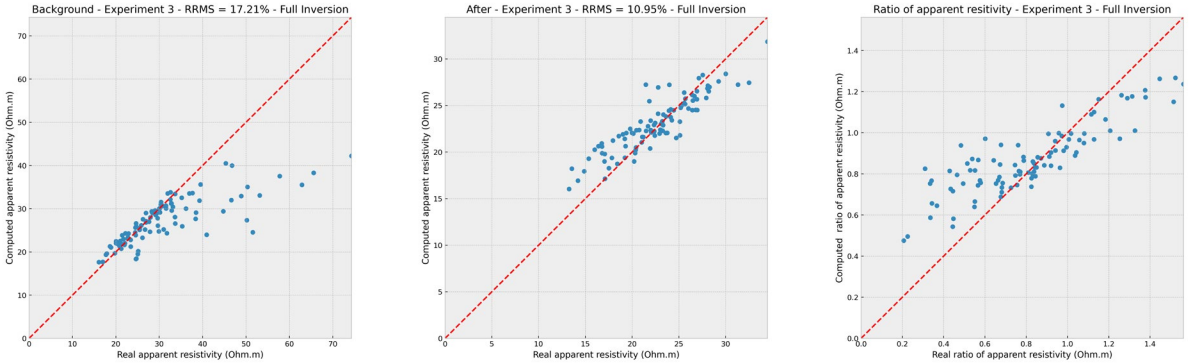

Annexe 11: Comparison of the real and simulated data for time-constrained processing for the longitudinal profile of the experiment 3

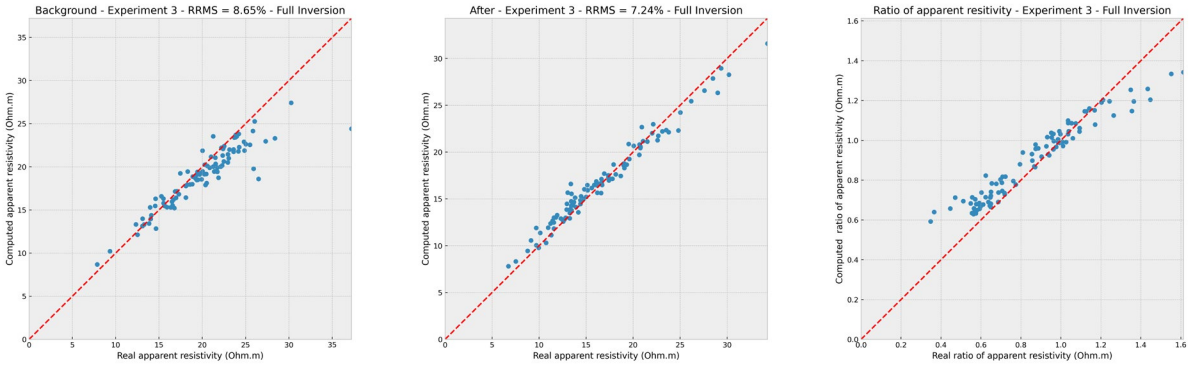

Annexe 12: Comparison of the real and simulated data for time-constrained processing for the perpendicular profile not in miscanthus of the experiment 3

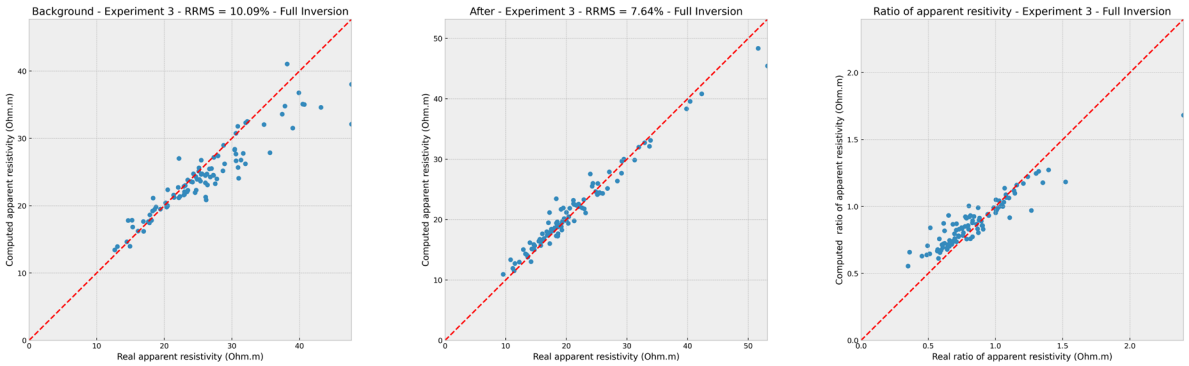

Annexe 13: Comparison of the real and simulated data for time-constrained processing for the perpendicular profile in miscanthus of the experiment 2

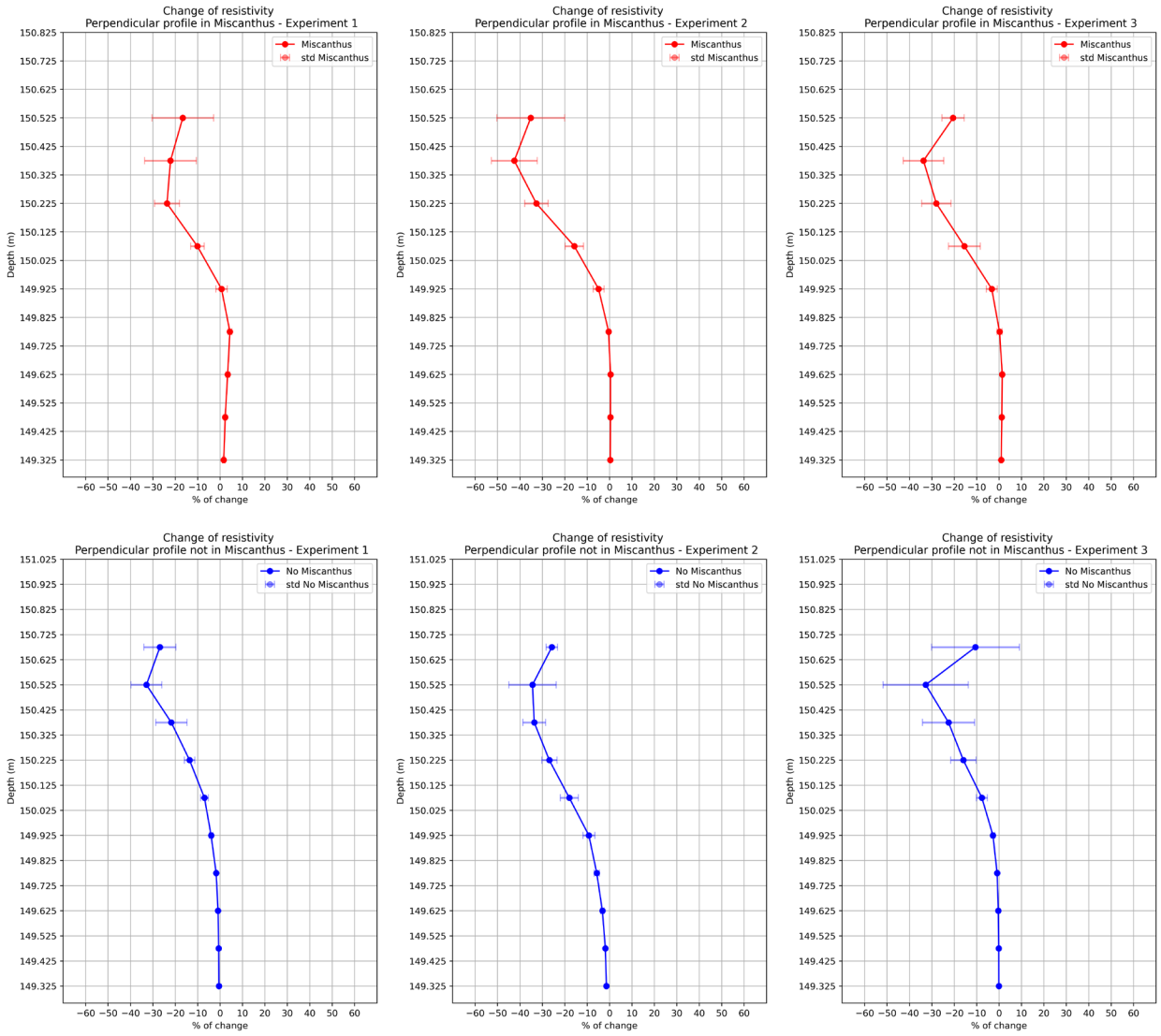

Annexe 14: Vertical variation of resistivity in and out of the miscanthus for the perpendicular profiles in (Top) or out (Bottom) of the miscanthus of each experiment

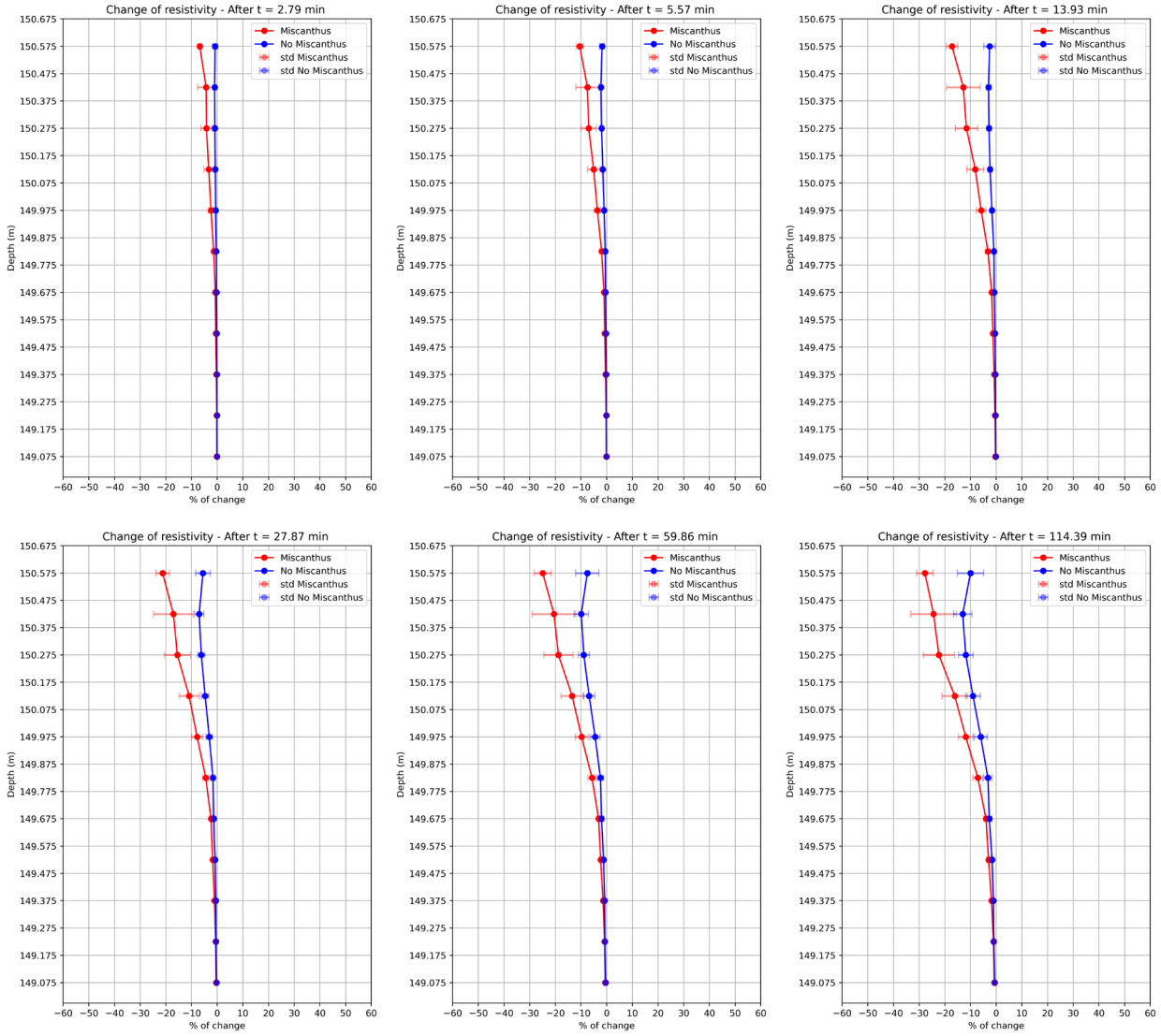

Annexe 15: Timelapse vertical change of resistivity in or out of the miscanthus for the longitudinal profile of the experiment 1

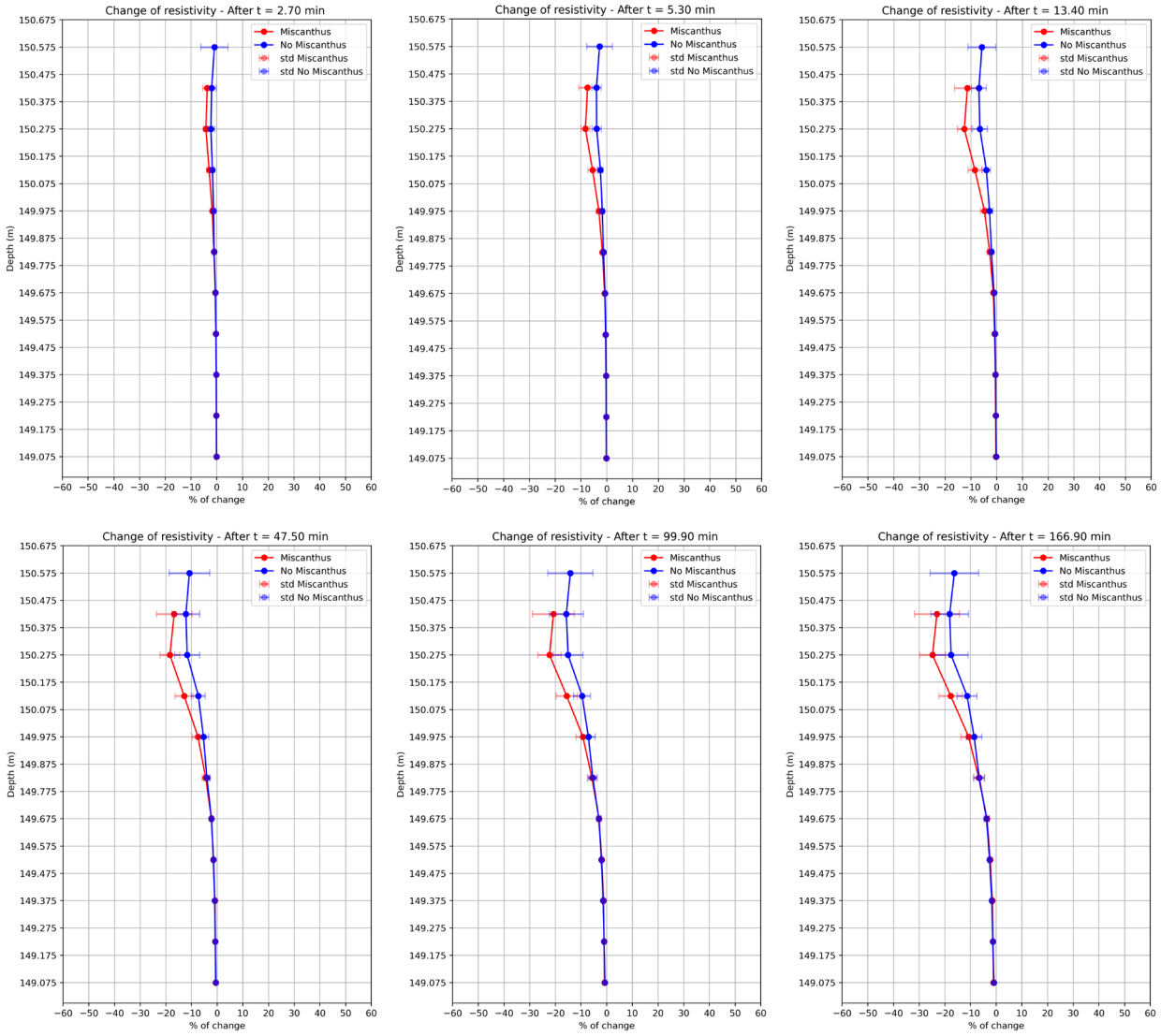

Annexe 16: Timelapse vertical change of resistivity in or out of the miscanthus for the longitudinal profile of the experiment 2

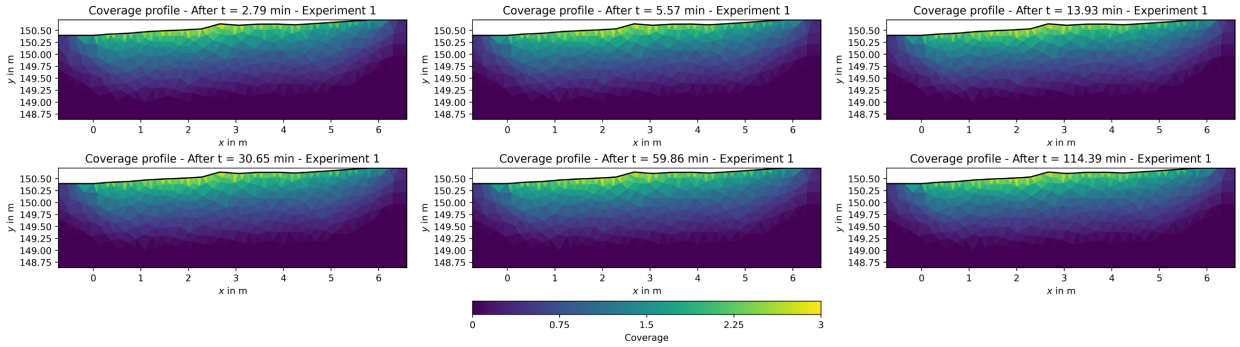

Annexe 17: Coverage profiles of timelapse frames of the longitudinal profile for the experiment 1

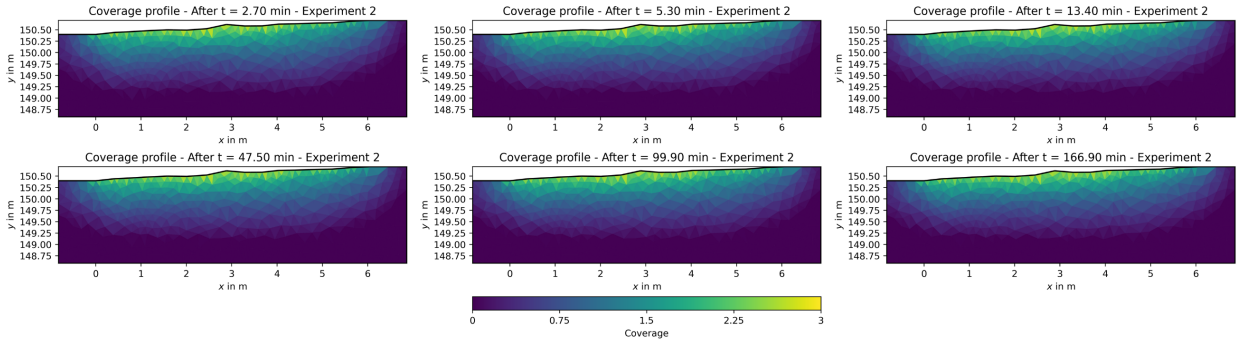

Annexe 18: Coverage profiles of timelapse frames of the longitudinal profile for the experiment 2

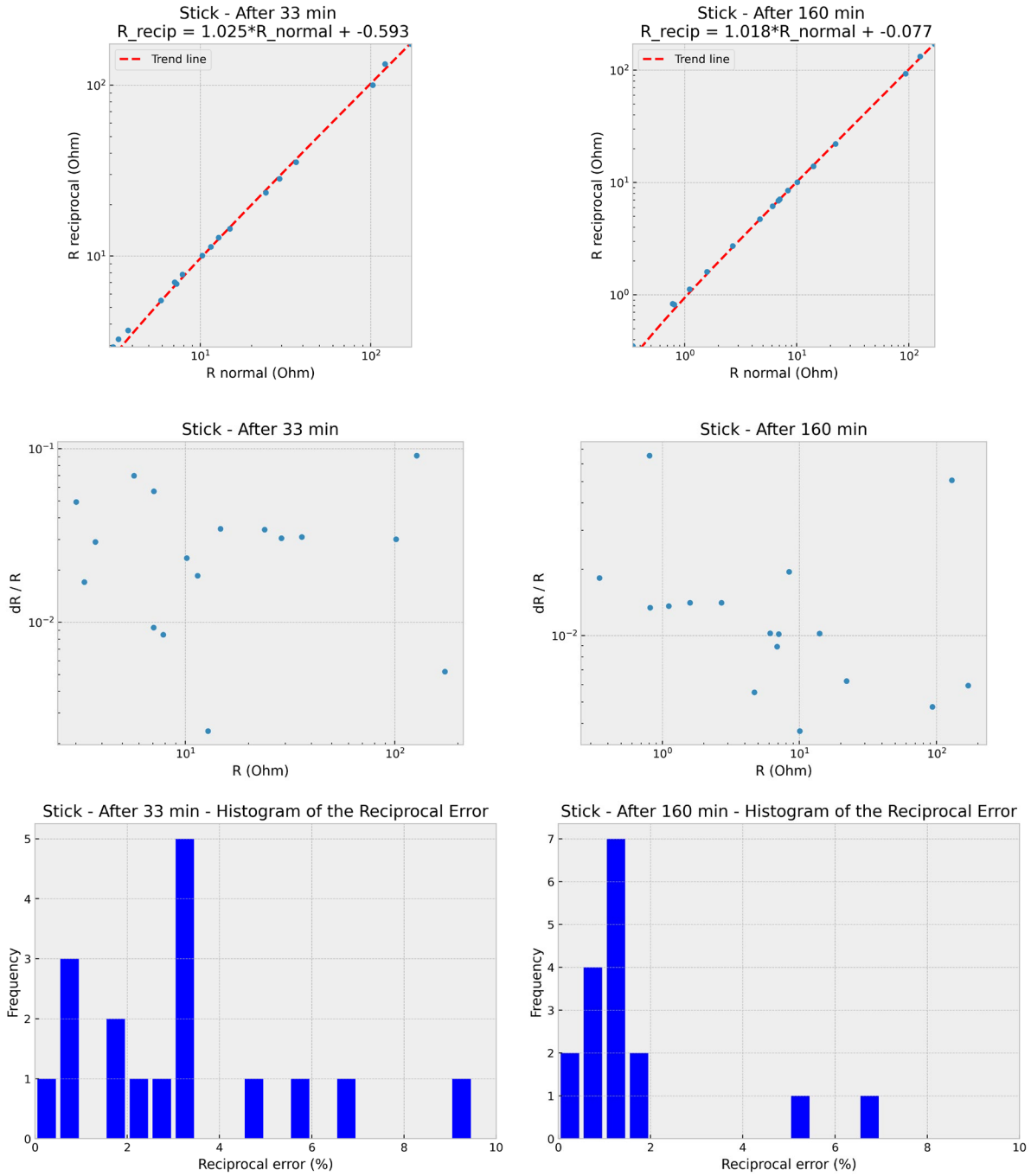

Annexe 19: Reciprocal study from the two reciprocal measurements during the timelapse for the infiltration stick